

# Knowledge-based acceleration of MRI for metal object localization

Frank Zijlstra

**ISBN:** 978-90-393-6891-6

**Cover design:** Frank Zijlstra

**Layout:** Frank Zijlstra

**Printed by:** Ridderprint B.V.

Copyright © F. Zijlstra, 2017

All rights reserved. No part of this publication may be reproduced or transmitted in any form or by any means without prior permission from the copyright owner. The copyright of the articles that have been published has been transferred to the respective journals.

# Knowledge-based acceleration of MRI for metal object localization

Op kennis gebaseerde versnelling van MRI  
voor lokalisatie van metalen objecten  
(met een samenvatting in het Nederlands)

## **Proefschrift**

ter verkrijging van de graad van doctor aan de Universiteit Utrecht  
op gezag van de rector magnificus, prof. dr. G.J. van der Zwaan  
ingevolge het besluit van het college voor promoties  
in het openbaar te verdedigen op  
dinsdag 14 november 2017 des ochtends te 10.30 uur

door

Frank Zijlstra  
geboren op 31 augustus 1985  
te Smalingerland

Promotoren: Prof. dr. ir. M.A. Viergever  
Prof. dr. P.R. Luijten

Copromotor: Dr. ir. P.R. Seevinck

This thesis is part of the research programme Applied and Engineering Sciences (TTW) with project number 10712 which is (partly) financed by the Netherlands Organization for Scientific Research (NWO).

The publication of this thesis was financially supported by Elekta and Philips Healthcare.

# CONTENTS

<b>1</b>	<b>Introduction</b>	<b>3</b>
<b>2</b>	<b>Evaluation of variable density and data-driven k-space undersampling for Compressed Sensing MRI</b>	<b>13</b>
<b>3</b>	<b>Fast Fourier-based simulation of off-resonance artifacts in steady-state gradient echo MRI applied to metal object localization</b>	<b>35</b>
<b>4</b>	<b>Challenges in MR-only seed localization for postimplant dosimetry in permanent prostate brachytherapy</b>	<b>51</b>
<b>5</b>	<b>Simultaneous real-time anatomical imaging and passive device tracking using multi-echo undersampled radial acquisitions for MR-guided interventions</b>	<b>69</b>
<b>6</b>	<b>Summary and discussion</b>	<b>91</b>
	<b>Bibliography</b>	<b>97</b>
	<b>List of publications</b>	<b>105</b>
	<b>Nederlandse samenvatting (Dutch summary)</b>	<b>109</b>
	<b>About the author</b>	<b>113</b>



CHAPTER



# INTRODUCTION

## 1.1 General introduction

In this thesis we present four studies relating to accelerating MRI and localizing metal devices in MRI to aid MR-guided interventions and other applications where the presence of metal is otherwise problematic. In each of these studies we incorporated prior knowledge in the MRI acquisition, reconstruction, and image analysis pipeline to approach these problems, following the same basic principle: the more is known about a problem beforehand, the easier and faster it will be to solve the problem. In this thesis we will show the value of this approach in MRI and how it can help accelerate MRI and localize metal devices in MRI.

In this introduction we will first discuss the importance of scan time in MRI and what factors influence scan time. Second, we will describe approaches that have been taken to accelerate MRI, including the use of prior knowledge. Finally, we discuss the problems associated with the presence of metal in MRI and outline applications where specifically the location of a metal device is important. We end this introduction with an outline of the rest of the thesis.

## 1.2 MRI

In the last two decades MRI has gained an important position in radiology mainly due to its unsurpassed performance in anatomical, functional, and physiological imaging of soft tissues in the human body. MRI has the unique ability to create images with different types of contrasts between different tissues or between healthy and diseased tissue. For example, these contrasts can be based on magnetic relaxation properties of the tissue, on whether the tissue contains fat, and also on physiological properties such as blood flow or diffusivity. Together these images with different contrasts can help paint a complete picture of a disease to aid diagnosis, treatment planning, treatment monitoring, and even MR-guided interventions. An additional benefit of MRI is that it does not use harmful radiation, in contrast to x-ray and CT.

The favorable diagnostic properties of MRI have caused a steady rise in the number of MRI exams performed each year (Fig. 1.1). Associated with this growth, there is an increasing need for efficiency to keep up with the rising demand and to help reduce the cost of MRI exams. In 2016, the International Society for Magnetic Resonance in Medicine recognized this need by launching the MR Value Initiative: an effort to promote research that improves the cost-effectiveness of MRI exams. This can be research that aims at faster imaging, or research that attempts to increase the utility of MRI scans in order to answer specific diagnostic questions without requiring a full MRI exam.

## 1.3 MRI scan time

Scan time is an important aspect of MRI in clinical practice. First of all, the length of a full MRI exam is directly dependent on the scan times of individual MRI scans. If images of the same quality could be acquired in less time, the full exam will be shorter and a patient will have to spend less time in the scanner. An important aspect of MRI is that scan time can be traded against image quality. For example, a higher resolution image will take more time to acquire. Therefore, faster imaging could be used to improve resolution, instead of reducing

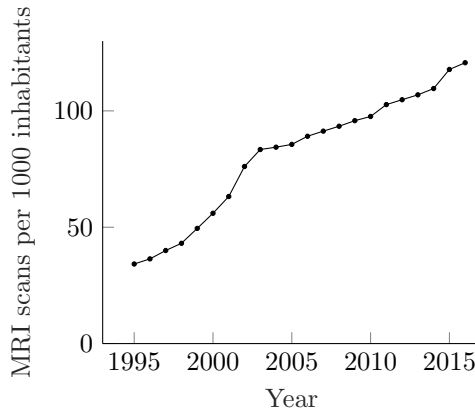


**FIGURE 1.1:** Growth of MRI usage in the United States from 1995 to 2016. Source: OECD [1]

scan time. Similar tradeoffs exist with other imaging aspects, such as the size of the field of view and the signal-to-noise ratio of the image.

Total scan time in MRI is defined by the time it takes to acquire enough data to be able to accurately reconstruct an image of the subject in the scanner. In MRI, data is acquired in the frequency domain, referred to as k-space. By manipulating radiofrequency pulses and magnetic field gradients, the MR signal can be encoded at different locations in k-space. A sequence of such pulses and encoding gradients is called a pulse sequence. Because enabling encoding gradients in MRI represent movement through k-space, we say that k-space is traversed using the pulse sequence.

The pulse sequence is designed in such a way that data is acquired at all locations of a discrete k-space. The size of k-space and density at which k-space must be sampled is determined by the Nyquist criterion, given a desired resolution and field of view. When the entire k-space is acquired, an image can be reconstructed by applying a Fourier transform to the acquired data. If k-space was sampled according to the Nyquist criterion, the reconstructed image is guaranteed to be free of aliasing artifacts.

As a result of the Nyquist criterion, the time it takes to acquire an MR image is defined by the time it takes to play out the pulse sequence that acquires the entire k-space. The size of k-space is an important factor in this, scans with higher resolution and/or larger field of views will take longer to acquire. The speed of k-space traversal is also limited by scanner hardware, such as the maximum amplitude and maximum slew rate of the gradient system.

Another important factor is the time efficiency of the pulse sequence, i.e. the fraction of the pulse sequence that is spent acquiring k-space data. The creation of contrast in MR images often boils down to the timing of the pulse sequence, which may influence the efficiency of the acquisition. For example, in order to create  $T_2$ -weighted contrast, sufficient time must pass between the excitation and acquisition of the signal to allow  $T_2$ -relaxation to take place.

Finally, there are physical limits to ensure patient safety during scanning. Fast switching of gradients should be limited to avoid peripheral nerve stimulation. And RF power must be limited to avoid excess heating of tissue.

## 1.4 Accelerating MRI

In comparison with other imaging modalities, the scan time of MRI is relatively long. Because of this, acceleration of MRI has been an active field of research since the inception of MRI. The approaches for accelerating MRI can be loosely classified in two categories. First, there are approaches that aim to increase the scan efficiency, i.e. to acquire more data in the same time, or the same amount of data in less time. Second, there are approaches that aim to acquire less data while still being able to reconstruct high quality images.

In general, scan efficiency has improved because of improvements of the MRI hardware. For example, better gradient systems can create encoding gradients with higher amplitudes and higher slew rates, which allow faster traversal of k-space.

Additionally, pulse sequences with higher efficiency have been developed. For example, sequences that acquire multiple echoes in a single pulse sequence repetition can acquire multiple image contrasts while the total scan time remains largely unchanged [2]. The Turbo Spin Echo sequence and Echo Planar Imaging apply the same concept, but also change the phase encoding of echo of the echoes to acquire more than one k-space line per repetition of the pulse sequence [3, 4]. More recently, Simultaneous Multi-Slice imaging has been proposed to acquire signal from multiple slices at once [5].

Methods that accelerate by acquiring less k-space data necessarily violate the Nyquist criterion. This is commonly referred to as undersampling or as an undersampled acquisition. The violation of the Nyquist criterion means that linear reconstructions of the acquired data will exhibit aliasing artifacts. The way these aliasing artifacts appear in the reconstructed image depends on which k-space data is acquired. The selection of k-space data is generally referred to as the (under)sampling pattern or the sampling trajectory.

The effect of aliasing artifacts can be expressed in terms of point spread function (PSF), which determines how a signal originating from a single voxel will be replicated across the image. For Cartesian undersampling, the PSF can be calculated as the inverse Fourier transform ( $\mathcal{F}^{-1}$ ) of the (under)sampling pattern expressed as a binary mask ( $S$ ):

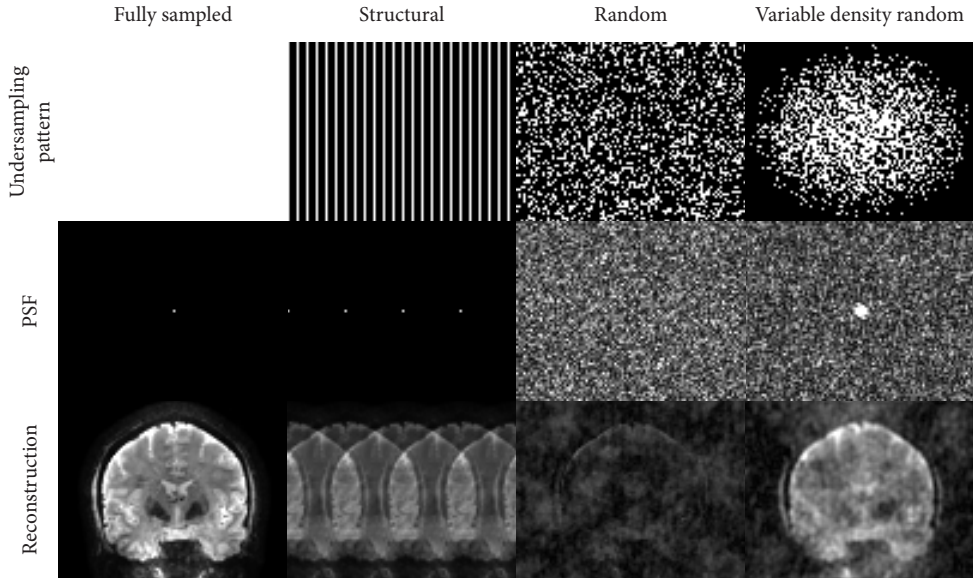
$$PSF = \mathcal{F}^{-1} S \quad (1.1)$$

Figure 1.2 shows examples of the PSFs associated with different undersampling patterns and their effects on an MR image.

Without any additional prior knowledge, aliasing artifacts resulting from undersampling cannot be removed. Methods that accelerate MRI through undersampling therefore need to make additional assumptions about the acquired data and/or the reconstructed image.

For example, partial Fourier imaging works under the assumption that the reconstructed image is real-valued. If this condition holds, k-space exhibits conjugate symmetry. This allows up to half of k-space to be reconstructed from the other half of k-space using the complex conjugate operation, which can accelerate acquisitions up to a factor of 2 [6].

Parallel imaging methods such as SENSE [7] or GRAPPA [8] use the redundancy of signal originating from multiple receive coils and the spatially varying sensitivity profile of these coils. If the coil sensitivity profiles are known, the undersampled signal from multiple coils can be reconstructed into a single image free of aliasing. In SENSE, the coil sensitivities are assumed to be known a priori, usually from a previously acquired coil sensitivity scan. In GRAPPA, coil sensitivities are acquired in the same scan, which requires additional k-space



**FIGURE 1.2:** The effect of different types of undersampling on the point spread function (PSF) and on the way the aliasing artifacts exhibit in the reconstructed image.

lines to be acquired for coil calibration. Although in theory the undersampling pattern can be freely chosen, structural undersampling patterns (i.e. skipping lines on regular intervals) are most commonly used because the associated PSFs have zeroes in all but a few locations, which allows parallel imaging reconstructions to be very computationally efficient. The acceleration achieved by parallel imaging in clinical practice typically ranges up to a factor of 4 [9].

Compressed Sensing (CS) reconstruction is a more recent development in undersampled MRI [10]. In CS the reconstructed image is assumed to be sparse in some transform domain, i.e. after transformation there will be very few high values and many values close to zero. Most medical images exhibit some sort of sparsity. This is shown by the success of applying image compression algorithms (e.g. JPEG) to such images, which are also based on exploiting image sparsity [11]. Common transformations in which medical images exhibit sparsity include the Wavelet transform and the finite difference transform [10], as shown in Figure 1.3.

In contrast to most other acceleration methods, CS uses undersampling schemes that produce incoherent aliasing artifacts. Incoherent aliasing spreads throughout the image as a noise-like interference. By imposing the reconstructed image to be sparse in a predefined domain, this noise-like interference can be removed using a non-linear reconstruction that simultaneously enforces sparsity and consistency with the acquired data. As a result, images free from aliasing can be reconstructed from incoherently undersampled data. Figure 1.4 shows an example of a CS reconstruction applied to an MR image of the brain that was undersampled with a factor 4 using a variable density random undersampling pattern (Fig. 1.2). Because acceleration achieved with CS is based on different principles, it can be com-

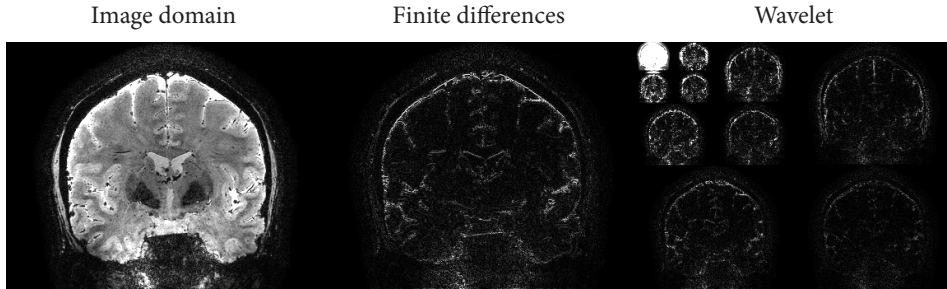


**FIGURE 1.3:** An MR image of the brain transformed using the vertical finite differences transform and the Wavelet transform. The transformed images can be seen to exhibit more sparsity than in the image domain (i.e. the transformations contain fewer voxels with high values).

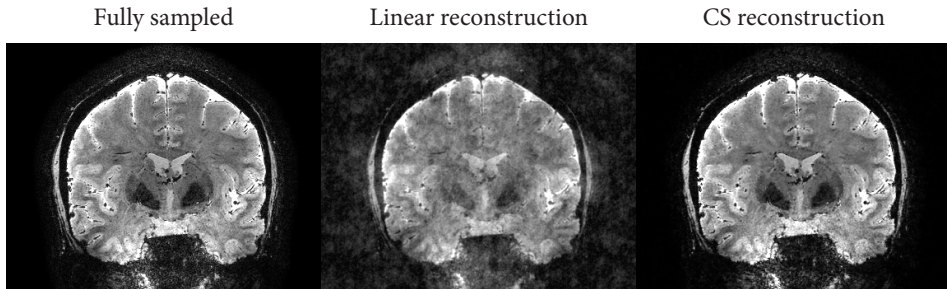


**FIGURE 1.4:** Compressed Sensing (CS) reconstruction of an MR image of the brain that was under-sampled with a factor 4 using a variable density random undersampling pattern. The fully sampled image and linear reconstruction of the undersampled data are shown for reference.

combined with other fast imaging and acceleration methods to achieve even higher acceleration factors. For example, CS and parallel imaging have been successfully combined [12] and can be used together to achieve acceleration factors up to 8 [13].

Many parameters need to be chosen to apply CS in practice. Most notably these parameters are the type and degree of sparsity that is enforced, the undersampling pattern, and the reconstruction algorithm. Although CS has been successfully applied to different types of MRI scans, not much is known about the influence of these parameters on the quality of the reconstructed image. As a consequence it is difficult to assess whether CS is being applied optimally. Because these parameters represent prior knowledge of the reconstructed image, optimizing these parameters using explicitly available prior knowledge could lead to higher quality CS reconstructions that are optimal for a specific application.

## 1.5 Prior knowledge in MRI

The successful application of CS shows the value of using prior knowledge to accelerate MRI acquisitions. The general idea here is straightforward: the more is known about the

image a priori, the less data needs to be acquired to be able to reconstruct the image.

Prior knowledge can be present at different levels of the imaging and image processing pipeline. From top to bottom these levels can be loosely defined as: the patient, the image, and the physics. On the patient level, prior knowledge can be available about for example: patient characteristics (age, sex, etc.), results from other diagnostic exams, and the presence of pathology or devices such as implants.

Prior knowledge about the image can include knowledge of the appearance and shape of specific anatomies; information from other MRI scans or scans from different imaging modalities, for example through image registration; and knowledge about image characteristics, such as the sparsity constraints used in Compressed Sensing.

On the physical level, prior knowledge can include from knowledge about physical processes in MRI, such as  $T_1$  and  $T_2$  relaxation and magnetic susceptibility effects, physiological phenomena such as the breathing pattern and heart rate, and exact knowledge of hardware involved, such as scanner hardware or models of devices present in MR-guided interventions.

Before CS was proposed, the use of prior knowledge in MR image reconstruction had been mostly on the physical level. In quantitative MR imaging, for example, model-based reconstructions use knowledge about physical processes to recover underlying MR parameters, such as  $T_1$  and  $T_2$  relaxation parameters [14] or susceptibility maps [15].

The successful application of CS to MRI has since inspired more research that attempts to use prior knowledge on the image level. In particular in dynamic imaging results have been promising, where redundancy in the time domain can also be exploited [16]. Other interesting approaches include the use of scans of the same anatomy from the same session as prior knowledge [17], and the combination of CS with model-based reconstructions [18].

In most of these cases the prior knowledge is empirically defined based on observation, such as seeing that images are sparse after a finite differences transform. To our knowledge, the use of datasets of scans to automatically optimize MRI acceleration methods such as CS has been limited. In contrast, in image processing fields such as image segmentation the use of explicit prior knowledge in the form of annotated datasets has been very successful, for example in atlas-based segmentations [19], statistical shape models [20], and supervised machine learning [21]. In **Chapter 2** of this thesis we analyze the potential of using such datasets for optimizing the undersampling patterns for applying CS to specific anatomies.

## 1.6 Metal devices in MRI

One of the main goals of the studies presented in this thesis was to perform accurate localization of metal devices in MR images using the off-resonance artifacts caused by such devices.

Generally, the presence of metal in MRI is considered problematic. In the worst case, devices such as metal orthopedic implants or pacemakers are not safe in the strong magnetic fields of MRI scanners, leading to exclusion of patients from undergoing MRI exams. Even in the best case, metal devices will cause off-resonance artifacts in conventional MRI acquisitions.

The presence of materials with a magnetic susceptibility different from the magnetic susceptibility of background tissue perturbs the main magnetic field proportionally to both the susceptibility difference and the field strength. These perturbations are often called off-

resonance effects, because it will cause spins to precess at frequencies other than the Larmor frequency. Because the entire MR imaging process is based on the assumption that spins precess at the Larmor frequency, the presence of off-resonance effects leads to several types of artifacts, including spatial distortion, signal loss due to intra-voxel dephasing, and signal loss due to imperfect RF excitation.

The presence of off-resonance effects interferes with the frequency encoding process, because both encoding gradients and off-resonance effects affect the precession frequency. The latter will cause spatial distortions, where signal is shifted in the frequency encoding direction proportional to the off-resonance. The shift in pixels ( $\Delta x$ ) at location  $r$  is defined as follows:

$$\Delta x(r) = \frac{\Delta B_0(r)\gamma}{BW_{read}} \quad (1.2)$$

Here,  $\Delta B_0$  is the magnetic field offset in tesla,  $\gamma$  is the Larmor frequency in Hz/T, and  $BW_{read}$  is the readout bandwidth in Hz/pixel (i.e. the rate at which signal is sampled). From this definition it directly follows that spatial distortion will increase around objects that cause larger off-resonance effects, i.e. larger objects or objects with stronger magnetic susceptibility.

In gradient echo scans off-resonance effects also cause dephasing of the MR signal. The phase difference ( $\Delta\phi$ ) that accumulates depends on both the strength of the off-resonance and the echo time ( $TE$ ):

$$\Delta\phi(r) = \Delta B_0(r)\gamma TE \quad (1.3)$$

If this dephasing effect is strong enough it will cause signals within a single voxel to have strongly varying phases. When added together, signals with different phases will (partially) cancel out, which causes signal loss.

Physically, magnetic susceptibility effects are well understood. When a spherical object is placed in a strong magnetic field, the off-resonance induced by magnetic susceptibility effects is defined by the dipole function. Non-spherical objects such as orthopedic implants will cause off-resonance effects with more complicated shapes. This off-resonance can be calculated efficiently if the model and magnetic susceptibility properties of the object are known [22]. Figure 1.5 shows the off-resonance artifacts in an MRI scan of the femoral component of a total knee replacement implant and the simulated off-resonance effects based on a model of the same implant.

Because artifacts around metal objects reduce the diagnostic quality of images, research has focused on reducing the impact of metal artifacts around objects like orthopedic implants. For example, imaging with strong readout gradients and short echo times can reduce the size of artifacts [23]. Another smart way to mitigate spatial distortions is view-angle-tilting, a method in which the slice selection gradient is repeated during readout to compensate for off-resonance effects [24]. More advanced methods, such as MAVRIC [25] and SEMAC [26], use longer, specialized pulse sequences to resolve signals affected by strong magnetic susceptibility effects.

Although in general clinical practice metal artifacts detract from image quality, there are applications where localization of metal objects is the primary objective, and imaging tissue around the objects is sometimes of lesser importance. These applications include localization of fiducial markers [27] and small devices such as brachytherapy seeds [28],

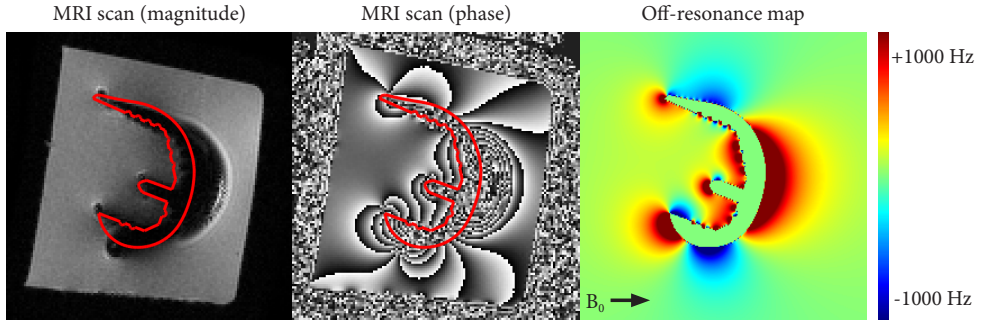


**FIGURE 1.5:** MRI scan (magnitude and phase) and simulated off-resonance map for the femoral component of an Oxinium<sup>TM</sup> total knee replacement implant.

tracking of interventional devices during MR-guided interventions [29], and localization of implants for validation of implantation procedures. In these situations the artifacts around the object can serve as a source of information about the position and orientation of the object. In **Chapters 3 to 5** we present studies that attempt to solve this type of localization problem using susceptibility models of the objects as prior knowledge.

## 1.7 Thesis outline

In **Chapter 2**, we evaluate different undersampling strategies for CS. We discuss optimization of variable density undersampling and compare this with a data-driven approach that designs an undersampling pattern using datasets of previously acquired scans as prior knowledge.

In **Chapter 3**, we propose a method to accelerate simulation of off-resonance artifacts in MRI by using the fast Fourier transform. Furthermore, we show that these fast simulations can be used to localize metal objects using a template matching approach, if an exact model of the object is available as prior knowledge.

In **Chapter 4**, we utilize the methodology from **Chapter 3** to perform MR-only localization of brachytherapy seeds in the prostate of prostate cancer patients for postimplant dosimetry in low dose-rate brachytherapy. The accuracy of the localization results was verified against CT scans and we identified sources of errors in the MR-only approach.

Finally, in **Chapter 5**, we combine the concept of undersampled MRI with localization of metal devices to achieve real-time passive tracking of such devices in 2D scans.



## EVALUATION OF VARIABLE DENSITY AND DATA-DRIVEN K-SPACE UNDERSAMPLING FOR COMPRESSED SENSING MRI

**Based on:**

F. Zijlstra, M. A. Viergever, and P. R. Seevinck, "Evaluation of Variable Density and Data-Driven K-Space Undersampling for Compressed Sensing Magnetic Resonance Imaging," *Investigative Radiology*, vol. 51, pp. 410–419, June 2016.

### Abstract

The aim of this study was to investigate the influence of variable density and data-driven  $k$ -space undersampling patterns on reconstruction quality for Compressed Sensing (CS) MRI to provide recommendations on how to avoid suboptimal CS reconstructions. First, we investigated the influence of randomness and sampling density on the reconstruction quality when using random variable density and variable density Poisson disk undersampling. CS reconstructions on one knee and two brain datasets were compared to fully sampled datasets and reconstruction errors were measured. Sampling coherence was evaluated on the undersampling patterns to investigate whether there was a relation between this coherence measure and reconstruction error.

Second, we investigated whether data-driven undersampling methods could improve reconstruction quality, when one or more fully sampled scans are available as a training set. We implemented three different data-driven undersampling methods: (1) Monte-Carlo optimization of variable density and variable density Poisson disk undersampling, (2) calculating sampling probabilities directly from the  $k$ -space power spectra of the training data, and (3) iterative design of undersampling patterns based on CS reconstruction errors in  $k$ -space. Two cross-validation experiments were set up using retrospective undersampling to evaluate the three data-driven methods and the influence of the size of the training set. Furthermore, in an experiment that included prospective undersampling we show the practical applicability of two of the data-driven methods. CS reconstruction quality was measured with both the Normalized Root Mean Squared Error metric and the mean Structural Similarity Index Measure.

Different optimal variable sampling densities were found for each of the datasets, showing that the optimal sampling density is data-dependent. Choosing a sampling density other than the optimal density decreased reconstruction quality. These results suggest that choosing a sampling density without having any reference scans is likely suboptimal. Furthermore, no meaningful correlation was found between sampling coherence and reconstruction error. For the data-driven methods, the iterative method yielded statistically significantly higher reconstruction quality in both retrospective and prospective experiments. In retrospective experiments, the power spectrum method yielded a reconstruction quality that was comparable with the data-driven variable density method. The size of the training set had only a minor influence on the reconstruction quality.

These results show that data-driven undersampling methods can be used to avoid suboptimal reconstruction quality in CS MRI, provided that at least one fully sampled scan is available to train the data-driven method. The iterative design method resulted in the highest reconstruction quality.

## 2.1 Introduction

In the field of Magnetic Resonance Imaging (MRI), Compressed Sensing (CS) is a relatively new and promising technique to accelerate the data acquisition process. Conventionally, a fully sampled  $k$ -space - in accordance with the Nyquist sampling criterion - is required to reconstruct an MR image without aliasing. However, CS enables reconstruction of an MR image from an undersampled  $k$ -space, thereby violating the Nyquist criterion, by exploiting the fact that MR images are often sparse in some transform domain (e.g. the finite differences or wavelet transform) [10].

In their initial work on CS MRI, Lustig et al. reported acceleration factors up to 5-fold with only a minor decrease in image quality [10]. In clinical practice, this acceleration might help reduce costs, reduce patient burden and/or increase scan resolution [30]. However, clinical adoption of CS MRI has been slow, in part because of the following two reasons. First, CS requires the use of non-linear reconstruction algorithms, which may dramatically increase reconstruction times beyond what is practical for daily clinical use. Second, CS can produce subtle artifacts, such as the loss of low-contrast features or compression artifacts similar to those that occur with JPEG compression [10,31], which may mask clinically relevant image characteristics.

To some degree, these artifacts are unavoidable insofar as they are directly related to the acceleration factor. However, these artifacts are also affected by the choice of the sparse domain,  $k$ -space undersampling pattern, and reconstruction algorithm [31]; choosing these suboptimally for a specific application may lead to an unnecessary increase of these CS artifacts.

Whereas a lot of research has focused on sparse domains (e.g.: Candès et al. [32,33]) and CS reconstruction algorithms (e.g. Beck and Teboulle [34] and Lustig and Pauly [12]), relatively little research has focused on  $k$ -space undersampling patterns for CS. In general, random undersampling is assumed sufficient to get high-quality reconstructions, based on mathematical guarantees from early CS theory [35].

Variable density (VD) random  $k$ -space undersampling is commonly used because it has been empirically shown that VD undersampling yields a higher reconstruction quality than uniform random undersampling does for many medical images [10]. The rationale behind VD undersampling is that low-frequency  $k$ -space coefficients contain more energy and must therefore be sampled more densely than high-frequency coefficients. Although a variable sampling density can be defined in many different ways, a common choice is to let the sampling probability decay with a power of the distance to the center of  $k$ -space [10], where the power is a parameter that defines the sampling density. However, there is currently no proven strategy to choose this sampling density optimally. In addition, many authors do not report the sampling density they used [18,36,37] or give it without motivation [10,38,39].

Even with a well-chosen sampling density, random sampling can create large variations in the generated undersampling patterns. Lustig et al. state that an undersampling pattern should be incoherent; that is, the point spread function (PSF) resulting from the  $k$ -space undersampling should be noise-like outside the central peak [10]. In their work, coherence was defined as the maximum sidelobe-to-peak ratio of the PSF [10]. This measure, referred to as the sampling coherence in this work, can be used to select the most incoherent undersampling pattern from a large number of randomly generated undersampling patterns. However, no proof exists that this approach systematically reduces reconstruction errors.

Others have suggested methods that avoid these problems, by using one or more fully

sampled (i.e. unaccelerated) scans as prior knowledge [40–42]. In this study, we will refer to these methods as data-driven methods. The advantages of such data-driven methods include the fact that they generally reduce the number of user-chosen parameters, for example, the sampling density. Furthermore, prior knowledge may be used to improve CS reconstruction quality for a specific scan protocol and anatomical region. For example, Knoll et al. proposed a method that eliminates the sampling density parameter by computing a probability density function (PDF) directly from a fully sampled reference image. In their work, the PDF was defined as the normalized k-space power spectrum of the reference image [40]. In other words, the more energy there is in a k-space coefficient, the more likely it is that it will be included in the undersampling pattern. A different approach was taken by both Liu et al. [41] and Ravishankar and Bresler [42], who have described methods that do not explicitly construct a PDF; instead, they directly design undersampling patterns based on reconstruction errors in k-space. The k-space coefficients with the highest errors after a CS reconstruction are assumed to be the best coefficients to add to an undersampling pattern. This concept is then used to design an undersampling pattern from scratch [41], or to refine an existing undersampling pattern [42]. Seeger et al. have proposed a method that could design an undersampling pattern while scanning, based on the data acquired so far [43]. An advantage of this approach is that no fully sampled scans are required a priori. However, for large 3D scans the computational requirements of this method are impractical.

A common limitation of the studies that propose these data-driven methods is that the datasets used to test the methods were small and homogeneous. In addition, comparisons to other undersampling methods were limited. In the presented work, we aim to address both aspects. The goal of this study was to investigate the influence of VD and data-driven undersampling patterns on CS reconstruction quality using large datasets. The study consisted of two parts: First, we analyzed the differences in reconstruction quality that could arise from using random VD undersampling patterns with different sampling densities. With this analysis, we intended to gain insight into the potential loss of reconstruction quality due to suboptimally chosen undersampling patterns. Simultaneously, this analysis allowed us to investigate the possible relationship between sampling incoherence and reconstruction quality. Second, we investigated whether data-driven undersampling methods could improve the reconstruction quality of future scans of a specific anatomy, provided that a representative set of fully sampled scans of other subjects is available. To that end, we implemented and compared three data-driven undersampling methods: (1) a data-driven variant of VD undersampling using Monte-Carlo optimization, (2) the method of Knoll et al. based on the k-space power spectrum, and (3) an iterative design method based on the method of Liu et al. These methods were evaluated in two experiments using retrospective undersampling on a knee and brain dataset, using leave-one-out cross-validation to ensure generalization of the results to future data. In addition, methods 1 and 3 were tested in a prospective experiment that included parallel imaging, to demonstrate the practical applicability of the methods.

## 2.2 Materials & Methods

### 2.2.1 Materials

Two large datasets were obtained to enable a thorough analysis of different undersampling methods. To be suitable for realistic retrospective 3D CS experiments, these datasets should

ideally meet the following criteria:

1. The acquisition protocol should not include prospective k-space undersampling (e.g. zero-filling or partial Fourier k-space coverage).
2. The stored image data must be complex-valued.
3. The image dimensions must be such that the two phase encoding directions are large enough to allow undersampling.

The first dataset was a knee dataset acquired at 3 tesla (GE Healthcare, Milwaukee, WI), provided by Epperson et al. [44, 45]. It consisted of fully sampled 3D proton density weighted spin echo scans of 20 healthy subjects (matrix size  $320 \times 320 \times 256$ , resolution  $0.5 \times 0.5 \times 0.6$  mm, TE/TR 25/1550, echo train length = 40, 8 coils, spherical shutter). The multicoil datasets were reconstructed using a self-calibrated parallel imaging reconstruction [46], as implemented by Uecker et al. [47]. Figure 2.1A shows a slice in the phase encoding plane of one of the images from this dataset.

The second dataset was a series of brain scans acquired at 7 tesla (Achieva, Philips Healthcare, Cleveland, USA). It consisted of 3D  $T_2^*$  weighted gradient echo scans of 7 healthy subjects (matrix size  $480 \times 381 \times 300$ , resolution  $0.5 \times 0.5 \times 0.5$  mm, TE/TR = 27/70, EPI factor = 13, SENSE (LR) = 2.3, 16 coils) [48]. Figure 2.1B shows a slice in the phase encoding plane of one of the images from this dataset.

Both the spherical shutter in the knee dataset and the SENSE factor in the brain dataset violate our first requirement. However, we limited the influence of the spherical shutter on our experiments by ensuring that our retrospective experiments did not sample locations outside the spherical shutter.

The original SENSE reconstruction in the brain dataset may have affected noise and other image characteristics. Upon visual inspection of the images and their k-space representations, we concluded that the information content of the images covered most of the full original resolution. Therefore, although not ideal, we decided that the dataset could be used for retrospective undersampling experiments that did not include parallel imaging. Importantly, the CS reconstruction errors in our experiments will be calculated in relation to the original reconstructed images. Therefore, any changes to the image characteristics will be present in the reference standard and should affect all experiments equally.

Furthermore, we presumed that any influences that these imperfections may have had were equal for all evaluated undersampling patterns; that is, no bias was introduced.

Finally, we acquired a set of 3D T1-weighted brain scans (matrix size  $240 \times 192 \times 266$ , resolution  $1 \times 1 \times 1$  mm, TE/TR 3.7/20, 16 coils) at 1.5 tesla (Ingenia, Philips Healthcare, Best, The Netherlands) on two healthy subjects who gave written informed consent, in accordance to the institutional review board of the University Medical Center Utrecht. This experiment will be referred to as the prospective experiment. In the first subject, we acquired a fully sampled scan (scan time 17:01 minutes). In the second subject, we acquired both a fully sampled scan and three prospectively undersampled scans using an undersampling factor of 8 (scan time 2:07 minutes). Figure 2.1C shows a slice in the phase encoding plane of the fully sampled scan on the first subject.

## 2.2.2 Compressed Sensing reconstruction

A CS reconstruction attempts to find the sparsest image that is consistent with the acquired undersampled data. For MR images, sparsity is commonly maximized in the finite difference

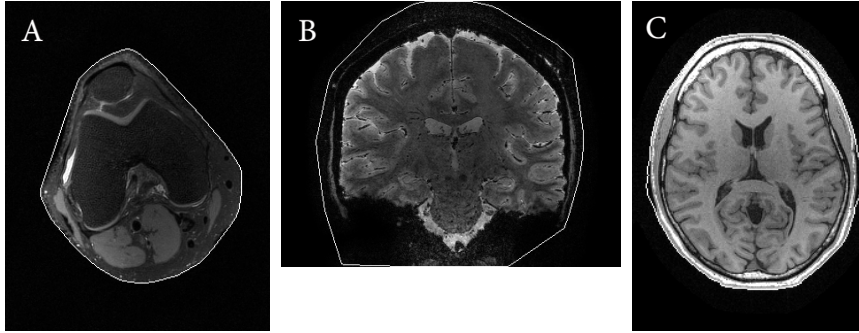


**FIGURE 2.1:** Single slice in the phase encoding plane from the knee (A) and brain (B) datasets, and the brain scan on the first subject of the prospective experiment (C). The edge of an automatically defined region of interest is indicated by the white border.

domain and/or a wavelet domain [10]. In this study, we used both these domains.

Mathematically, CS reconstruction can be expressed as solving the following unconstrained minimization problem:

$$\underset{x}{\text{minimize}} \|F_u x - y\|_2^2 + \lambda TV(x) + \lambda \|Wx\|_1 \quad (2.1)$$

Here,  $x$  is the image to be reconstructed,  $y$  is the acquired data,  $F_u$  is the undersampled Fourier operator,  $TV$  is the  $\ell_1$  norm of the finite differences in each image dimension, also known as total variation regularization, and  $W$  is a wavelet operator, in our case the Daubechies-6 wavelet [49]. This minimization enforces consistency with the acquired data, while promoting sparsity in the finite difference and wavelet domains. We used the Split Bregman method to solve this problem efficiently [50].

For CS reconstruction of the multicoil data in the prospective experiment, we used the ESPIRiT method [51], as implemented in the Berkeley Advanced Reconstruction Toolbox (BART) [52, 53]. It uses the Fast Iterative Shrinkage Thresholding Algorithm (FISTA) [34] to solve the following problem:

$$\underset{x^1 \dots x^M}{\text{minimize}} \sum_{i=1}^N \|F_u \sum_{j=1}^M S_i^j x^j - y_i\|_2^2 + \lambda \sum_{j=1}^M \|Wx^j\|_1 \quad (2.2)$$

Here,  $x^j$  is the  $j$ th image component and  $S_i^j$  are the coil sensitivities for the  $i$ th coil and  $j$ th image component. We take  $x^1$  as the final reconstructed image (out of the 2 components used by default), as suggested by Uecker et al. [51].

The regularization weight  $\lambda$  controls how much sparsity may be introduced at the cost of consistency with the acquired data. In this study,  $\lambda$  was chosen using a parameter sweep on CS reconstructions of a single image from each dataset, resulting in a unique  $\lambda$  for each dataset.

### 2.2.3 Analysis of variable density random undersampling

The first goal in our study was to investigate the influence of different sampling densities and random sampling on CS reconstruction quality when using variable density (VD) ran-

dom undersampling. Variable density undersampling commonly uses a probability density function (PDF) that decays with the distance to the center of k-space according to a power distribution [10, 40]. We used the following definition of the PDF, similar to the one used by Knoll et al. [40]:

$$P(k_x, k_y) = \max((1 - \sqrt{k_x^2 + k_y^2}), 0)^d \quad (2.3)$$

Here,  $k_x$  and  $k_y$  are the k-space coordinates scaled between -1 and 1. The power  $d$  defines the sampling density; for example, higher values of  $d$  will result in denser sampling near the k-space center, which we refer to as a higher sampling density. Undersampling patterns were generated using this PDF by performing random sampling without replacement until the requested undersampling rate was achieved. The sampling density  $d$  was varied between 1.0 and 4.0 with steps of 0.25, empirically chosen based on initial experiments. Per sampling density we generated 25 random undersampling patterns, adding up to a total of 325 patterns. These patterns were used to retrospectively undersample the knee and brain datasets, followed by CS reconstruction.

In the case of parallel imaging CS reconstruction, the inclusion of structural undersampling is beneficial because it allows exploiting the coil geometry and sensitivity profile, similar to SENSE or GRAPPA. Variable density Poisson disk (VDPD) sampling is a commonly used method to achieve a mix between structural undersampling and VD random undersampling [13], by enforcing a minimum distance between randomly chosen sampling locations.

We retrospectively undersampled the fully sampled scans from the prospective experiment with 100 random VDPD undersampling patterns. The sampling densities were varied between 0 and 2.5 with 10 steps (i.e. steps of 2.5/9), empirically chosen based on initial experiments. Per sampling density we generated 10 random undersampling patterns.

The CS reconstruction errors resulting from both these VD undersampling experiments were measured with the Normalized Root Mean Squared Error (NRMSE) metric. The variation in these errors will show the effect of both the sampling density and the randomness in the patterns.

For all these patterns, we calculated the sampling coherence as defined by Lustig et al. [10]. Sampling coherence was measured as the maximum sidelobe-to-peak ratio of the PSF resulting from the undersampling, where a lower sampling coherence indicates a more incoherent undersampling pattern. We found the transform PSF mentioned in the study of Lustig et al. [10] to be impractical for this purpose because it requires the calculation of thousands of Fourier and wavelet transforms.

Using Spearman rank correlation test [54] we tested whether there was any positive correlation between sampling coherence and the reconstruction errors. This test was applied to both the complete set of sampling patterns and for each sampling density individually.

### 2.2.4 Data-Driven undersampling

The second goal in our study was to investigate whether data-driven undersampling methods could improve CS reconstruction quality for future scans, provided that a representative training set of fully sampled scans of other subjects is available. The next subsections describe the three data-driven undersampling methods we assessed in this work. All methods required a fully sampled training set and all methods were implemented such that they

yielded a single undersampling pattern. The training sets will be defined in the “Experimental Setup” section.

### Data-driven variable density undersampling

First, we used Monte-Carlo optimization to find a random VD or VDPD undersampling pattern with the lowest NRMSE reconstruction error on the training set. We reused the 325 VD (for the knee and brain datasets) and 100 VDPD (for the prospective experiment) undersampling patterns from the initial analysis of VD undersampling because we already calculated the reconstruction errors resulting from CS reconstruction using each of these patterns. The pattern with the lowest mean NRMSE reconstruction error on the training set was then selected as the best VD undersampling pattern. By using this approach, we optimized both the sampling density and the randomness within the undersampling patterns for the given training set.

### Power spectrum undersampling

Second, we implemented the method of Knoll et al defining a PDF using the *k*-space power spectrum of a given reference image [40]. In our case, the training set could contain multiple 3D scans. Therefore, we calculated the average power spectrum over both the Fourier transformed readout direction and over all scans in the training set, resulting in a single 2D power spectrum. This power spectrum was normalized between 0 and 1 to obtain the PDF. We used a Monte-Carlo optimization to find a random undersampling pattern generated from this PDF with the lowest NRMSE reconstruction error on the training set. The number of randomly generated patterns was 25.

Power spectrum undersampling was not applied in the prospective experiment because there is currently no method that combines this principle with structural undersampling for parallel imaging.

### Iterative undersampling design

Finally, we used an iterative undersampling design method based on the method proposed by Liu et al [41]. For a given CS reconstruction, the unsampled *k*-space locations associated with the highest reconstruction errors are assumed to add the most information [41]. Consequently, if those locations are added to the undersampling pattern, this is assumed to reduce the reconstruction errors the most [41].

In contrast to Liu et al, we did not make a distinction between low- and high-frequency *k*-space components because it adds a user-defined parameter to the method. Instead, we used the following procedure for designing an undersampling pattern, which is identical to the “Batch-optimization” stage of the algorithm of Liu et al [41]. We refer to the undersampling pattern as *S* and initialize it as a set containing only the central *k*-space location.

1. Reconstruct the training set using retrospective undersampling with *S*.
2. For every candidate *k*-space location, measure the residual mean squared error over the entire training set.
3. Add the *K* *k*-space locations with the highest errors to *S*.

4. Repeat steps 1 through 3 until  $S$  contains enough elements to satisfy the undersampling rate.

Because the prospective experiment required parallel imaging CS reconstruction, structural undersampling needed to be included (similar to the VDPD undersampling patterns). For this purpose, we added an extra constraint to the iterative method: in each iteration, once a location is added, no other locations may be chosen in a  $3 \times 3$  neighborhood around the added location, which promotes structural undersampling. This constraint resets every iteration to ensure that nonstructural undersampling can still be generated over multiple iterations.

Ideally, the method should evaluate the effect of adding each  $k$ -space location individually (i.e.  $K = 1$ ), but in most cases, this is not computationally feasible. In our experiments we chose  $K$  such that the algorithm finishes after 100 iterations, resulting in  $K = 205$  for the knee dataset,  $K = 288$  for the brain dataset, and  $K = 64$  for the prospective experiment.

### 2.2.5 Experimental setup

In our retrospective CS experiments on the brain and knee datasets the fully sampled  $k$ -spaces were retrospectively undersampled in the phase encoding plane by a factor of 4. In case of the knee dataset this undersampling was on top of the undersampling already present because of the spherical shutter, resulting in a factor of  $16/\pi$ . In the prospective, parallel imaging experiment, the undersampling factor was chosen to be 8. The frequency encoding direction always remained fully sampled.

The CS reconstruction errors were evaluated using two metrics. The first metric was the Normalized Root Mean Squared Error (NRMSE), defined as the Root Mean Squared Error divided by the magnitude range of the reference image:

$$NRMSE = \frac{1}{\max(|y_i|; i = 1..n) - \min(|y_i|; i = 1..n)} \sqrt{\sum_{i=1}^N |x_i - y_i|^2} \quad (2.4)$$

Here,  $x$  is the reconstructed image and  $y$  the reference image. The second metric was the mean Structural Similarity Index Measure (mSSIM), proposed by Wang et al as an error metric that is more consistent with human perception [55].

Both measures were evaluated only on the regions of the image with signal, to avoid measuring errors in noise outside the subject. Per reference image, the region of interest was defined as the convex hull of all voxels with a magnitude higher than the mean voxel magnitude over the entire image. Figure 2.1 shows an example of the region of interest for each of the datasets.

### Data-driven undersampling

On the knee and brain datasets, we set up two different data-driven undersampling experiments with a different number of subjects in the training sets. The first experiment was a leave-one-out cross-validation experiment; that is, undersampling patterns were designed based on all but one of the subjects in the dataset (19 out of 20 subjects for the knee dataset, 6 out of 7 subjects for the brain dataset). Reconstruction errors were then calculated for the subject that was left out. The experiment was repeated such that each subject was left

out once. This experiment simulated a situation where there is plenty of fully sampled data available for training.

However, having to acquire many fully sampled scans for training is highly impractical. Therefore, in the second experiment, we simulated a situation where there is only a single fully sampled scan available for training. We used the same cross-validation methodology as in the first experiment, except that the subject that was left out was now used for training. As a result, each subject's scan was reconstructed multiple times, once for every other subject in the dataset. Both the mean reconstruction error and the worst-case reconstruction error per subject were reported.

In addition to the data-driven undersampling methods, low resolution sampling (i.e. sampling only the center of *k*-space) was evaluated with the same undersampling rates. Although the low resolution data could be reconstructed with a normal linear reconstruction, we did apply a CS reconstruction to ensure that differences in reconstruction quality were only a result of the undersampling pattern and not the reconstruction method.

Differences in mean reconstruction errors were tested for significance using paired *t* tests (paired per subject) at a 5% level of significance, both between experiments and between undersampling methods.

In the prospective experiment, we first acquired a fully sampled scan on the first subject to serve as the training set for the data-driven VDPD and iterative design methods, yielding two optimized undersampling patterns. In addition, a  $2 \times 2$  structural undersampling pattern was generated (similar to what could be used for 4-fold SENSE or GRAPPA acceleration), with the resolution restricted using a spherical shutter to achieve the desired undersampling factor of 8. In the second subject, three scans were acquired with prospective undersampling using these three undersampling patterns (structural undersampling, data-driven VDPD and iterative design). A fully sampled scan was also acquired to serve as a reference for comparison. In addition, the same three undersampling patterns were also applied retrospectively to the fully sampled scan and reconstructed. The reconstructions of the prospectively undersampled scans were registered to the fully sampled scan to correct for subject motion in between scans. The registration was performed using Elastix [56] and allowed only a rigid transformation (i.e. only translation and rotation).

## 2.3 Results

### 2.3.1 Analysis of variable density undersampling

Figure 2.2 shows the influence of different sampling densities as well as of the process of random sampling on NRMSE reconstruction errors for VD random undersampling on both the knee (A) and brain (B) datasets, and for VD Poisson Disk undersampling applied retrospectively to the fully sampled scan of the second subject in the prospective experiment (C). Each data point represents one random undersampling pattern drawn from a variable sampling density  $d$  (annotated in Figure 2.2). For each undersampling pattern, the NRMSE reconstruction error (vertical) and sampling coherence (horizontal) are shown.

The primary source of variation in reconstruction errors seemed to be the choice of the sampling density. On average, the best undersampling patterns were found with sampling density  $d = 2$  for the brain dataset,  $d = 2.25$  for the knee dataset, and  $d = 0.56$  for the prospective experiment. The single best undersampling pattern was found with  $d = 1.75$  for the brain dataset,  $d = 2$  for the knee dataset, and  $d = 0.56$  for the prospective experi-

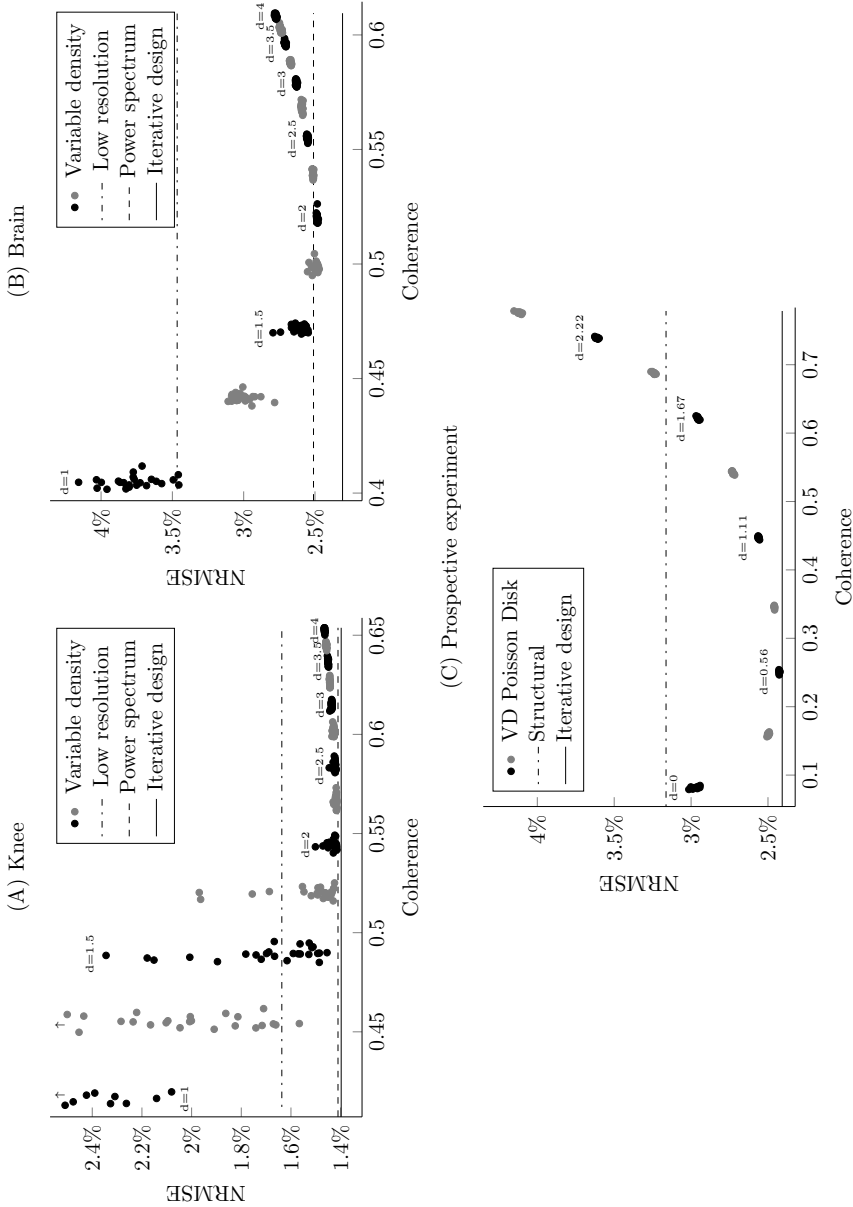


**FIGURE 2.2:** Normalized Root Mean Squared Error (NRMSE) reconstruction results from the analysis of variable density random undersampling patterns for the knee (A) and brain (B) datasets, and variable density Poisson disk undersampling patterns for the prospective experiment (C). Each data point represents one random variable density undersampling pattern. Sampling densities are annotated as  $d$  (shown every 0.5 in panels A and B, every 0.56 in panel C) and alternating shades indicate different undersampling patterns. The horizontal axis shows the sampling coherence for each undersampling pattern (i.e. the most incoherent patterns are on the left). For the knee dataset,  $\uparrow$  indicates 16 data points for  $d = 1$  and 2 data points for  $d = 1.25$  that were omitted because of scaling. For reference, horizontal lines show mean reconstruction errors for low resolution sampling, for the power spectrum method, and for the iterative design method from the first data-driven experiment (A/B, Table 2.1, experiment 1), and structural undersampling and iterative design from the prospective experiment (C, Table 2.2, retrospective).

ment. The second source of variation in reconstruction errors was random sampling, which showed larger variations for lower sampling densities than for higher sampling densities for the brain and knee datasets. In the retrospective results of the prospective experiment, the variations were much smaller, although they slightly increased when moving away from the optimal sampling density.

We found that increasing the sampling density  $d$  led to an increase in coherence, as clearly shown in Figure 2.2, where the clusters of data points for increasing sampling densities were perfectly ordered from left to right (i.e. low coherence to high coherence). In contrast, in general, there was no significant positive correlation between sampling coherence and reconstruction errors; that is, more incoherent undersampling patterns did not necessarily lead to a lower reconstruction error.

When we tested the correlation for each sampling density individually, a significant positive correlation ( $P < 0.05$ ) between sampling coherence and reconstruction error was found for most sampling densities that were higher than the optimal sampling density. For both the knee and brain datasets significant positive correlation was found for  $d = 3.25$ ,  $d = 3.5$ ,  $d = 3.75$  and  $d = 4$ . In addition, for the brain dataset, significant positive correlation was found for  $d = 2$  and  $d = 2.5$ . For the prospective experiment, significant positive correlation was found for  $d \geq 1.11$ .

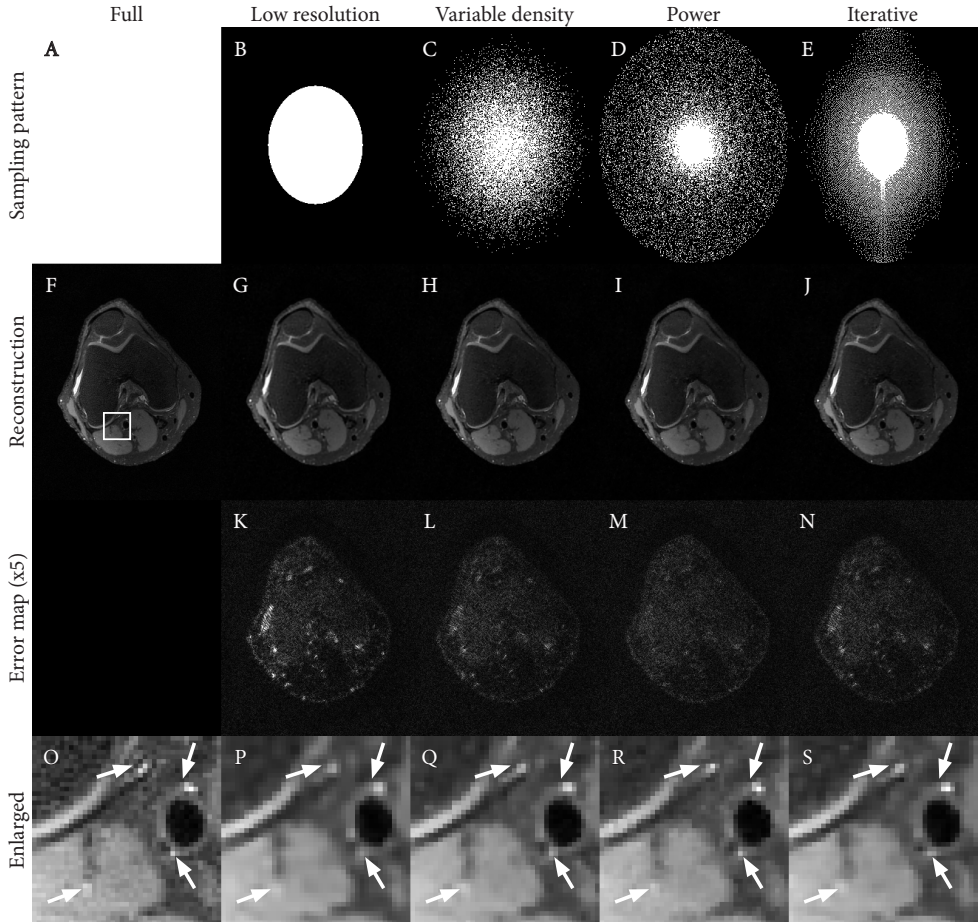
### 2.3.2 Data-driven undersampling

Table 2.1 shows the mean reconstruction errors and mean mSSIM values for the data-driven undersampling experiments for the knee and brain datasets. In all experiments, the iterative design method yielded statistically significantly better reconstruction results according to both error metrics. The differences between data-driven VD undersampling and the power spectrum method were small and in some cases not significantly different ( $P < 0.05$ ). The differences between experiment 1 (large training set) and experiment 2 (single subject training set) were also small on average. As expected, the worst-case results for experiment 2 showed slightly larger errors for all methods.

The large difference in NRMSE and mSSIM values between the knee and brain datasets can be attributed to the fact that both metrics were normalized using the maximum magnitude of the reference image. The knee dataset contained some very high-magnitude peaks, whereas the mean magnitude was much lower (Fig. 2.3F), leading to lower normalized errors. In the brain dataset the magnitudes were more evenly distributed (Fig. 2.4F), which led to higher normalized errors.

Figures 2.3 and 2.4 show examples of the resulting undersampling patterns and reconstructed images for experiment 1. These qualitative results were harder to interpret, as we found that reconstruction quality varied locally per undersampling method and per dataset. In general, the qualitative results corresponded to the quantitative results. In the error maps for all methods (Figs. 2.3K to N and 2.4K to N), the number of large errors and the overall magnitude of the errors decreased with decreasing NRMSE (Table 2.1). A notable exception was the error map for the power spectrum method on the knee dataset (Fig. 2.3M). For this case, the errors were more noise-like than for the data-driven VD and iterative design methods, although the magnitude of the errors was slightly higher. In addition, there were fewer large errors (Fig. 2.3M).

Table 2.2 shows the NRMSE reconstruction errors and mSSIM values for the prospective experiment and the corresponding reconstructions using retrospective undersampling.



**FIGURE 2.3:** Knee reconstruction results for the data-driven undersampling methods. Fully sampled image (F) with enlarged region (O) indicated. Undersampling pattern (first row), reconstructed image (second row), absolute reconstruction errors times 5 (third row) and enlarged region (fourth row) are shown for low resolution undersampling (B, G, K, P), the data-driven VD method (C, H, L, Q), the power spectrum method (D, I, M, R), and the iterative design method (E, J, N, S). Arrows indicate features with strongly varying reconstruction quality.

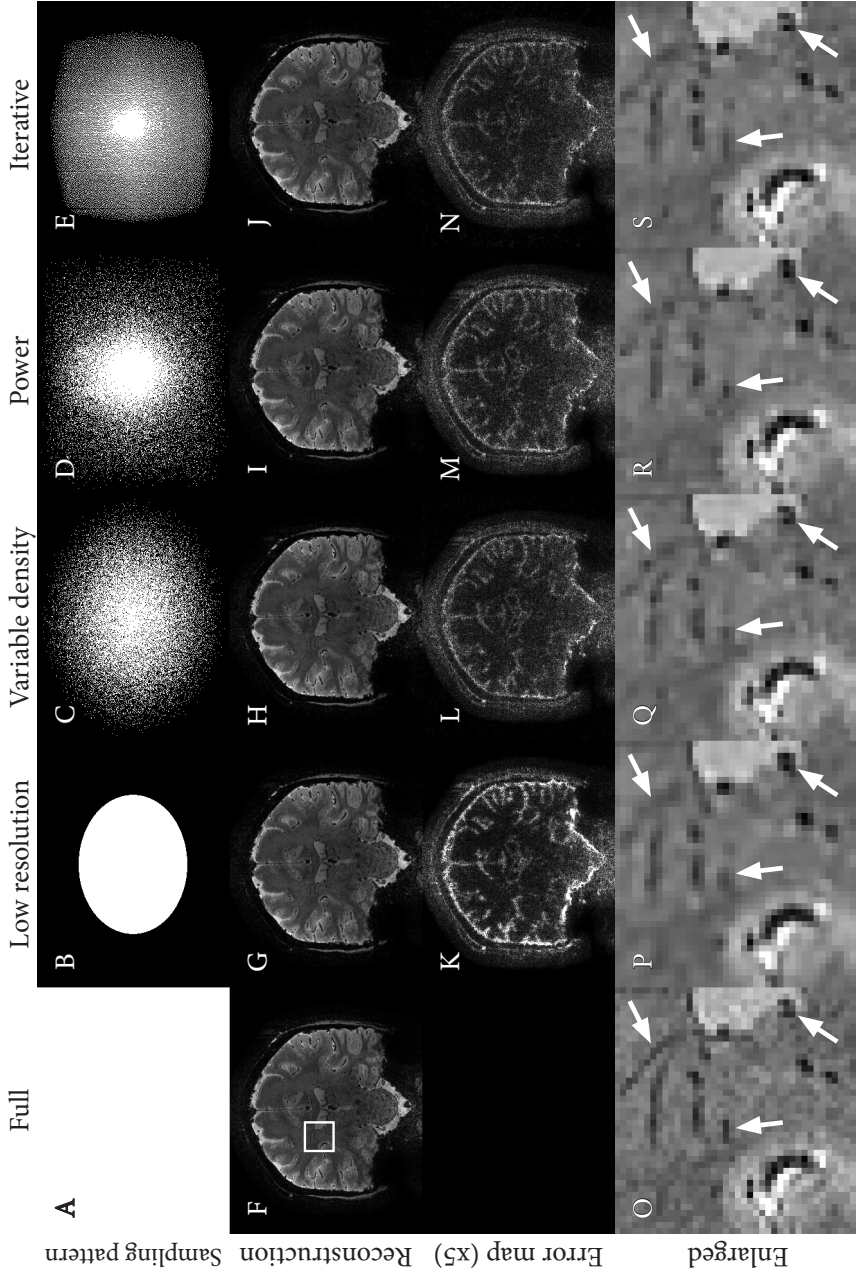


**FIGURE 2.4:** Brain reconstruction results for the data-driven undersampling methods. Fully sampled image (F) with enlarged region (O) indicated. Undersampling pattern (first row), reconstructed image (second row), absolute reconstruction errors times 5 (third row) and enlarged region (fourth row) are shown for low resolution undersampling (B, G, K, P), the data-driven VD method (C, H, L, Q), the power spectrum method (D, I, M, R), and the iterative design method (E, J, N, S). Arrows indicate features with strongly varying reconstruction quality.

Dataset	Experiment	Low res.	VD	Power	Iterative
NRMSE					
Knee	1	1.637%	1.418% ↓ ↔	1.413% ↔	<b>1.399%</b> ↓
	2 (mean)		1.419% ↓	1.411%	<b>1.398%</b> ↓
	2 (worst)		1.438%	1.417% ↔	<b>1.415%</b> ↔
Brain	1	3.466%	2.479% ↓	2.517%	<b>2.290%</b>
	2 (mean)		2.480% ↓	2.510%	<b>2.307%</b>
	2 (worst)		2.492% ↔	2.523% ↔	<b>2.337%</b>
mSSIM					
Knee	1	0.9679	0.9738 ↓	0.9730	<b>0.9744</b>
	2 (mean)		0.9738 ↓	0.9731	<b>0.9741</b>
	2 (worst)		0.9734	0.9729	<b>0.9736</b>
Brain	1	0.9355	0.9499 ↓	0.9486	<b>0.9536</b>
	2 (mean)		0.9499 ↓	0.9487	<b>0.9528</b>
	2 (worst)		0.9493 ↔	0.9484 ↔	<b>0.9510</b>

**TABLE 2.1:** Normalized Root Mean Squared Error (NRMSE) and mean Structural Similarity Index Measure (mSSIM) values for the data-driven undersampling experiments: Experiment 1 was trained using all but one subject and experiment 2 was trained using only a single subject, for which both the mean and worst case values are shown. Values are shown for the following methods: Low resolution undersampling (Low res.), the data-driven variable density method (VD), the power spectrum method (Power), and the iterative design method (Iterative). Pairs of values marked with ↓ were not significantly different ( $P < 0.05$ ) from each other within the same column (same method, different experiments). Pairs of values marked with ↔ were not significantly different ( $P < 0.05$ ) from each other within the same row (same experiment, different methods)

	Experiment	Structural	VDPD	Iterative
NRMSE				
	Retrospective	3.163%	2.423%	2.407%
	Prospective	5.416%	5.302%	4.783%
mSSIM				
	Retrospective	0.9743	0.9767	0.9780
	Prospective	0.9476	0.9464	0.9525

**TABLE 2.2:** Normalized Root Mean Squared Error (NRMSE) and mean Structural Similarity Index Measure (mSSIM) values for the prospective experiment using both retrospective and prospective undersampling. Values are shown for the following methods: Structural undersampling (Structural), the data-driven variable density Poisson disk method (VDPD), and the iterative design method (Iterative).

In both cases, the iterative design method performs best. However, when measured against the fully sampled scan, the errors for the prospective scans were much higher, which can be attributed to registration errors and possibly physiological differences between the prospective scans and the fully sampled scan.

Figure 2.5 shows the undersampling patterns and reconstructed images for the prospective experiment. In the error maps for the retrospective results (Fig. 2.5, G, I, and K) the number of large errors and the overall magnitude of the errors decreased with decreasing NRMSE (Table 2.2). In the error maps for the prospective results (Fig. 2.5, M, O, and Q)

large errors occurred in the areas around the skull for all scans, which are probably related to imperfect registration and the influence of partial volume effects related to resampling in the registration process. The prospective errors in the brain matter were slightly higher than the retrospective errors at the same location, but the structure of the errors appears to be similar. For the structural undersampling pattern, the errors in the brain matter were more noise-like than the other undersampling patterns (Fig. 2.5, G and M).

When looking more closely at specific details of the reconstructed images, it is difficult to confirm the quantitative results regarding reconstruction quality. As indicated by the arrows in Figures 2.3O to S and 2.4O to S and Figure 2.5R to X, loss of contrast and loss of small details were observed that varied between the undersampling methods. Whereas for the brain dataset the iterative design method seemed to yield the highest resolution on average (Fig. 2.4S), this was less obvious, if at all true, for the knee dataset and the prospective experiment, where the reconstruction quality varied more locally.

When comparing the actual undersampling patterns generated for the knee and brain datasets by the three data-driven methods, large variations between the undersampling patterns for both datasets were observed (Figs. 2.3 and 2.4, top row). Especially the apparent sampling densities varied substantially. For example, the iterative design method did not sample the highest frequencies at all, which effectively lowers resolution. Furthermore, the undersampling patterns resulting from the iterative design method (Figs. 2.3E and 2.4E) appeared less random than the other undersampling patterns; in many areas, chessboard patterns were present.

The undersampling patterns generated for the prospective experiment by the VDPD and iterative design methods (Fig. 2.5, C and D) appeared similar, although the apparent sampling density generated by the iterative design method is slightly higher (i.e. denser sampling towards the  $k$ -space center) and slightly asymmetric: the top and bottom of  $k$ -space were sampled less densely.

The computation times of the data-driven methods scale with the CS reconstruction time. On a single core of a Xeon E5-2670 processor, the CS reconstruction of a single image took about 5 minutes for the knee dataset and 10 minutes for the brain dataset. For the knee dataset, when training the data-driven methods with a single subject (experiment 2) this resulted in a training time of 1625 minutes for the data-driven VD undersampling method, 125 minutes for the power spectrum method, and 500 minutes for the iterative design method. For the brain dataset, these times were twice as high. For the prospective experiment, a single reconstruction took about 3 minutes on 20 cores of a dual Xeon E5-2670 processor. This resulted in a training time of 300 minutes for both the data-driven VDPD undersampling method and the iterative design method.

## 2.4 Discussion

In this study, we have investigated the influence of different undersampling patterns on Compressed Sensing MRI reconstruction quality. We retrospectively simulated over 65,000 CS acquisitions and reconstructions of 3D scans from two large datasets using different undersampling patterns. In addition, we applied two of the three undersampling methods prospectively to show that the principles demonstrated in this study can be applied in practice.

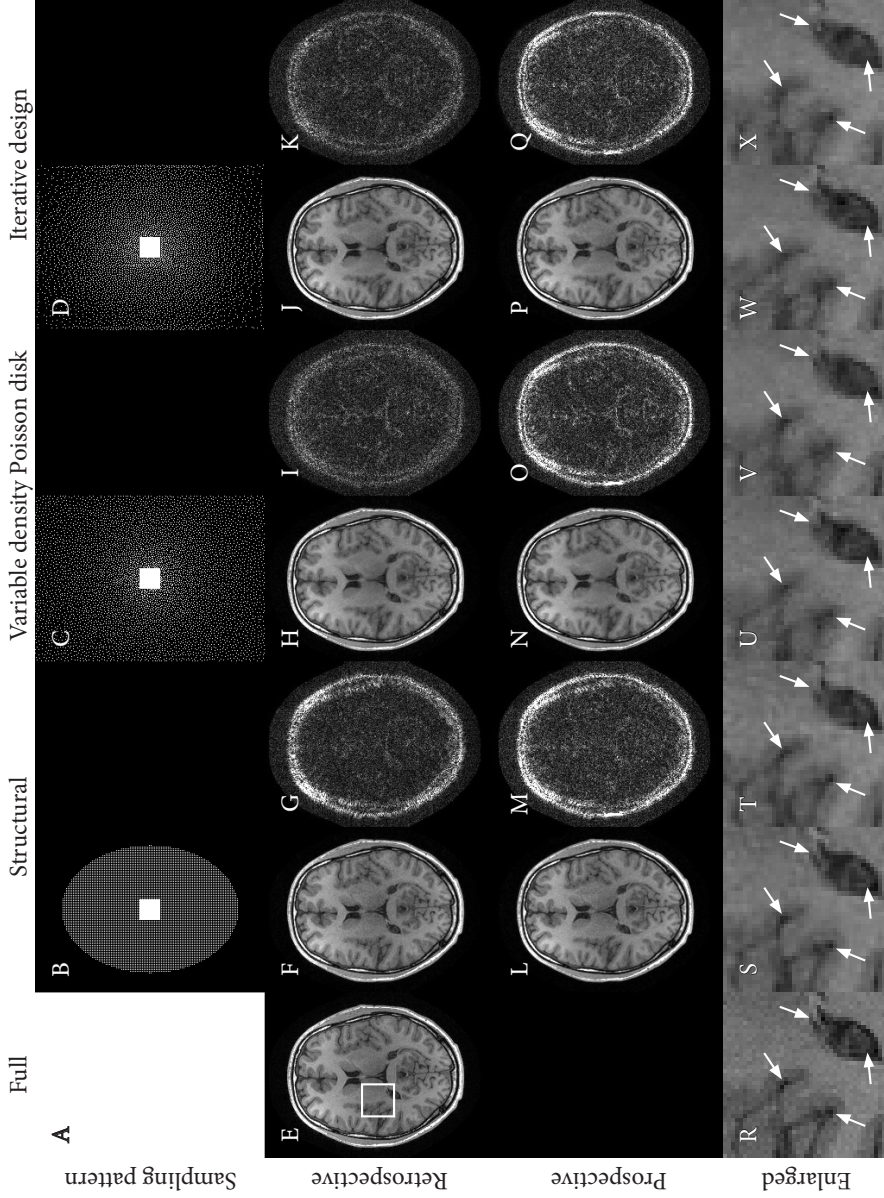


**FIGURE 2.5:** Reconstruction results for the prospective experiment. Fully sampled image (E) with enlarged region (R) indicated. Undersampling pattern (first row), retrospective reconstructions (F, H, J) and absolute reconstruction errors (G, I, K) times 5 (second row), prospective reconstructions (L, N, P) and absolute reconstruction errors (M, O, Q) times 5 (third row), and enlarged region (fourth row, retrospective [S, U, W] and prospective [T, V, X]) for: Structural undersampling (B, F, G, L, M, S, T), the data-driven VDFPD method (C, H, I, N, O, U, V), and the iterative design method (D, J, K, P, Q, W, X).

For variable density random undersampling, we found that the optimal sampling densities were different for the knee and the brain dataset. The analysis of VD and VDPD undersampling patterns showed that choosing a sampling density other than the optimal density decreases reconstruction quality, especially when the chosen sampling density is too low (i.e. the sampling is too uniform) for CS reconstruction without parallel imaging. In contrast, for the VDPD patterns, choosing the sampling density too high resulted in the highest errors, whereas a uniform density ( $d = 0$ ) performed similar to structural undersampling. For comparison, note that the structural undersampling used for SENSE or GRAPPA also has a uniform density. These results clearly indicate that optimization of the undersampling pattern is necessary to avoid suboptimal CS reconstructions when using VD or VDPD undersampling. Our data-driven VD and VDPD experiments (Tables 2.1 and 2.2) resulted in reconstruction errors very close to the lowest reconstruction errors found in the analysis of random VD and VDPD undersampling (Fig. 2.2), showing that suboptimal results for VD and VDPD undersampling can be avoided with a data-driven approach.

The power spectrum method yielded results similar to the data-driven VD method. This suggests that the PDF calculated from the power spectra was functionally equivalent to the optimal VD sampling density, even though the resulting sampling patterns were very different. An advantage of the power spectrum method is that the power spectra can be easily calculated, while finding the optimal VD sampling density requires optimization. Currently, no method is available that combines the power spectrum method with structural undersampling, and therefore it was not tested in the prospective experiment. The positive results in our non-parallel-imaging experiments indicate that a combination of the power spectrum method with VDPD sampling could be useful to efficiently find a good VDPD sampling density.

The iterative design method yielded lower reconstruction errors than both the data-driven VD method and the power spectrum method on the knee and brain datasets. In the prospective experiment, the iterative design method yielded lower reconstruction errors than the data-driven VDPD method did. This shows that the iterative design method is able to adapt to specific datasets, rather than only matching the *k*-space energy distribution. Interestingly, for the knee and brain datasets, the resulting undersampling patterns did not always sample the highest frequencies and showed checkerboard patterns, a sign of structural undersampling, rather than random undersampling (Fig. 2.3E and 2.4E). The tendency toward sampling lower frequencies may indicate that the undersampling factor was too high to maintain the full resolution of the scans. In this situation, the iterative design method tends to select lower frequencies in *k*-space because they apparently reduce the reconstruction error more than the high frequencies do. By comparison, methods that are based on random sampling always have a chance to sample the higher frequencies, unless they are manually instructed not to do so. The signs of structural (i.e. coherent) undersampling show that random (i.e. incoherent) undersampling is not strictly required to obtain good CS reconstructions. This seems to contradict the notion that incoherent sampling is required for CS [10] and warrants further investigation.

In the prospective experiment, the iterative design method successfully generated an undersampling pattern that included structural undersampling. Although this was promoted by the modification for parallel imaging that we made to the method, it was not a strict requirement, as opposed to the minimum distance required between sampling locations in VDPD sampling for example. This shows that the method can automatically adapt to situations that require structural undersampling, without specific knowledge of the re-

construction method or the coil geometry. Especially for asymmetric coil geometries, this may prove useful.

An interesting aspect of the iterative design method is the fact that by designing an undersampling pattern with a predefined undersampling factor, it actually generates optimized undersampling patterns for a range of undersampling factors up to that predefined undersampling factor. This may be of particular interest in methods where it is desirable that the undersampling factor can be chosen after the scan, for example, because of physiological circumstances [57] or the inability to adequately perform a breathhold [58]. When using the iterative design method, one can retrospectively choose any undersampling pattern up to the predefined factor, knowing that it will be an optimized undersampling pattern.

When using only one subject for training the data-driven methods, a small reduction in reconstruction quality was observed in the worst cases, however on average there were only small differences between using all but one subject and using just one subject for training the data-driven methods. In other words, while using multiple subjects for training is preferred, using a single subject for training is still sufficient to avoid suboptimal reconstruction quality. This is important for clinical adoption of data-driven undersampling methods for CS MRI, as the acquisition of one fully sampled dataset of a representative subject may be expected to be acceptable, whereas acquisition of many fully sampled datasets is impractical. The acquisition of a fully sampled dataset is relatively easy for anatomies that do not move much or can be stabilized, as demonstrated in our prospective experiment. The acquisition of a fully sampled dataset may prove more difficult, or even impossible, for moving anatomies or dynamic scan sequences, for example. In these cases it should be investigated whether different scans or undersampled scans can still provide valuable information for the purpose of optimizing undersampling patterns.

Although the differences in the quantitative results on the knee and brain datasets were generally statistically significant, it is important to note that this does not necessarily correspond to clinically significant differences. The qualitative results showed that the reconstruction quality varied locally per method and that the quality was not always consistent between the two used datasets. In contrast, our quantitative results were indicative only for the overall reconstruction quality. For specific applications of CS, it will be necessary to review reconstruction quality with respect to clinical objectives, such as being able to detect pathology.

We found no meaningful positive correlation between the incoherence defined by Lustig et al [10] and NRMSE reconstruction errors for VD and VDPD undersampling. Some positive correlations were found within single sampling densities, but only when the sampling density was higher than the optimal density. From these results, it follows that minimization of sampling coherence in undersampling patterns is unlikely to lead to reduced reconstruction errors when the sampling density is chosen properly. This confirms the assumption by Seeger et al that the analysis of a PSF will not be useful to optimize k-space undersampling, which they attribute to the signal dependence of non-linear sparse reconstruction [43]. With this signal dependence in mind, we believe that it is unlikely that a single metric can be defined that efficiently judges the quality of an undersampling pattern, apart from actually measuring reconstruction errors resulting from using the undersampling pattern in CS reconstructions.

In the prospective experiment we demonstrated that the methodology applied to knee and brain datasets also extended to a practical setting including parallel imaging CS reconstruction. Similar to VD random undersampling, it was necessary to find the optimal

sampling density for VDPD sampling to avoid suboptimal reconstructions, and with a minor modification, the iterative design method was able to generate an undersampling pattern that resulted in lower reconstruction errors. However, the prospective experiment was too small to be considered conclusive evidence. As such, undersampling for parallel imaging CS reconstruction should be investigated in more detail and on more data in future research.

The quality of the prospectively undersampled scans seemed to be comparable with their retrospective counterparts, based on qualitative, visual assessment. However, the errors calculated on the prospective scans were influenced not only by the undersampling pattern but also by residual differences between scans after rigid registration caused by partial volume effects due to resampling, physiological factors, and/or hardware-related factors. These confounding factors made it hard to quantitatively compare error metrics of retrospectively and prospectively undersampled scans. This leads us to the conclusion that the results obtained by retrospective undersampling are more representative for the changes caused purely by the undersampling patterns (and possibly other CS aspects). At the same time, it remains important to ensure that retrospective experiments are representative for prospectively undersampled scans and that the methods are practically applicable.

When putting the presented results in perspective, it is important to remember that data-driven optimization of an undersampling pattern for CS is just one aspect of the CS implementation. Data-driven approaches should be taken to optimize other aspects of the CS implementation, such as the sparse domain and the reconstruction algorithm.

In conclusion, we have shown that data-driven undersampling methods are required to avoid suboptimal reconstruction quality in Compressed Sensing MRI. In general, we recommend acquiring at least one fully sampled scan in order to be able to optimize a CS undersampling pattern specific for that scan protocol and anatomy. In a non-parallel-imaging CS application, we recommend using either the power spectrum method or the iterative design method. The power spectrum method is easy to implement and fast, while yielding reconstruction quality comparable with what could be achieved with variable density undersampling. For parallel imaging CS reconstruction and when aiming to achieve the highest reconstruction quality irrespective of computational time limitations, we recommend the iterative design method as it led to the highest reconstruction quality in all analyzed cases.





**FAST FOURIER-BASED SIMULATION OF  
OFF-RESONANCE ARTIFACTS IN STEADY-STATE  
GRADIENT ECHO MRI APPLIED TO METAL  
OBJECT LOCALIZATION**

**Based on:**

F. Zijlstra, J. G. Bouwman, I. Braškute, M. A. Viergever, and P. R. Seevinck, “Fast Fourier-based simulation of off-resonance artifacts in steady-state gradient echo MRI applied to metal object localization,” *Magnetic Resonance in Medicine*, Dec. 2016, early view online.

**Abstract**

In this study, we propose a method to accelerate simulation of off-resonance artifacts in steady-state gradient echo MRI by using Fast Fourier Transforms, and demonstrate its applicability to metal object localization.

By exploiting the repetitive nature of steady-state pulse sequences it is possible to use fast Fourier transforms to calculate the MR signal. Based on this principle, a method for fast simulation of off-resonance artifacts was designed. The method was validated against Bloch simulations and MRI scans. Its clinical relevance was demonstrated by employing it for template matching-based metal object localization, as applied to a titanium cylinder, an oxidized zirconium knee implant, and gold fiducials.

The fast simulations were accurate as compared with actual MRI scans of the objects. The differences between the fast simulations and Bloch simulations were minor, while the acceleration scaled linearly with the number of phase-encoding lines. The object localization method accurately localized the various metal objects.

The proposed simulation methodology provided accurate 3D simulations of off-resonance artifacts with a lower computational complexity than Bloch simulations. The speed of the simulations opens up possibilities in image reconstructions involving off-resonance phenomena that were previously infeasible due to computational limitations, as demonstrated for metal object localization.

### 3.1 Introduction

Simulation of MRI has proven successful in characterizing off-resonance artifacts caused by disturbances of the main magnetic field  $B_0$  [59–61]. These artifacts include geometric distortion, signal loss, signal pile-up, and phase dispersion [62]. In clinical practice, off-resonance artifacts are increasingly caused by the presence of metal objects, such as implants, surgical screws, or interventional devices [63]. The ability to predict artifacts around metal is an important investigative tool for the development of methods aiming at either imaging around metal objects [25, 26, 64] or localization of metal objects [28, 65, 66].

The most general method for simulating off-resonance artifacts is Bloch simulation, which uses the discrete time solutions of the Bloch equations to simulate the entire pulse sequence for a lattice of isochromats [67, 68]. However, the generality of Bloch simulation comes at the cost of a high computational burden, which increases linearly with the product of the number of simulated isochromats and the number of simulated k-space coefficients. In simulating a 3D scan, both the number of isochromats and the number of k-space coefficients increase cubically with increasing scan resolution and/or field of view. Both parallel computation [69] and GPU acceleration [70] have been used to accelerate Bloch simulation. However, these types of acceleration only reduce the simulation time by a constant factor, which means that simulating large 3D scans remains impractical.

In this study, we propose a fast alternative to Bloch simulation for simulating off-resonance artifacts in steady-state pulse sequences. By assuming the signal is in a steady state, it is possible to simulate the MRI signal with a computational complexity that is lower than that of Bloch simulation, while maintaining some of its generality and without requiring analytical descriptions of the phenomena involved. We validated the speed and accuracy of the fast simulation method by comparing it with Bloch simulations and gradient echo scans of a titanium cylinder in vitro. Furthermore, to demonstrate the clinical relevance of the fast simulation method, we employed it for a metal object localization method, inspired by the work of Wachowicz et al. [28], and tested this method on scans of a titanium cylinder, an oxidized zirconium knee implant, and gold fiducials.

### 3.2 Theory

Bloch simulation can accurately simulate a large number of phenomena in MR simultaneously, such as radiofrequency (RF) pulse inhomogeneity, nonlinear encoding gradients, off-resonance effects, and chemical shift [68]. Depending on the specific research question, not all of these effects need to be simulated, which can simplify the simulation.

In idealized conditions, MRI encoding establishes a perfect Fourier relationship between the measured signal and the image of the object. For example, in a 2D gradient echo sequence with perfectly rectangular encoding gradients, the demodulated MR signal during the readout interval is given by the following formula:

$$s(k_x, k_y) = \int \int \int \rho(x, y, z, t) e^{-i2\pi(k_x x + k_y y)} dx dy dz \quad (3.1)$$

Here,  $\rho$  is the effective spin density at time point  $t$ , which, for example, can include the effects of RF excitation, proton density,  $T_1$  and  $T_2^*$  decay, and off-resonance ( $\Delta B_0$ ). In a perfect steady state with no motion or other time-varying factors, the effective spin density without encoding is identical in every repetition of the pulse sequence. Then, for simulation

of a discrete isochromat grid with proton density ( $\rho'$ ),  $\Delta B_0$ , and  $T_2$  as parameters, the signal formula (Eq. (1)) can be rewritten to the following:

$$s(k_x, k_y) = \sum_z \sum_y \sum_x \rho'(x, y, z, t') e^{i2\pi\gamma\Delta B_0(x,y,z)t'} e^{-t'/T_2(x,y,z)} e^{-i2\pi(k_x x + k_y y)} \quad (3.2)$$

Here, the time point  $t'$  is the time after RF excitation. Because  $k_x$  is a function of  $t'$  (i.e. the readout direction in k-space is traversed over time during one repetition) and  $k_y$  is independent of  $t'$ , this formula can be split into a form where the phase encoding can be evaluated separately as a 1D fast Fourier transform (FFT) for every  $k_x$  and every  $z$ :

$$s'(k_x, y, z) = \sum_x \rho'(x, y, z, t') e^{i2\pi\gamma\Delta B_0(x,y,z)t'} e^{-t'/T_2(x,y,z)} e^{-i2\pi k_x x} \quad (3.3)$$

$$s(k_x, k_y) = \sum_z \sum_y s'(k_x, y, z) e^{-i2\pi k_y y} \quad (3.4)$$

The complexity of this alternative computation of the signal formula is:

$$\mathcal{O}(N_z N_y N_{k_x} N_x + N_z N_{k_x} (N_y \log N_y)) \quad (3.5)$$

Here, the size of the isochromat grid is  $N_x \times N_y \times N_z$ , and the size of the simulated k-space is  $N_{k_y} \times N_{k_x}$ . For Bloch simulation, the complexity is equivalent to naïve summation:

$$\mathcal{O}(N_z N_x N_y N_{k_x} N_{k_y}) \quad (3.6)$$

Theoretically, this corresponds to a speedup in the order of  $N_{k_y}$ . In 3D simulation, phase encoding in both  $y$  and  $z$  directions can be calculated with FFTs, resulting in a theoretical speedup in the order of  $N_{k_y} \cdot N_{k_z}$ .

## 3.3 Methods

### 3.3.1 Fast Simulation

We implemented the FFT-based fast simulation as described in the Theory section, referred to as FORECAST (Fourier-based off-resonance artifact simulation in the steady state) [71]. We published the MATLAB (MathWorks, Natick, Massachusetts, USA) source code for FORECAST on the MATLAB File Exchange<sup>1</sup>.

To validate the fast simulation methodology, we created a phantom of a titanium cylinder (length, 86 mm; diameter, 24 mm; magnetic susceptibility,  $\chi = 181$  ppm) placed in agar gel. The phantom was scanned with a fast 3D spoiled gradient echo scan with non-slice-selective excitation using the following parameters: matrix =  $256 \times 256 \times 96$ ; isotropic resolution = 1 mm; echo time/pulse repetition time (TE/TR) = 3.2/6.9 ms; flip angle =  $30^\circ$ ; feet-head readout direction; readout bandwidth =  $\sim 57$  kHz; excitation bandwidth =  $\sim 6.8$  kHz; scan time = 2 min, 13 s) at a field strength of 1.5T (Philips Achieva, Best, The Netherlands). To test the accuracy of the simulated artifacts under varying conditions, we rotated the phantom in the coronal plane with angles of approximately  $0^\circ$ ,  $45^\circ$ , and  $90^\circ$  relative to  $B_0$ . Furthermore, we varied scan parameters that directly influence artifact size and shape: 1) the echo time

<sup>1</sup><http://www.mathworks.com/matlabcentral/fileexchange/56680-mri-simulation-using-forecast--fourier-based-off-resonance-artifact-simulation-in-the-steady-state>

was doubled to 6.4 ms (TR = 11.2 ms); 2) the readout bandwidth was doubled to  $\sim 114$  kHz (TE/TR = 2.1/4.7 ms); and 3) the readout direction was changed to the left-right axis.

Fast simulations were performed for each of these situations to allow a qualitative comparison of the simulated artifacts and the experimentally obtained artifacts. The parameters of the isochromat grid were chosen as follows: The  $\Delta B_0$  map was calculated from the known magnetic susceptibility of the titanium cylinder using a fast method for forward field-shift calculation [22]. The proton density was defined to be 1 in the medium surrounding the cylinder, and 0 in the cylinder itself. If at any location the  $\Delta B_0$  value was outside the RF excitation bandwidth, the effective spin density was set to 0 (i.e. no signal originates from those isochromats). The  $T_2$  value of the medium was set to 50 ms. The resolution of the isochromat grid was 0.5 mm.

To measure the speed and accuracy of FORECAST relative to Bloch simulation, we simulated a 2D cross-section of the cylinder using both simulation methods. The scan matrix size was varied from  $16 \times 16$  to  $256 \times 256$ , and the simulation times per matrix size were recorded. The other scan parameters were identical to the 3D experiments. The isochromat grid had a resolution of 0.5 mm and was restricted to a single slice without simulating slice selection. In the Bloch simulation, we included 300 dummy repetitions of the pulse sequence to ensure a steady state at the start of encoding. These repetitions were not included in the total simulation time. Furthermore, we simulated perfect spoiling of the transverse magnetization at the end of each repetition. These timing experiments were run on a single core of an Intel Xeon E5-1607 CPU.

### 3.3.2 Object Localization

To demonstrate the accuracy of the simulations in a practical application, we implemented a method for localization of known metal objects inspired by the work of Wachowicz et al. [28]. FORECAST was used to generate a library of 3D images of a known object in varying orientations. Each of these images was matched individually to an acquired MRI scan using the phase correlation method [72]. The voxel with the highest correlation with any image from the library was chosen as the detected position of the object. The orientation of the object is then known from the orientation that was used to simulate the image with the highest correlation.

We applied this localization method to 3D spoiled gradient echo scans of the titanium cylinder, an oxidized zirconium knee implant (Oxinium, estimated  $\chi = 112$  ppm), and gold fiducials (length, 5 mm; diameter, 1 mm;  $\chi = -34$  ppm). As described in the previous section, the cylinder was scanned in three orientations:  $0^\circ$ ,  $45^\circ$ , and  $90^\circ$ . A phantom containing the knee implant was scanned with the phantom in seven different orientations: one scan approximately aligned with  $B_0$ , and one clockwise and counterclockwise rotation for each image plane. The scan parameters of the knee implant scans were almost identical to the parameters of the cylinder scans, but with matrix size  $128 \times 128 \times 128$  and readout bandwidth  $\sim 29$  kHz. One scan of a phantom with three gold fiducials was acquired on a 3T scanner (Philips Ingenia, Best, The Netherlands) using the following parameters: matrix =  $376 \times 292 \times 75$ ; isotropic resolution = 1.2 mm; TE/TR = 2.7/4.6 ms; flip angle =  $10^\circ$ ; anterior-posterior readout direction; readout bandwidth =  $\sim 25$  kHz; excitation bandwidth =  $\sim 7$  kHz; scan time = 2 min, 10 s. Each of the fiducials was aligned approximately with one of the main axes. With the same scan parameters we also acquired one in vivo scan of a prostate cancer patient, in whom three gold fiducials were placed in the prostate for position verification.

A segmentation of the prostate was used as the region of interest. Informed consent was obtained in accordance to the institutional review board of the University Medical Center Utrecht.

For both the cylinder and the gold fiducials a library of 321 different orientations of the objects was generated, corresponding to an angular resolution of approximately  $8^\circ$ . For the knee implant, a library of 891 orientations was generated in a range of  $-20^\circ$  to  $20^\circ$  rotation in each axis, corresponding to an angular resolution of approximately  $4^\circ$ . The isochromat grids of both the cylinder and knee implant were generated at a resolution of 0.5 mm. The isochromat grid for the gold fiducials was generated at a resolution of 0.075 mm in a 25.2 mm field of view around the fiducial.

## 3.4 Results

### 3.4.1 Fast Simulation

Figures 3.1 and 3.2 show the magnitude, phase, and phase difference of the MRI scans and the FORECAST simulations of the titanium cylinder rotated at angles of approximately  $0^\circ$ ,  $45^\circ$ , and  $90^\circ$  (Fig. 3.1), and with increased echo time, increased readout bandwidth, and with the readout direction changed from feet-head to left-right (Fig. 3.2). The 3D FORECAST simulations (matrix size =  $256 \times 256 \times 96$ ) took 1045 seconds on average on a single core of an Intel Xeon E5-1607 CPU.

In all of these experiments, the fast simulations of the cylinder appeared very similar to the actual scans. In areas of the scan where intravoxel dephasing occurs, the simulation slightly overestimated the signal voids, which may be attributed to the limited resolution of the isochromat grid, as well as possible imperfections in the size and susceptibility of the cylinder model. The phase difference between the simulations and the actual scans was generally consistent with the presence of merely a low-order background field, which could have been caused by the shape of the agarose phantom and/or system imperfections such as imperfect shimming. Only very close to the cylinder some local phase differences occurred, in particular in areas with signal pile-ups. Similar results can be seen for simulations of the knee implant in Figure 3.3.

Figure 3.4 shows the simulated images of both the 2D FORECAST simulation and the 2D Bloch simulation of the cylinder. Some minor differences between these images are visible at the boundary of the cylinder, where the full RF simulation in the Bloch simulation produced a more accurate spectrally selective excitation than the excitation bandwidth threshold used in the fast simulation. In Figure 3.5A, the simulation times for these images are shown for the FORECAST and Bloch simulations for increasing matrix size. Figure 3.5B shows the corresponding acceleration factors, which are nearly linear with matrix size, as predicted by the theoretical computational complexity.

### 3.4.2 Object Localization

For the scans with the titanium cylinder rotated approximately  $0^\circ$ ,  $45^\circ$ , and  $90^\circ$ , the best matching simulations were exactly those with the cylinder model rotated at  $0^\circ$ ,  $45^\circ$ , and  $90^\circ$ . These simulations are depicted in Figure 3.1 in the second and fourth columns. The actual positions of the cylinder are depicted by red outlines, which show that the signal voids do not accurately represent the location of the cylinder.

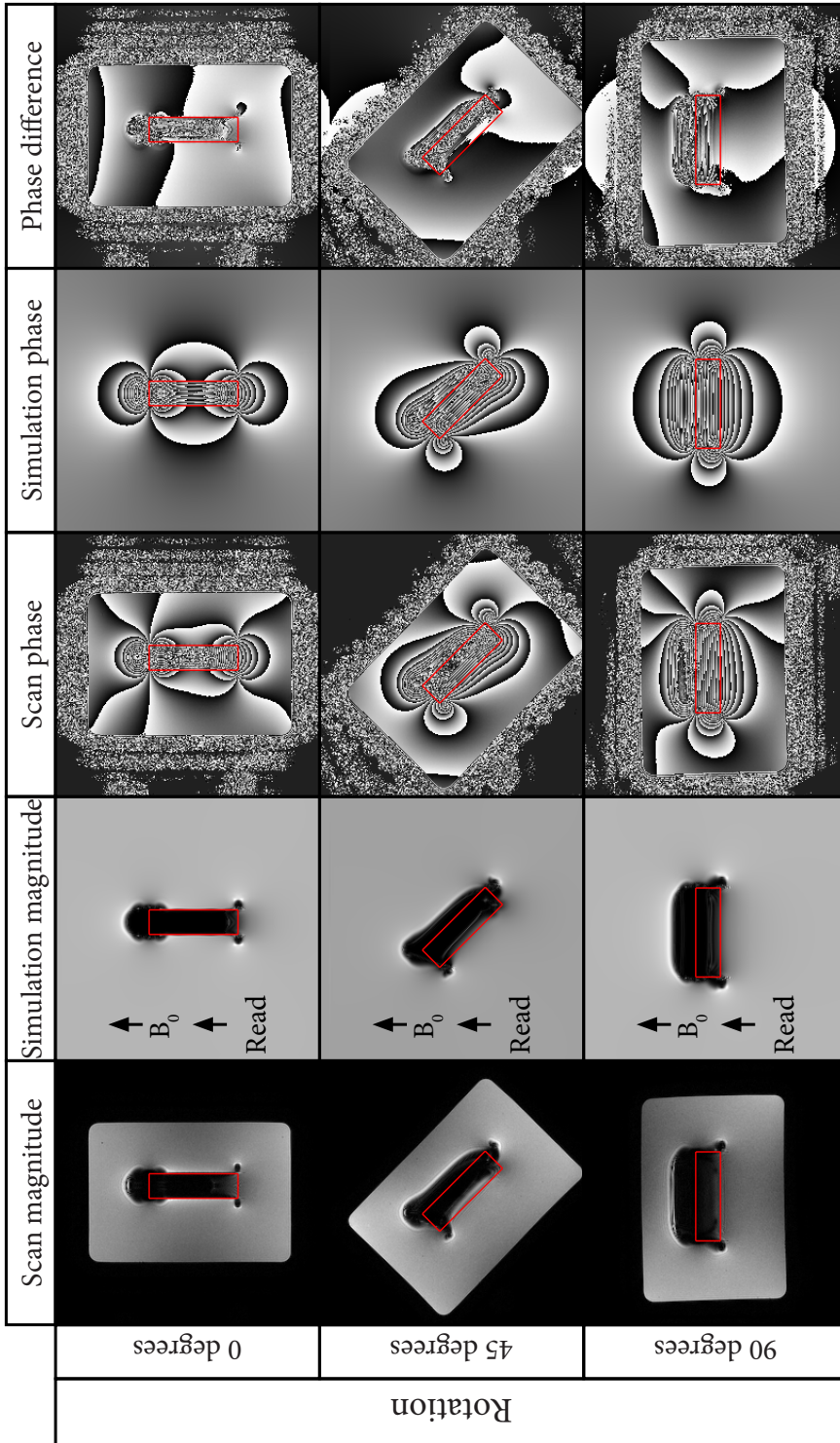


**FIGURE 3.1:** MRI scans (first and third columns) and FORECAST simulations (second and fourth columns) of a titanium cylinder rotated approximately 0°, 45°, and 90° in the coronal plane. The fifth column shows the difference in phase between the MRI scan and the simulations. The outline of the cylinder is shown in red.

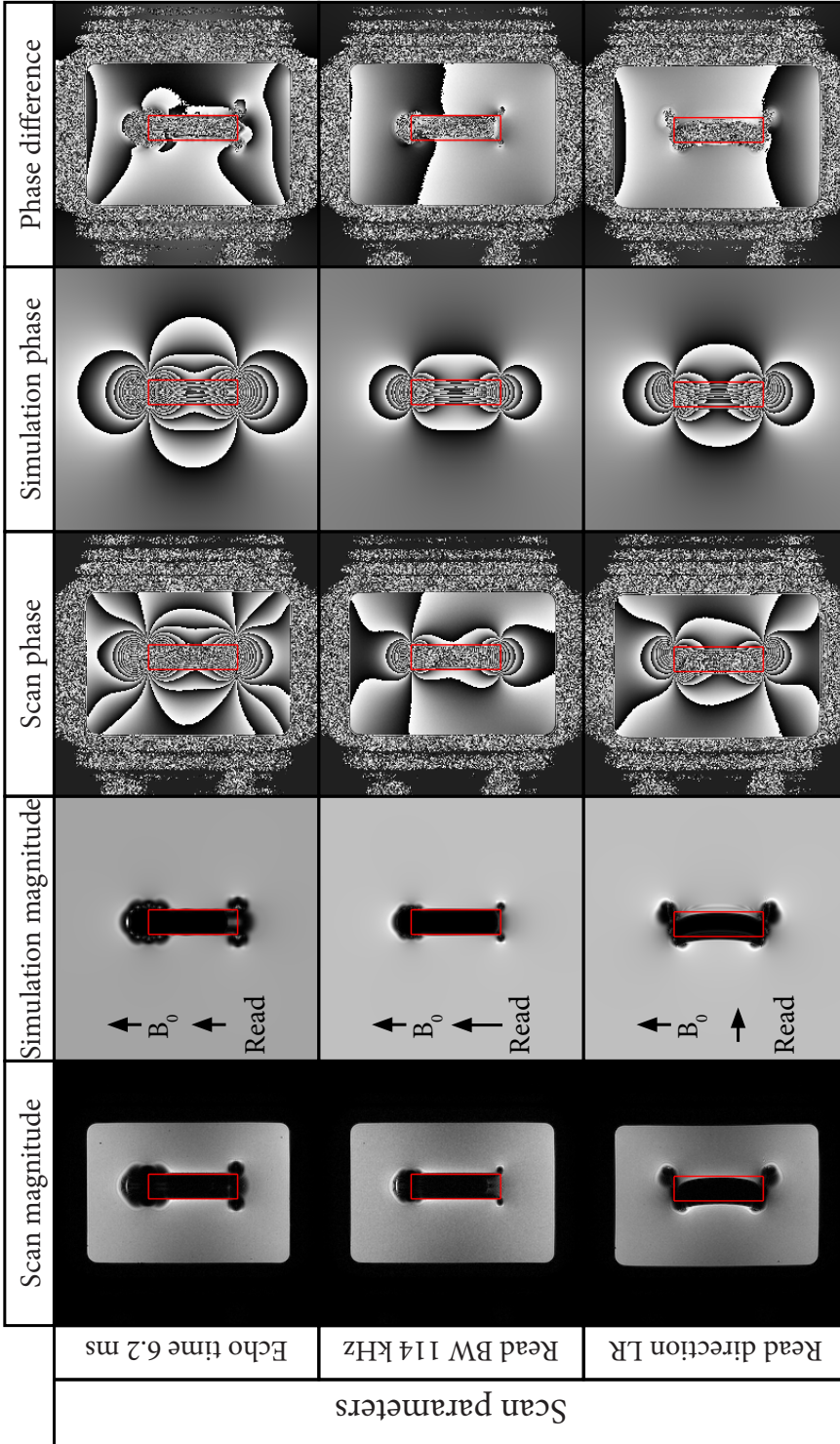


**FIGURE 3.2:** MRI scans (first and third columns) and FORECAST simulations (second and fourth columns) of a titanium cylinder with varying scan parameters (B). Echo time increased to 6.2 ms (first row), readout bandwidth increased to ~114 kHz (second row), and readout direction changed to left-right (LR) (third row). The fifth column shows the difference in phase between the MRI scan and the simulations. The outline of the cylinder is shown in red.

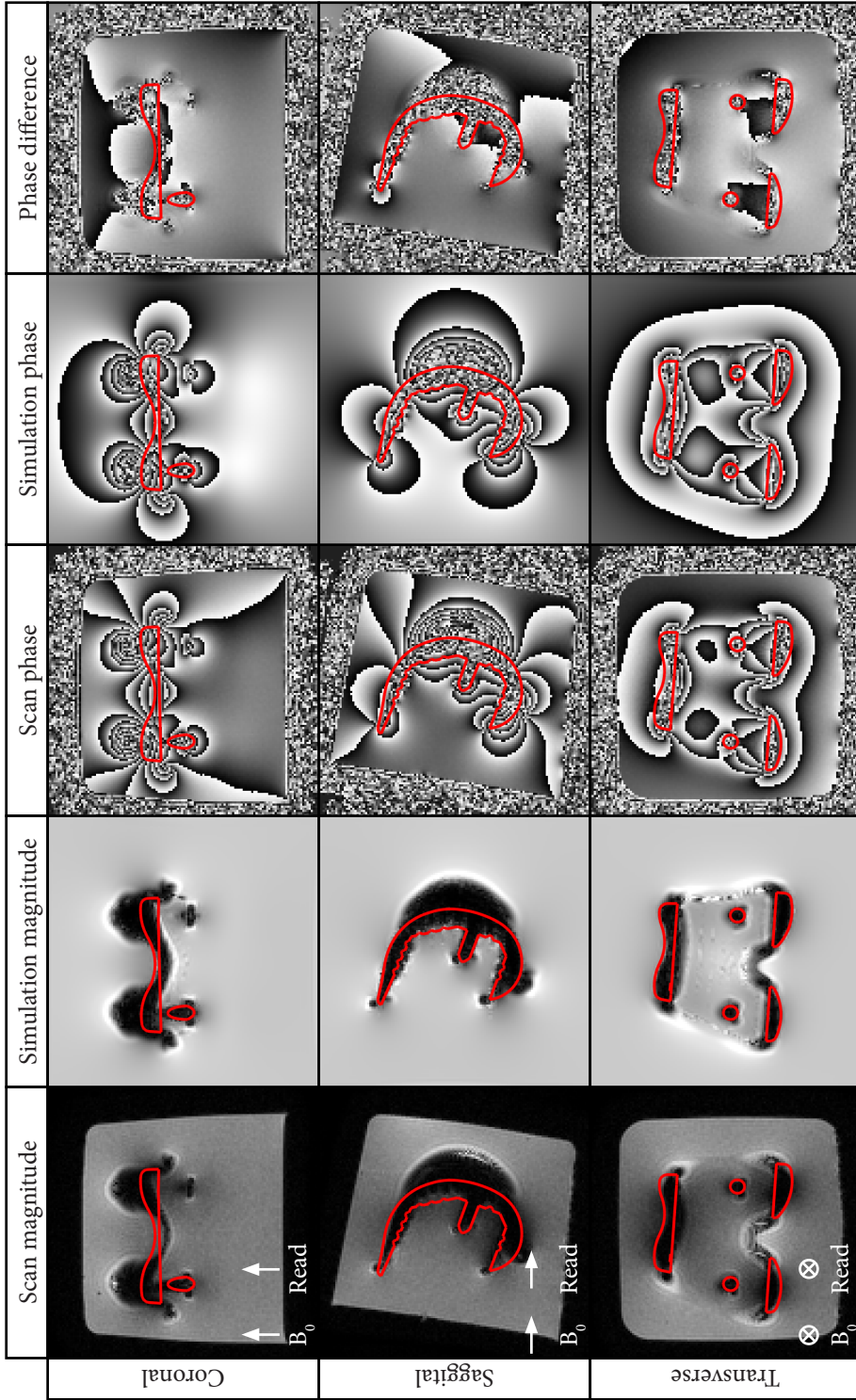


**FIGURE 3.3:** Coronal (first row), sagittal (second row), and transverse (third row) slices of an MRI scan (first and third columns) of an oxidized zirconium knee implant and the best matching simulation as found by the proposed localization method (second and fourth columns). The outline of the localized 3D model of the implant is shown in red.

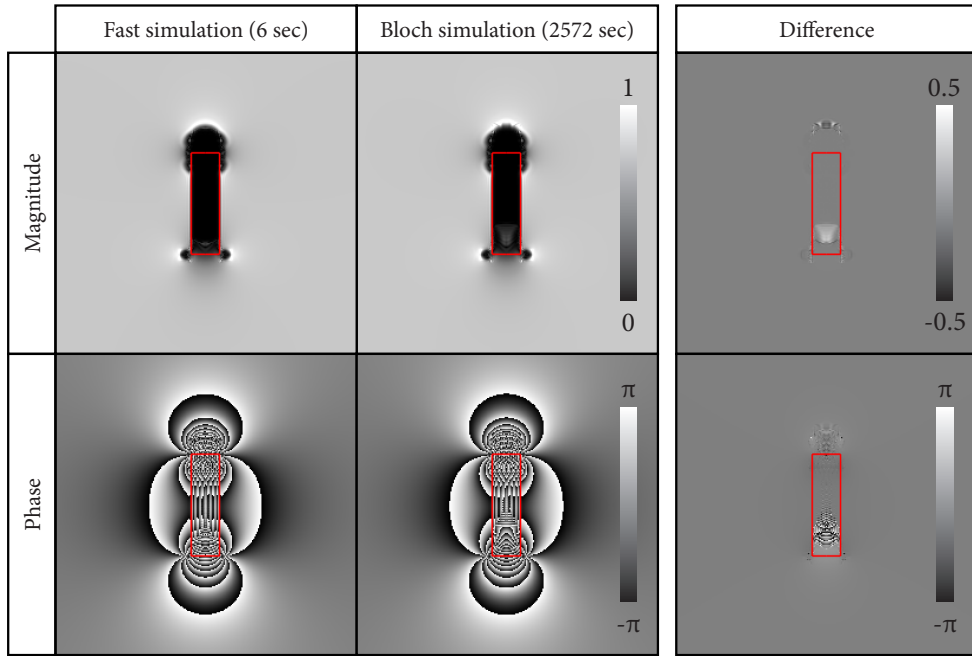


**FIGURE 3.4:** Magnitude and phase of a 2D simulation of a titanium cylinder using both FORECAST and Bloch simulations. The third column shows magnitude and phase difference maps. The outline of the cylinder is shown in red.

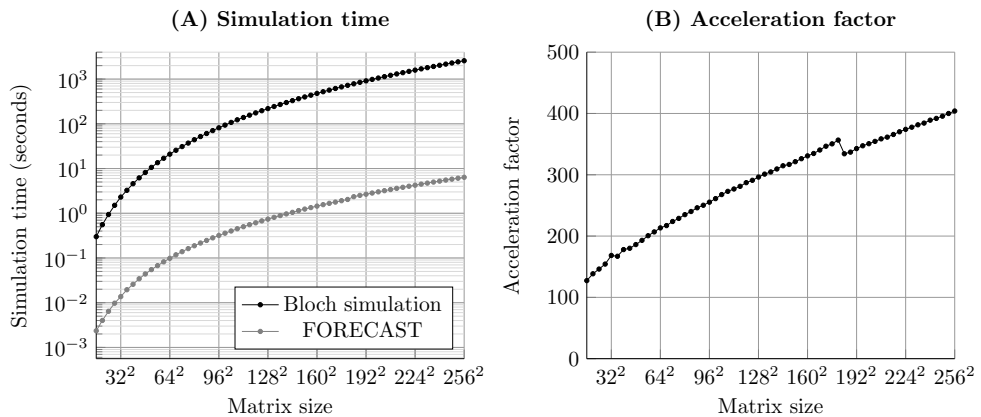


**FIGURE 3.5:** Simulation times for Bloch and FORECAST simulation for increasing 2D matrix sizes (A) and the corresponding acceleration factor (B).

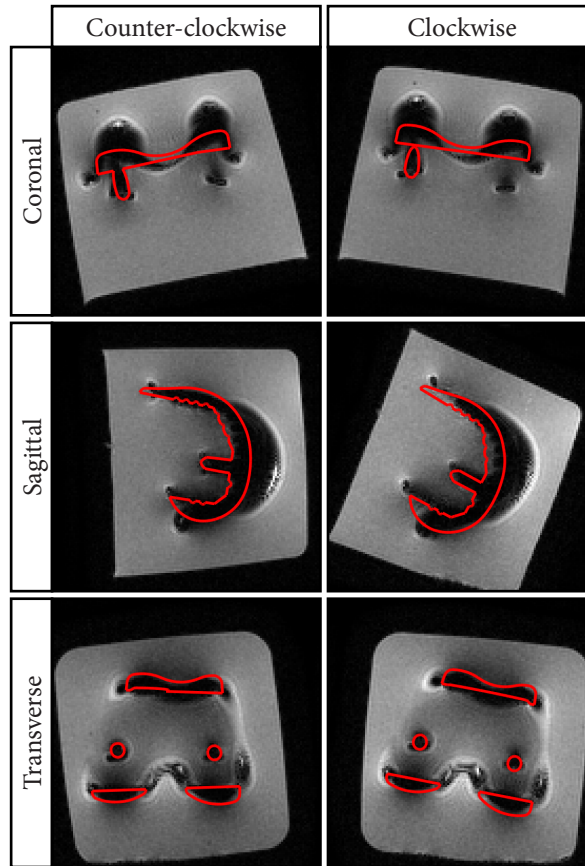


**FIGURE 3.6:** Localization of the femoral component of an oxidized zirconium knee implant in MRI scans where the implant was rotated counterclockwise and clockwise in the three orthogonal image planes. The outline of the 3D model of the localized implant is shown in red.

Figure 3.6 shows the localization results for the rotations of the knee implant phantom. The detected locations and orientations of the implant are shown as an overlay on these scans. The detected locations generally showed good correspondence with the MRI scan, with the exception of the clockwise rotation in the sagittal plane, where the localized implant appeared to be slightly rotated in the counterclockwise direction.

Figure 3.7 shows the gold fiducial detection results for both the phantom and in vivo experiments. In both cases the phase correlation maps showed high correlation at the locations of the fiducials. Both the locations and the orientations of the detected fiducials were accurate when qualitatively compared to the CT scan, as shown in the maximum intensity projection of the CT scan.

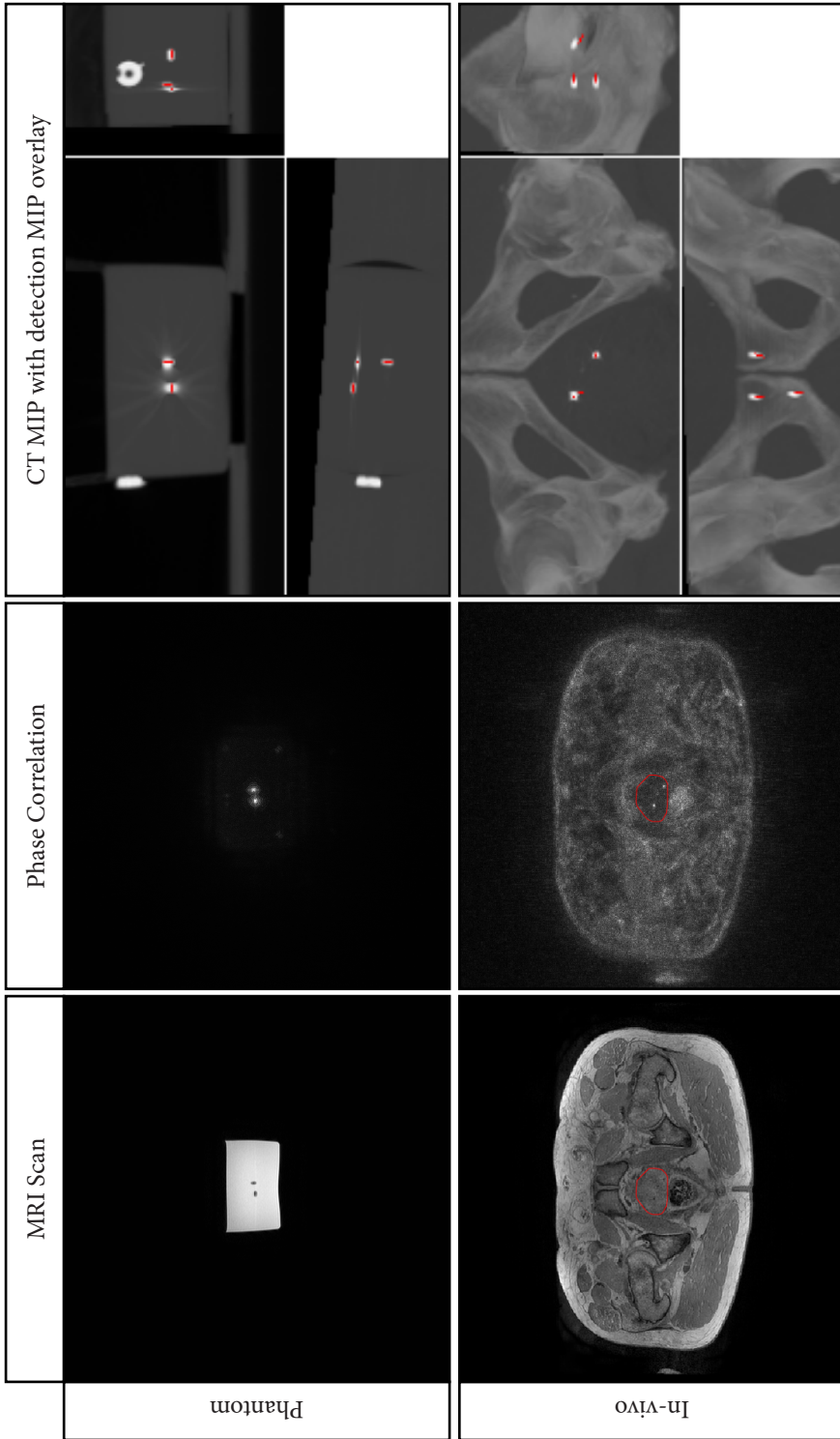


**FIGURE 3.7:** Gold fiducial detection in a phantom (top row) and in vivo (bottom row). From left to right: a transverse slice of the MRI scan showing two of the three fiducials (first column), the corresponding phase correlation map (second column), and a maximum intensity projection (MIP) of the CT scan in each image plane with an overlay of a MIP of the detected fiducials in red (third column). In the in vivo scan and phase correlation map an outline of the segmented prostate is shown in red.

## 3.5 Discussion

In this study, we have presented a theory for fast Fourier-based simulation of off-resonance artifacts in steady-state gradient echo MRI. Based on this theory, we implemented the FORECAST simulation method and applied it to the simulation of artifacts induced by metal objects in 3D gradient echo scans. The simulated artifacts were found to be accurate with respect to actual scans of metal objects of varying size and shape. To demonstrate the practical applicability of FORECAST, we applied it in a method for localization of known metal objects in MRI.

### 3.5.1 Fast Simulation

Our fast simulation methodology allowed the computation of high-resolution 3D simulations of off-resonance artifacts within several minutes on regular computer hardware. FORECAST has a computational complexity that is lower than the complexity of Bloch simulation by a factor of the number of phase-encoding lines. This lower complexity makes our approach especially useful for simulations of scans with large matrix sizes, such as high-resolution or 3D scans. In our experiments, we were able to perform 3D FORECAST simulations in 1045 s on a single CPU core, which was faster than a 2D Bloch simulation with the same in-plane matrix size, which required 2572 seconds. Because computing discrete Fourier transforms and FFTs is the primary computational load of the FORECAST method, the method can be easily accelerated using parallel computing or GPU acceleration.

In general, the off-resonance artifacts simulated by FORECAST were similar to the artifacts observed in actual MRI scans, in both the magnitude and the phase of the images. Differences between the simulations and scans can be partly attributed to factors that were not included in the simulation, such as accurate simulation of RF excitation and spoiling mechanisms. These effects can be included in the fast simulation with a hybrid simulation approach, in which Bloch simulation is used to numerically establish the steady state of a sequence, which can subsequently be used as an input to the FORECAST simulation. Additionally, there may have been small imperfections in the simulation models with respect to the real objects, since the size and susceptibility values were based on idealized models. The limited resolution of the models may have also caused imperfect intravoxel dephasing and partial volume effects. Given the favorable computational complexity of our method, the resolution of the simulation model can still be increased to reduce these imperfections while maintaining acceptable simulation times.

The results presented in this study only involved steady-state gradient echo pulse sequences. However, the simulation methodology is theoretically applicable to other types of steady-state pulse sequences as well. For example, including refocusing effects in the signal formula (Equation 3.3) would allow simulation of spin echo sequences. Simulation of sequences with non-Cartesian encoding could be achieved through the nonuniform FFT [73]. Although the gridding in the nonuniform FFT would increase simulation time, its computational complexity remains better than that of naïve summation. Another possibility is this simulation of sequences with turbo or EPI factors, although this would increase the simulation time proportionally to the turbo or EPI factor.

Although in this study we applied the fast simulation exclusively to the simulation of off-resonance artifacts for metal object localization, other research areas may benefit from the speed of the proposed simulation method. For example, FORECAST can be used to quickly

generate validation images to investigate the influence of susceptibility and off-resonance effects on reconstruction and postprocessing algorithms, such as  $B_0$  mapping or quantitative susceptibility mapping. Furthermore, the simulations could be used in methods that correct for off-resonance artifacts. For example, the phase difference images in Figures 3.1, 3.2, and 3.3 are essentially phase images in which the phase dispersion induced by the metal object is largely corrected. This may improve phase-sensitive reconstructions that have difficulties near strong field disturbers, such as Dixon water-fat separation [74], temperature mapping, or quantification of metal deposits [75]. The speed of the simulations also opens up possibilities for using simulations as part of iterative reconstruction approaches.

### 3.5.2 Object Localization

As a demonstration of the proposed fast simulation method, we implemented a method that localizes metal objects in MRI scans. The localization results on a cylinder, knee implant, and gold fiducials were mostly accurate to within the limits that could be expected from the angular resolution of the template library and the spatial resolution of the images. Generally, this shows that the simulations were sufficiently accurate for this type of application. Automatically locating known metal objects has a variety of potential applications. First, we have shown the possibility of locating gold fiducials. The same procedure can be applied to other types of metal markers and small metal objects such as brachytherapy seeds and sources [76, 77]. Second, locating large implants could be used to evaluate arthroplasty procedures and to improve diagnosis of pathology such as implant loosening. Third, the method could be used to locate interventional devices during interventional procedures, although modifications may be necessary to apply the procedure in real time. Finally, gaining exact knowledge about the position and orientation of any metal object could potentially be used to improve imaging and postprocessing in the vicinity of that object.

In conclusion, FORECAST is a fast alternative to Bloch simulation for 3D simulation of off-resonance artifacts in gradient echo MRI. The clinical applicability of FORECAST was shown in a metal object localization method, which was able to accurately localize a variety of objects. The low computational complexity of FORECAST makes it ideal as an investigative tool and opens up possibilities in image reconstruction involving off-resonance phenomena that were previously infeasible due to computational limitations.

## 3.6 Acknowledgements

We thank the Department of Orthopedics of the UMC Utrecht and Smith & Nephew for providing us with the knee implant and its computer model.





**CHALLENGES IN MR-ONLY SEED LOCALIZATION  
FOR POSTIMPLANT DOSIMETRY IN PERMANENT  
PROSTATE BRACHYTHERAPY**

**Based on:**

F. Zijlstra, M. A. Moerland, J. R. van der Voort van Zyp, J. L. Noteboom, M. A. Viergever, and P. R. Seevinck, "Challenges in MR-only seed localization for postimplant dosimetry in permanent prostate brachytherapy," *Medical Physics*, 2017, in press.

### Abstract

An MR-only postimplant dosimetry workflow for low dose rate (LDR) brachytherapy could reduce patient burden, improve accuracy, and improve cost efficiency. However, localization of brachytherapy seeds on MRI scans remains a major challenge for this type of workflow. In this study, we propose and validate an MR-only seed localization method, and identify remaining challenges.

The localization method was based on template matching of simulations of complex-valued imaging artifacts around metal brachytherapy seeds. The method was applied to MRI scans of 25 prostate cancer patients who underwent LDR brachytherapy and for whom postimplant dosimetry was performed after four weeks. The seed locations found with the MR-only method were validated against the seed locations found on CT. The circumstances in which detection errors were made were classified to gain an insight in the nature of the errors.

A total of 1490 out of 1557 (96%) seeds were correctly detected, while 67 false positive errors were made. The correctly detected seed locations had a high spatial accuracy with an average error of 0.8 mm compared with CT. A majority of the false positives occurred near other seeds. Most false negatives were found in either stranded configurations without spacers or near other seeds.

The low detection error rate and high localization accuracy obtained by the complex-valued template matching approach are promising for future clinical application of MR-only dosimetry. The most important remaining challenge is robustness with regard to configurations of multiple seeds in close vicinity, such as in strands of seeds without spacers. This issue could potentially be resolved by simulating specific configurations of multiple seeds, or by constraining the treatment planning to avoid these configurations, which could make the proposed method competitive with CT-based seed localization.

## 4.1 Introduction

Postimplant dosimetry is an important tool for quality assurance after low dose rate (LDR) prostate brachytherapy. Despite various innovations in planning and delivery of brachytherapy seeds [78–80], the actual dose distribution may deviate from the planned distribution due to errors in needle positioning, errors in seed delivery, prostate deformation between needle insertion and retraction, edema, and seed migration [78, 81, 82]. Therefore, postimplant dosimetry is recommended to assure the quality of the implant workflow and to establish accurate dose-response relationships [83].

In current practice for postimplant dosimetry, CT is the modality of choice for localizing brachytherapy seeds on account of its high sensitivity to the metal components in the brachytherapy seeds [78, 83]. However, delineation of the prostate and the organs at risk around the prostate is challenging because of the low contrast in soft tissues in CT images [84]. MR images, on the other hand, provide excellent soft tissue contrast and are often used for delineation of the prostate, tumor, and organs at risk [85, 86]. These delineations are then registered to CT images to perform high-quality dosimetry [87, 88], although uncertainties in delineation and image registration may impair accuracy of postimplant dosimetry. Furthermore, a disadvantage of the use of image registration is that errors may occur because of deformation of the prostate in between the CT and MRI scans, which may be caused by changes in patient position, or by physiological factors such as changes in bladder and rectum filling.

An MR-only approach to postimplant dosimetry could remove registration as a source of errors by providing intrinsically registered seed localization and organ delineations. Furthermore, patient burden and costs would be reduced by the omission of CT scanning in the workflow [89]. However, although MR-only approaches for localizing brachytherapy seeds have been investigated by several groups [28, 66, 90–94], no method has proven robust and accurate enough for clinical use as yet.

Some studies have only considered the susceptibility-induced signal voids caused by brachytherapy seeds in MRI [90–92]. A problem with this approach is that signal voids are not specific to brachytherapy seeds. Other sources of signal voids in the prostate include vessels, small bleeds, and calcifications.

Further studies have solved this issue by focusing on the off-resonance effects around brachytherapy seeds. Kuo et al. describe the use of the IRON (inversion recovery with on-resonant water suppression) pre-pulse for suppressing on-resonant signal, which creates positive contrast at the off-resonant signal around brachytherapy seeds [93]. A disadvantage of this method is that it is also sensitive to other sources of field inhomogeneity, which does not make it robust for in vivo application. The co-RASOR (center-out radial sampling with off-resonance reception) method was proposed to shift local signal pile-ups caused by off-resonance back to the center of the brachytherapy seed in radial acquisitions [94]. Dong et al. applied susceptibility gradient mapping to specifically use the local dephasing around brachytherapy seeds to generate positive contrast at the location of the seed [66]. Since these two approaches are based on local susceptibility effects, they are less sensitive to other field inhomogeneities.

A problem that remains with all of these methods is that generating positive contrast in itself is not enough for accurate localization of brachytherapy seeds. A robust detection algorithm would still be required to localize the seeds in varying orientations and in varying configurations.

Wachowicz et al. have proposed the use of simulations to characterize the artifacts around brachytherapy seeds and subsequently using these simulated images to establish the location and orientation of the seed in an experimentally obtained image [28]. For a large number of possible orientations of a seed they performed an MRI simulation, which were matched to the image using normalized cross correlation. Although the method was only demonstrated for a 2D spin echo sequence, the approach can theoretically be applied to any sequence, as long as accurate simulations for that sequence can be performed in reasonable time.

In this study, we have investigated the potential and challenges of an MR-only brachytherapy seed localization method using a comprehensive dataset of 25 prostate cancer patients who underwent LDR brachytherapy. We used a seed localization methodology that improves on the method proposed by Wachowicz et al. by incorporating complex-valued 3D MR simulations, provided by a recently proposed method for efficiently simulating off-resonance artifacts in steady-state gradient echo MRI sequences [95]. The resulting method is applicable to 3D images and exploits the off-resonance artifacts present in both the magnitude and the phase of the MR images to determine the location and orientation of multiple brachytherapy seeds. The localization results were verified against clinically used seed detections based on CT images, and all detection errors were examined to determine the circumstances in which the errors occurred. Based on the results we identify remaining challenges for applying MR-only postimplant dosimetry in clinical practice.

## 4.2 Methods

### 4.2.1 Patients

For this study, we recruited 25 prostate cancer patients who underwent LDR prostate brachytherapy between February 2015 and May 2016 and gave informed consent for an additional MRI scan optimized for MR-only seed detection. Informed consent was obtained in accordance to the guidelines of the institutional review board of the University Medical Center Utrecht. A total of 17 patients were treated using Best medical model 2301 (Best Medical Inc, Springfield, USA) I-125 seeds (Fig. 4.1A, top), with an average number of seeds implanted of  $62 \pm 7$  (mean  $\pm$  standard deviation (SD)). The remaining 8 patients were treated using Nucletron selectSeed model 130.002 (Elekta / Nucletron, Veenendaal, The Netherlands) I-125 seeds (Fig. 4.1A, bottom), with an average number of seeds implanted of  $64 \pm 16$  (mean  $\pm$  SD). Most seeds were implanted in stranded configurations, optionally spaced with 5 mm plastic spacers. If no spacers were used, we refer to those strands as unspaced strands. Best 2301 seeds in stranded configurations were always physically attached to the spacers or to other seeds. In contrast, the selectSeed seeds were never physically attached to either seeds or spacers.

Regular clinical postimplant dosimetry was performed around 4 weeks after implantation using a CT- and MRI-based approach. Semi-automatically detected seed locations were obtained from CT scans using the treatment planning system Oncentra Prostate (Elekta / Nucletron, Veenendaal, The Netherlands). This served as the gold standard in the validation of our proposed MR-only seed localization approach.

A 3D gradient echo scan was included in the regular MRI scanning protocol to facilitate the MR-only seed localization proposed in this study. Relevant scan parameters were: 1.2 mm isotropic acquired resolution, matrix size  $292 \times 376 \times 75$ , field of view  $350 \times 451 \times 90$

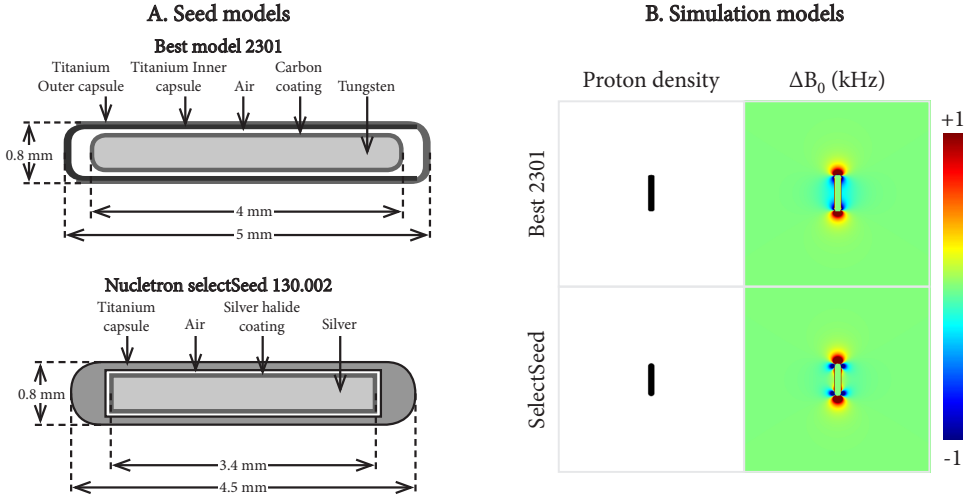


**FIGURE 4.1:** A. Schematics of the Best model 2301 (top) and Nucletron selectSeed 130.002 (bottom) brachytherapy seeds with material types indicated. B. Proton density and  $\Delta B_0$  maps that were used to simulate a seed oriented parallel with  $B_0$ . The maps were generated at a resolution of 0.075 mm and cover a field of view of  $25 \times 25 \times 25$  mm.

mm, TE/TR 2.7/4.6 ms, readout direction = anterior-posterior, readout bandwidth =  $\sim 1155$  Hz/pixel, flip angle  $10^\circ$ , and a scan time of 130 seconds. To prevent motion artifacts due to breathing from spilling into the prostate region, we chose the readout direction in the anterior-posterior direction, because the readout direction is less susceptible to motion artifacts. Scans were acquired at 3 tesla (Ingenia, Philips Healthcare, Best, The Netherlands) using a 32 channel torso coil. Figure 4.2 shows an example of this scan for a patient treated with Best 2301 seeds.

#### 4.2.2 Seed localization

We improved on the methodology proposed by Wachowicz et al. in a number of ways. First, we changed the simulation method to allow simulation of 3D gradient echo MRI scans, instead of only 2D spin echo scans. Second, we modified the template matching from using normalized cross-correlation to phase correlation [72], which appeared more robust with respect to background signal variations that are present in vivo. And finally, to aid in the detection of the large number of seeds present, we introduced additional steps to eliminate false positive detections.

#### 4.2.3 Library generation

To simulate complex-valued artifacts around brachytherapy seeds in high resolution for 3D gradient echo scans in reasonable time, we used the FORECAST (Fourier-based Off-Resonance Artifact simulation in the STeady-state) method [95]. The simulated artifacts include spatial distortion, dephasing, and signal dropout due to intra-voxel dephasing. The simulation models were generated at a resolution of 0.075 mm in a  $25 \times 25 \times 25$  mm region around

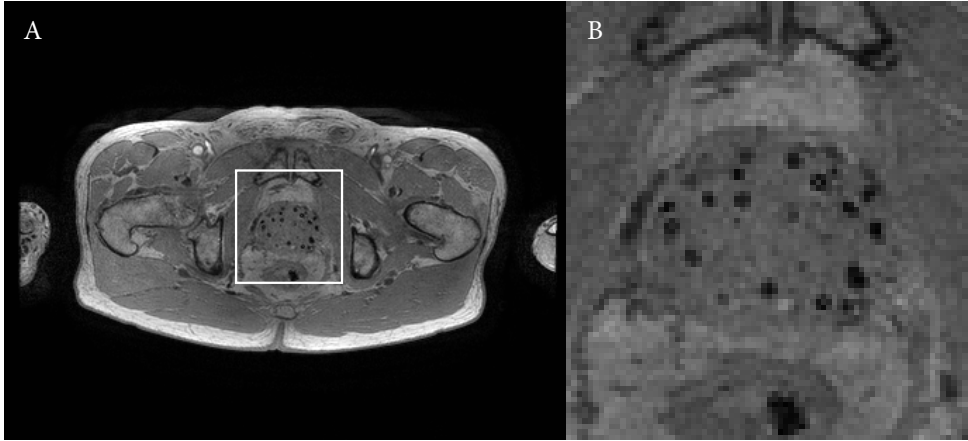


**FIGURE 4.2:** A magnitude image of a transverse slice of the 3D gradient echo scan that was used for seed localization (A), and an enlarged region around the prostate in which Best medical model 2301 brachytherapy seeds are present (B). The region is indicated by the white box in A.

a brachytherapy seed. The models contained the brachytherapy seed in a uniform medium with proton density set to 1 and a  $T_2$  value of 50 ms. Based on magnetic susceptibility models of the brachytherapy seeds (Fig. 4.1A), we calculated  $\Delta B_0$  maps for both seed models using a fast method for field-shift calculation [22] (Fig. 4.1B). Figure 4.3A shows an example of the scanned and simulated complex-valued artifacts for each seed type. We simulated a library of 321 seed orientations for each of the two types of brachytherapy seeds. The seed orientations were sampled approximately uniformly as orientation vectors positioned on a half-sphere. Figure 4.3B shows how the complex-valued artifacts vary with seed orientation for a subset of the simulated libraries.

#### 4.2.4 Template matching

In initial experiments we found that the normalized cross-correlation used by Wachowicz et al. was not robust against signal variations that were present in vivo. For this reason we used the phase correlation method [72] to perform template matching of the libraries with an acquired MRI scan in the frequency domain. Phase correlation is mathematically defined as the following elementwise operation in the frequency domain:

$$C(\mathbf{k}) = \frac{I(\mathbf{k})\overline{T(\mathbf{k})}}{|I(\mathbf{k})\overline{T(\mathbf{k})| + \epsilon} \quad (4.1)$$

Here,  $I$  is the frequency domain of the MR image,  $\overline{T}$  is the complex conjugate of the frequency domain of the simulated template image,  $C$  is the frequency domain of the phase correlation image,  $\mathbf{k}$  is the location of the frequency domain element to which the operation is applied, and  $\epsilon$  is a constant that prevents division by zero, which was set to  $10^{-15}$ . The phase correlation in the spatial domain is then obtained by performing an inverse fast Fourier transform on  $C$ . This is repeated for each template in the library. For each voxel in the scan, the template with the highest correlation was determined and stored as a candidate

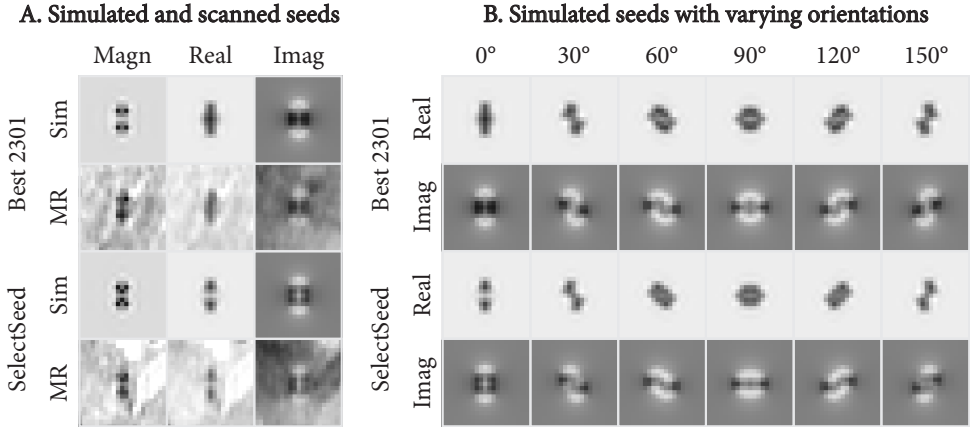


**FIGURE 4.3:** A. Coronal slice of MR simulations (Sim) and in vivo images (MR) for a seed oriented parallel with  $B_0$  for a Best 2301 (top) and a SelectSeed (bottom) seed. Both the magnitude (Magn) and the real and imaginary (Imag) components are shown. B. A subset of the simulated template libraries for varying orientations of the seeds. The images show the complex components (Real/Imag) of the simulations for rotations in the coronal plane with steps of  $30^\circ$ .

seed detection. We applied the template matching in a cubical region of interest incorporating the prostate with a margin of 5 mm between the delineated prostate and the bounding box.

#### 4.2.5 Seed detection

In order to reduce the number of false positive detections, we selected 1000 candidate detections with the highest correlations. On each of these candidates we performed a local linear regression of the measured signal around the candidate to the matched template to determine how well the template fit to the local signal. At the location of the candidate detection, the matched template was placed over the MR image to allow a voxelwise comparison of image and template intensities. All voxels in the template that deviated at least 20% from the background intensity (i.e. where artifacts were present) were used to solve the following linear regression problem:

$$aI(\mathbf{r}) + b = T(\mathbf{r}) \quad (4.2)$$

Here,  $I$  is the complex MR image intensity at location  $\mathbf{r}$ ,  $T$  is the complex template image intensity at location  $\mathbf{r}$ , and  $a$  and  $b$  are the complex-valued coefficients fitted using linear regression, which minimizes the sum of squared residual errors:

$$\sum_{\mathbf{r}} |aI(\mathbf{r}) + b - T(\mathbf{r})|^2 \quad (4.3)$$

We will refer to this sum as the residual error after linear regression, which indicates how well a template matched the local signal around a candidate seed detection. Next, candidates were accepted in the order of their residual error, starting with the candidates

with the lowest errors. For each accepted candidate, the dephasing caused by the presence of the seed was corrected by unwinding the phase in the image as predicted by the best matching template at that location (Fig. 4.4, last column). For every voxel in the template, the following phase correction was applied:

$$I_{new}(\mathbf{r}) = I(\mathbf{r})e^{-iArg(T(\mathbf{r}))} \quad (4.4)$$

Here,  $I_{new}$  is the complex MR image intensity after phase unwinding, and  $Arg(T(\mathbf{r}))$  is the complex argument (i.e. the phase) of the template at location  $\mathbf{r}$ .

After each phase correction the local regression was recalculated for each candidate affected by the correction. Furthermore, all candidates within 1 voxel distance of the accepted detection were removed to prevent multiple detections of a single seed. This detection process was repeated until the number of detected seeds was equal to the number of implanted seeds.

#### 4.2.6 Experimental setup

We applied our MR-only seed detection to each of the 25 subjects, using the specific library for the type of seed that was implanted. In order to compare the detected seed locations found on MRI to the detected seed locations on CT, we performed a rigid registration of the two point sets using the Coherent Point Drift method [96]. Next, an automatic matching was applied to find matching pairs of detections on MRI and CT. A seed detected on MRI which was within 3 mm of a seed detected on CT was accepted as a pair of matching seeds and removed from the list of seeds that needed to be matched. The matching was ordered such that the pairs with the smallest distances to each other were accepted as matches first.

Any seed that was detected on MRI and matched on CT was classified as a true positive (TP) detection. Seeds detected on MRI that were not matched on CT were classified as false positive (FP) detections. Finally, any seed that was detected on CT but not matched on MRI was classified as a false negative (FN) detection.

Based on these classifications we calculated the Dice similarity coefficient (DSC) [97] of the sets of detections on MRI and CT:

$$DSC = \frac{2TP}{2TP + FP + FN} \quad (4.5)$$

As a measure of the accuracy of the detected positions we calculated the mean and standard deviation of the distance to the matched CT detection for the true positive detections.

All FPs and FNs were reviewed to assess the conditions in which the detection errors were made. Figure 4.4 shows examples of most of these conditions and how they appear on CT and MR scans. The false positives were classified in one of the following categories:

- Incorrect automatic matching (Fig. 4.4B): In some cases the distance between a correct detection on MR and CT was more than the 3 mm matching threshold. This category of false positive was chosen if clear seed artifacts were visible on the MR scan, while on the CT scan a seed was detected nearby. When a one-to-one relationship was found between a FP and FN that were classified as incorrectly matched, we manually corrected the matching for these cases.
- Near other seeds (Fig. 4.4C): In this case the CT scan showed no seed at the location of the false positive, while one or more seeds were nearby.

- Outside the prostate (Fig. 4.4D): This category of false positive was located outside of the segmented prostate and no seed was visible on the CT scan.
- Unknown: This was chosen if none of the conditions for the other categories were satisfied.

The false negatives were classified in on the following categories:

- Incorrect automatic matching (Fig. 4.4B): This category of false negative was chosen if nearby a false positive was detected on the MR scan with clear seed artifacts visible.
- Near other seeds (Fig. 4.4E): In this case one or more seeds were visible on the CT scan near the false negative.
- Part of an unspaced strand of seeds (Fig. 4.4F): This category of false negative was chosen if the seed was determined to be part of an unspaced strand of seeds based on the planning of the treatment.
- Outside the region of interest: In this case the false negative was located outside the predetermined region of interest and was therefore unable to be detected.
- Unknown: This was chosen if none of the conditions for the other categories were satisfied.

The entire detection method was implemented in MATLAB (The Mathworks, Natick, MA, US). Library generation took approximately 35 seconds per template, adding up to a total of just over 3 hours for the complete library for each seed type. Seed detection took approximately 40 seconds per patient, varying slightly with the size of the region of interest and the number of seeds to be detected.

### 4.3 Results

Figure 4.1 shows the magnetic field distortions induced by the presence of a brachytherapy seed in a static magnetic field. In Figure 4.3A the artifacts resulting from these magnetic field distortions are visible in the magnitude images as well as the real and imaginary components of the complex-valued images. We observed a good correspondence between the simulated artifacts and the artifacts in actual MR scans. Even small differences in the artifacts due to the different compositions of the two types of brachytherapy seeds (Fig. 4.1) were simulated accurately. The examples in Figure 4.3A show distinct patterns in the real and imaginary components of the signal that were not present in the magnitude of the signal. This suggests that in a gradient echo sequence the complex-valued signal contains additional information regarding the position and orientation of the seeds, in comparison with the magnitude of the signal.

Figure 4.4E and 4.4F show examples of how the artifacts of multiple seeds can interact. In both the magnitude and the phase of the signal the artifacts were more complicated than a simple combination of the artifacts of individual seeds. In the case of the unspaced strand of Best 2301 seeds (Fig. 4.4F), the seeds in the middle of the strand showed almost no artifacts.

Table 4.1 shows the detection results for the 25 patients, split by patients who were treated with the Best 2301 seeds (Table 4.1A) and the selectSeed seeds (Table 4.1B). We observed a false negative rate of 4% for both types of seeds, a false discovery rate of 4% for the Best 2301 patients, and a false discovery rate of 5% for the selectSeed patients, where the false discovery rate is the percentage of all detections that were classified as false positives.

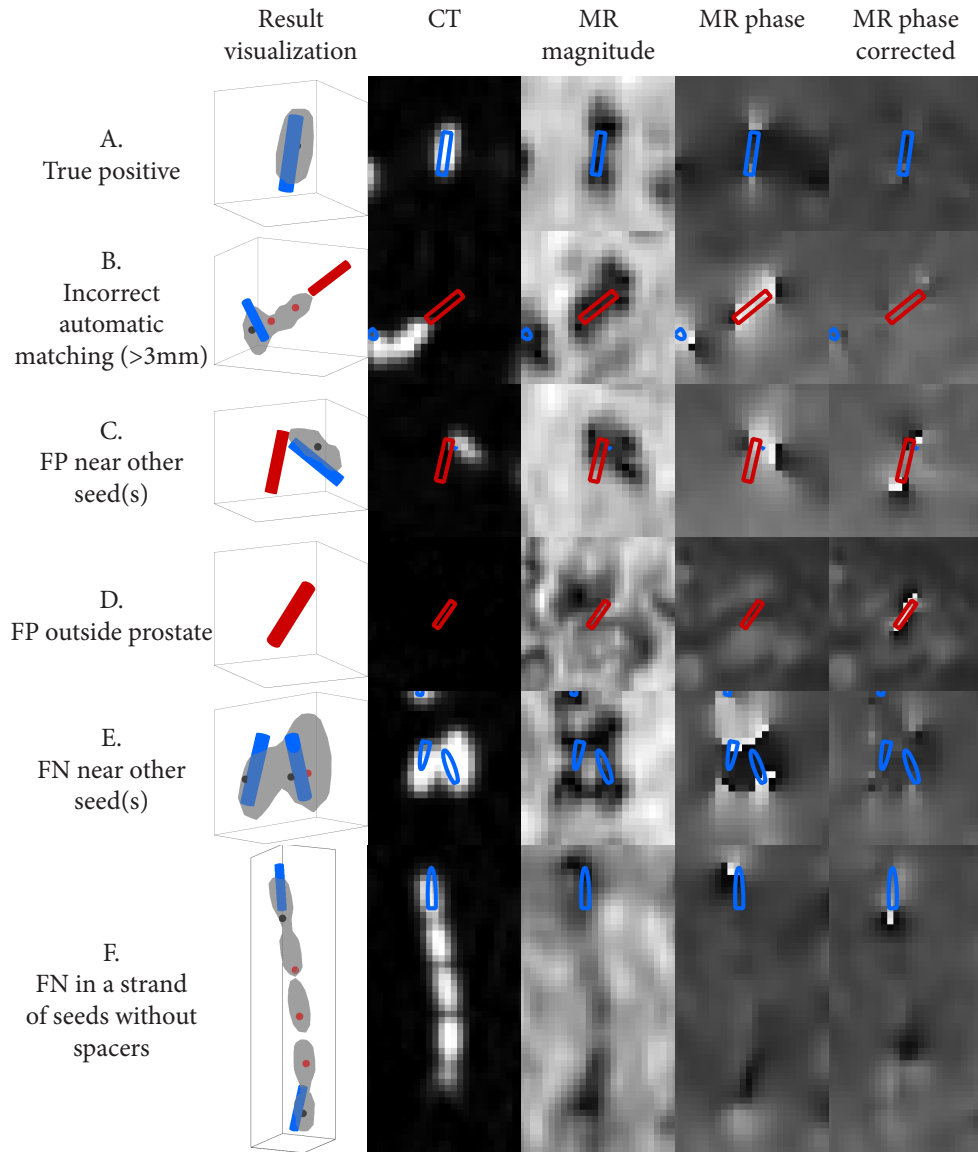


**FIGURE 4.4:** Examples of the conditions in which classification errors (false positive (FP) and false negative (FN)) occurred. For reference, A shows a true positive (TP) detection. In the first column a rendering of the detected seeds (blue cylinder = TP, red cylinder = FP), the gold standard locations (black dot = TP, red dot = FN), and the CT isosurface (gray) is shown. Columns 2-5 show representative oblique slices through these detections for the CT scan and MRI scans.

	Seeds implanted	Seeds counted on CT	TP	FP	FN	Dice overlap	Mean distance to CT (mm)	Standard deviation (mm)
Best 2301	1047	1046	1008	39	38	0.96	0.79	0.38
SelectSeed	510	501	482	28	19	0.95	0.83	0.46

**TABLE 4.1:** Detection results per seed type. Reported values include the number of true positives (TP), false positives (FP), false negatives (FN), and the mean and standard deviation of the distance of the distance from the MR-only detections to the registered CT detections.

	Total FP	Total FN	FP near other seeds	FP outside prostate	FN near other seeds	FN outside ROI	Total seeds in unspaced strands	FN in unspaced strands
Best 2301	39	38	28 (72%)	10 (26%)	1 (3%)	3 (8%)	73	31 (82% of FNs)
SelectSeed	28	19	17 (61%)	8 (29%)	8 (42%)	3 (16%)	42	7 (37% of FNs)

**TABLE 4.2:** Classification of the circumstances in which false positives (FP) and false negatives (FN) occurred per seed type. For each classification the absolute number of occurrences and the percentage of the total number of false positives or false negatives is indicated.

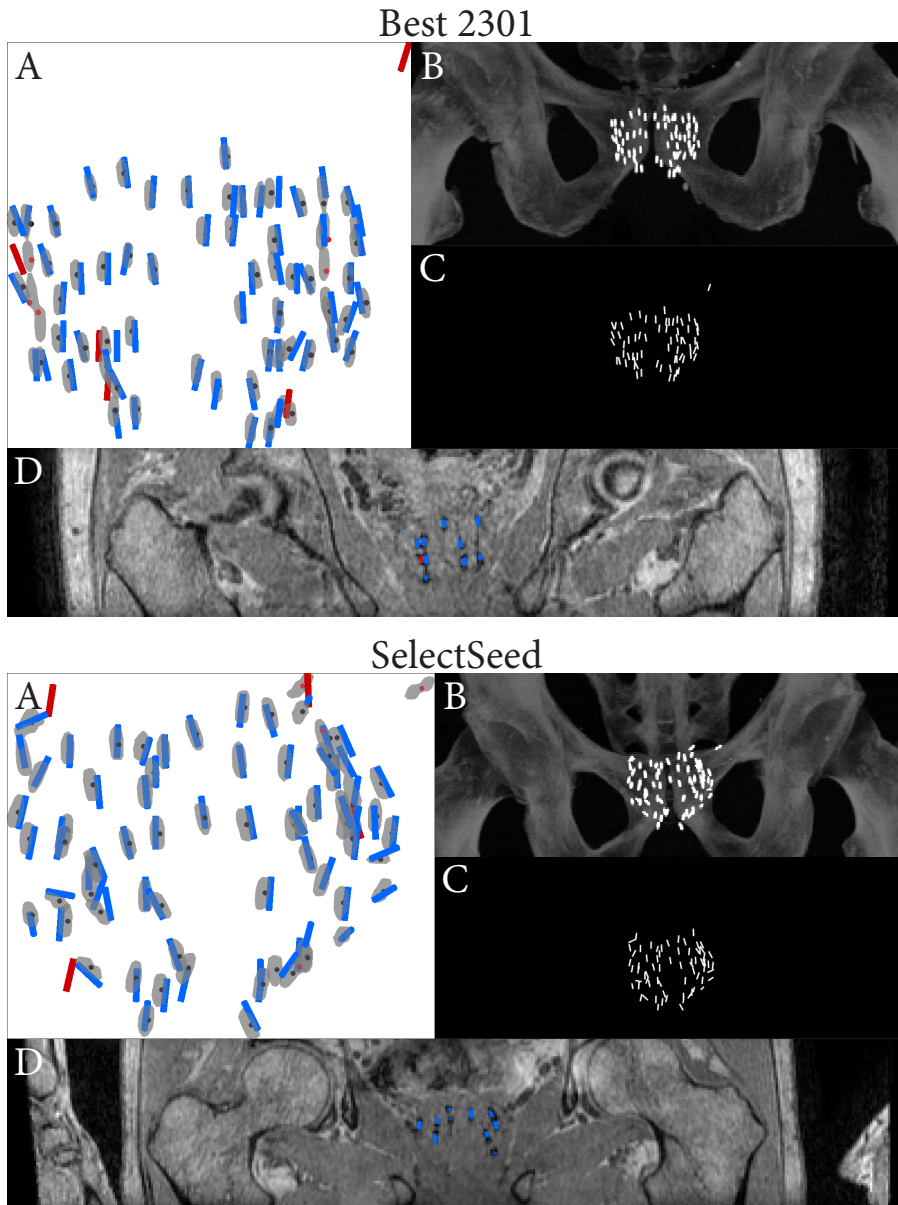
The true positive detections show a high spatial accuracy with regard to the registered CT locations. The mean distance was approximately 0.8 mm with 0.4 mm standard deviation, and in only two patients the mean distance was higher than 1 mm (Supplementary Tables 4.1 and 4.2).

Table 4.2 shows a summary of the classification of the detection errors. A total of 4 false positives and 4 false negatives did not satisfy any of the categories and were classified as unknown. False positives were most often found near other seeds: 72% for the Best 2301 patients, and 61% for the selectSeed patients. For the Best 2301 patients, 82% of the false negatives were located in unspaced strands, which accounts for 42% of the total number of seeds in unspaced strands. For the selectSeed patients the false negatives were approximately equally distributed between occurring near other seeds (42%) and in unspaced strands (37%).

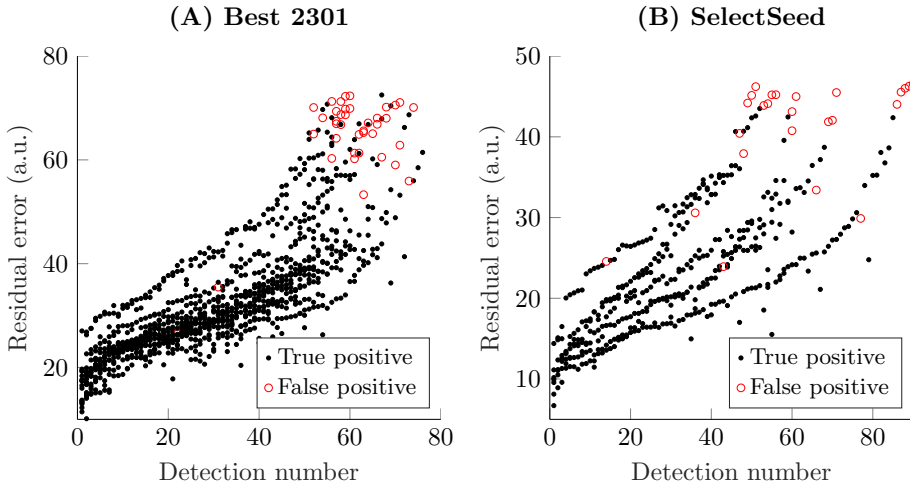
We corrected a total of 7 seeds that were not automatically matched because they were outside of the 3 mm matching threshold. During the classification process we also identified a total of 9 cases (6 FPs and 3 FNs) where an error in the CT gold standard was suspected. We made no corrections for these cases and selected the most appropriate classification, assuming the gold standard was correct.

Figure 4.5 shows the full detection results for one of the patients treated with the Best 2301 seeds (left) and for one of the patients treated with the selectSeed seeds (right). Both cases show a good correspondence between the detected seeds and the CT isosurface, in both position and orientation of the seeds.

Figure 4.6 shows the residual errors after regression for both seed types. This shows that most of the false positive detections were associated with high errors and were found



**FIGURE 4.5:** Detection results for a Best 2301 patient (left) and selectSeed patient (right). Frontal view of localization and detection results (A) overlaid on a registered isosurface of the CT scan (gray). MR-only detections are shown as cylinders (blue = true positive, red = false positive). The CT detections are shown as dots (black = true positive, red = false negative). B shows a maximum intensity projection of the CT scan, and C shows a virtual maximum intensity projection of the detected seeds. D shows a coronal slice of the MR scan.



**FIGURE 4.6:** Residual errors after regression analysis for the Best 2301 patients (A) and selectSeed patients (B). Each data point represents one MR-only seed detection, which was classified as either a true positive (black) or a false positive (red). The detection number is the order in which the seeds were detected per patient (i.e. the leftmost points were detected first).

late in the detection process.

## 4.4 Discussion

In this study, we applied a state-of-the-art MR-only seed localization method to in-vivo scans of 25 patients who were treated with one of two types of brachytherapy seeds. Out of a total of 1557 seeds we correctly localized 1490 seeds (96%). The total number of detection errors (false positives and false negatives) was 124, approximately 5 errors per patient on average. Although these numbers are promising, for postimplant dosimetry the error rate is most likely still too high to be clinically applicable at this stage. The presented data allow a study that compares dosimetry based on MR and CT with MR-only dosimetry, which could determine what error rate is acceptable for clinical practice.

We have analyzed the circumstances in which the detection errors occurred. Here we will discuss the sources of errors, to what degree they may be solved, and their impact on MR-only seed localization.

The main source of errors we found was related to configurations of multiple seeds in close vicinity to each other. Because artifacts of multiple seeds near each other interact, localizing seeds based on these artifacts will be challenging. This interaction causes false negatives when the artifacts are no longer recognizable as the artifacts of individual seeds. We recognized a special case of this error in unspaced strands, i.e. seeds that were implanted close to each other by design. In the Best 2301 patients, a large amount of seeds placed in unspaced strand configurations were missed (31/73), which was the majority of all FNs (31/38). However, in the selectSeed patients relatively few of the seeds in unspaced strands were missed (7/42) and these FNs formed a smaller fraction of the total number of FNs

(7/19). This can be attributed to the composition of the selectSeed: the diamagnetic core and paramagnetic hull induce a complex magnetic field around the seed, which partially persists in unspaced strands, aiding detection. Because of its relatively simple, paramagnetic nature, Best 2301 seeds in an unspaced strand induce a field more consistent with a metal cylinder, where the field is only perturbed near the start and end of the strand, making detection of the seeds in the middle of the strand particularly challenging.

In the selectSeed patients 8 out of 19 FNs occurred in the vicinity of other seeds, while for the Best 2301 patients this was only 1 out of 38 FNs. This may be due to the fact that all selectSeed seeds are loose when they are implanted, can thus move more freely, and may therefore end up very close to each other (Fig. 4.5, right). On the other hand, most Best 2301 seeds are physically linked in strands that are more rigid and therefore much less likely to end up in such configurations (Fig. 4.5, left).

These results show that the type of brachytherapy seed and the implantation techniques clearly influenced the MR-only detection results. Optimization of such factors could be beneficial in a clinical implementation of MR-only seed localization and postimplant dosimetry. For example, suppose a treatment plan can be designed such that no unspaced strands of seeds are implanted. With such a plan a majority of the FNs found in this study could have been avoided, which could make the proposed method competitive with CT-based seed localization. Alternatively, a priori information on the treatment plan could be used to improve upon our method. Under the assumption that seed migration is a rare occurrence, the seed locations are expected to closely match the treatment plan. This information could be useful in detecting false positives in locations where no seeds are expected, or to reconstruct strands of seeds with a priori information on the length and position of strands of seeds, which may be possible with methods previously applied to CT [98].

Seeds outside of the region of interest were a minor source of false negatives. Two out of six of these FNs were seeds that migrated to the seminal vesicles. The other four FNs were located just outside the ROI. Although extension of the ROI may have caused our method to find these seeds, it is important to note that extension of the ROI also increases the chance of false positive detections occurring, especially if the ROI includes anatomies such as the rectum.

For both seed types, most false positives occurred in the vicinity of correctly detected seeds. Interaction between artifacts around multiple seeds is likely to partially match with some template in the library. False positives were also commonly found outside the prostate, where signal around the rectum and around small bleeds or calcifications can resemble artifacts around brachytherapy seeds. Most of these false positives were associated with high residual errors after regression (Fig. 4.6), and were therefore found late in the detection process. These false positives could be partially eliminated by stopping the detection algorithm when the matching errors are too high. Similarly, improving local matching with additional criteria may help in eliminating false positives that do not resemble brachytherapy seeds, for example by locally analyzing the phase of the image with respect to the simulated phase around a seed. Such criteria may also be useful for human review and correction of the detection results; detections with high errors are likely to be false positives and could be flagged for a human operator to give it extra attention during review.

An important aspect of the proposed method is that it provides exact locations and orientations of the brachytherapy seeds. This is a clear advantage in comparison to methods that only provide visualization of seeds, for example through positive contrast mechanisms [66, 93, 94]. In order to achieve this exact localization, we do require that certain

prior knowledge is explicitly available. Most importantly, an exact model of the implanted brachytherapy seed must be available, including the magnetic susceptibility of the materials used in the seed. Furthermore, the exact scan parameters must be known, such as the  $k$ -space trajectory and the echo times. Other methods that do not require this prior knowledge could be easier to apply, in particular in cases where multiple types of seeds were implanted.

It is important to note that issues with seeds in close vicinity to each other are also likely to occur in other MR-only seed localization methods. Because the brachytherapy seed itself does not generate signal, information about the presence of a seed is always derived from tissue in the vicinity of the seed. Multiple seeds in close vicinity to each other will affect the same tissue, which then gives information about the presence of multiple seeds, but not about each seed individually. To resolve this issue, an MR-only localization method should be aware of the complex interactions occurring in such seed configurations. For example, the template libraries used in this study could be expanded with templates of a limited number of configurations of multiple seeds, based on prior knowledge of these specific configurations, such as the unspaced strands that caused most errors in the Best 2301 patients. However, due to computational limits it will be impossible to include all possible configurations of multiple seeds in a method that relies on template matching to locate seeds. A certain number of false positives and false negatives in multiple seed configurations can therefore be expected, especially if these configurations occur because of unpredictable phenomena, such as migration of seeds. An alternative approach could be to place positive contrast markers in strands of brachytherapy seeds to help localize these strands [99]. Our method could make use of these markers by including them in the simulation models. A downside of this approach is that it requires dedicated markers and is limited to stranded configurations of seeds.

In theory any pulse sequence or contrast mechanism proposed in other studies could be combined with our localization approach, provided that the effects around the brachytherapy seeds can be accurately simulated in reasonable time. In this way, methods that yield positive contrast may be turned into localization methods. When applying the proposed method to other pulse sequences, it is important to remember that the effects around the brachytherapy seeds should be sufficiently large to allow reliable localization, but small enough such that interactions between multiple seeds are limited. Because off-resonance effects scale with field strength, artifacts around the seeds will be smaller at lower field strengths. This can be compensated by scanning with longer echo times, or by using brachytherapy seeds with stronger magnetic susceptibilities. Conversely, at higher field strengths artifacts will be larger, which allows scanning with shorter echo times, and could allow localization of brachytherapy seeds with weaker magnetic susceptibilities.

In this study, we assumed the only information on the number of seeds was the number of seeds that were implanted. In practice, seeds are occasionally lost; the number of seeds that were counted on CT during postimplant dosimetry showed that 10 seeds that were implanted were not found (Table 4.1). This discrepancy resulted in 10 false positives. An appropriate stopping criterion would be required to deal with lost seeds, i.e. the method should only continue finding seeds when it is confident that the detections are real. A side-effect of such a stopping criterion would be that a failure to detect a seed no longer causes a false positive to be found in exchange.

The spatial accuracy of the true positive detections with respect to the CT detections was high, with an average error of 0.8 mm. The accuracy was probably limited by the fact

that the detections were made at the MR resolution of 1.2 mm. It may be possible to improve on this by adapting the detection method to perform template matching at a subvoxel resolution [100]. Furthermore, the measured errors include the CT to MR registration errors due to non-rigid deformations. The high accuracy across the dataset of 25 patients indicates that the proposed method performed robustly in clinical conditions. Artifacts from patient motion and breathing were benign and did not appear to influence the seed localization.

Further analysis is required to establish the influence of using MR-only seed localization on postimplant dosimetry. Of particular importance is the influence of the absence of CT to MR registration errors on dosimetry. Another topic of interest is the influence of detection errors. It is possible that a single false positive or false negative detection may not have significant effects on the dose-volume calculations, because of the low dose of an individual seed. Finally, the information on seed orientation gained through MR-only seed localization may improve the accuracy of the dose calculations by allowing the use of anisotropic dose distributions [101].

The proposed method is readily applicable in situations where fiducial markers have sufficient distance to each other, and therefore do not suffer from the challenges identified in this study. An example of such an application is the localization of gold fiducial markers for radiation therapy planning [27].

## 4.5 Conclusion

This study shows that MR-only brachytherapy seed localization could be clinically feasible if the proposed method is made more robust with respect to seed configurations with many seeds close to each other. This may be achieved by including simulations of problematic seed configurations such as seeds in unspaced strands, or alternatively, by adapting seed implantation to help avoid such seed configurations. Additionally, review by a human operator could help reduce false positives. Future research should establish whether dose distributions calculated based on a MR-only dosimetry workflow are of equal or better quality compared with the current clinical standard of using both CT and MR scans.

## 4.6 Supplementary material

Id	Seeds implanted	Seeds counted on CT	TP	FP	FN	Dice overlap	Mean distance to CT (mm)	Standard deviation (mm)
1	54	54	53	1	1	0.98	0.90	0.47
2	68	68	62	6	6	0.91	0.79	0.42
3	60	60	56	4	4	0.93	0.80	0.48
4	52	52	51	1	1	0.98	0.71	0.39
5	58	58	56	2	2	0.97	1.03	0.47
6	59	59	56	3	3	0.95	0.88	0.38
7	52	52	52	0	0	1.00	0.71	0.27
8	62	62	61	1	1	0.98	0.67	0.35
9	60	60	57	3	3	0.95	0.99	0.35
10	76	75	74	2	1	0.98	0.77	0.31
11	57	57	56	1	1	0.98	0.78	0.39
12	67	67	64	3	3	0.96	0.84	0.35
13	74	74	71	3	3	0.96	0.74	0.30
14	57	57	57	0	0	1.00	0.70	0.24
15	64	64	61	3	3	0.95	0.62	0.28
16	56	56	54	2	2	0.96	0.87	0.45
17	71	71	67	4	4	0.94	0.71	0.30
Total	1047	1046	1008	39	38	0.96	0.79	0.38

**SUPPLEMENTARY TABLE 4.1:** Detection results for Best 2301 patients. Reported values include the number of true positives (TP), false positives (FP), false negatives (FN), and the mean and standard deviation of the distance of the distance from the MR-only detections to the registered CT detections.

Id	Seeds implanted	Seeds counted on CT	TP	FP	FN	Dice overlap	Mean distance to CT (mm)	Standard deviation (mm)
1	60	60	59	1	1	0.98	0.68	0.30
2	40	40	39	1	1	0.98	1.14	0.61
3	90	85	84	6	1	0.96	0.80	0.37
4	71	71	67	4	4	0.94	0.86	0.51
5	51	51	47	4	4	0.92	0.82	0.46
6	56	54	50	6	4	0.91	0.89	0.54
7	81	80	78	3	2	0.97	0.75	0.32
8	61	60	58	3	2	0.96	0.89	0.53
Total	510	501	482	28	19	0.95	0.83	0.46

**SUPPLEMENTARY TABLE 4.2:** Detection results for selectSeed patients. Reported values include the number of true positives (TP), false positives (FP), false negatives (FN), and the mean and standard deviation of the distance of the distance from the MR-only detections to the registered CT detections.



**SIMULTANEOUS REAL-TIME ANATOMICAL  
IMAGING AND PASSIVE DEVICE TRACKING USING  
MULTI-ECHO UNDERSAMPLED RADIAL  
ACQUISITIONS FOR MR-GUIDED INTERVENTIONS**

**Based on:**

F. Zijlstra, M. A. Viergever, and P. R. Seevinck, "Simultaneous real-time anatomical imaging and passive device tracking using multi-echo undersampled radial acquisitions for MR-guided interventions," 2017, in preparation.

### Abstract

In this study, we propose a real-time passive device tracking method for MR-guided interventions that simultaneously acquires anatomical images to provide a frame of reference for visualization of the device. This was achieved by combining a previously proposed metal object localization methodology based on Phase Correlation template matching with a fast undersampled radial multi-echo acquisition using the white marker phenomenon. In a four echo acquisition, the first echo was acquired with regular anatomical contrast, whereas the remaining echoes were acquired with white marker contrast to provide positive contrast around metal devices. Fast simulations in radial k-space were used to simulate the white marker effects around the device, which were localized using template matching.

We tested this approach on tracking of five 0.5 mm steel markers in an agarose phantom and on an insertion of an MRI-compatible 20 Gauge titanium needle in *ex vivo* porcine tissue. The tracked locations of the steel spheres were compared with locations found using CT. The average pairwise distance between the MRI and CT locations was 0.30 mm for tracking of stationary steel spheres, which was close to the theoretical limit of a system that localizes objects on the MRI resolution of 1.2 mm. For tracking of moving steel spheres, we found an error of 0.29 mm which remained relatively constant during motion. Qualitative evaluation of the tracking of the needle insertions showed that tracked positions were stable throughout needle insertion and retraction. The anatomical contrast around the needle tip was almost undisturbed by off-resonance artifacts caused by the presence of the needle because of the low echo time and fast acquisition of the anatomical image.

The passive tracking method we proposed shares some advantages that are traditionally only available with active tracking methods: accurate tracking of devices at high framerates, the ability to include real-time anatomical scanning, and the capability of automatic slice positioning. Furthermore, the method does not require specialized hardware and could therefore be applied to track any rigid metal device that is safe for use in MRI and that causes sufficient magnetic field distortions.

## 5.1 Introduction

MR-guided interventions have shown promise in a variety of applications, including needle biopsies [102], vascular interventions [29, 103–105], and MR-guided radiation therapy [106, 107]. MRI has some distinct advantages when compared to other imaging modalities used for interventions, such as x-ray fluoroscopy or ultrasound. First, MRI offers superior soft tissue contrast with controllable weighting in terms of tissue and relaxation parameters, for example water, fat, or tissues with specific relaxation parameters can be highlighted or suppressed. Second, MRI can image in arbitrary, multiplanar orientations or 3D volumes. These orientations can be changed almost instantaneously without moving parts, which provides greater flexibility during interventions. In addition to these advantages and in contrast to x-ray fluoroscopy, no ionizing radiation is used in MRI, which is safer for both the patient and the operator.

However, in contrast to other modalities, most interventional devices used in MRI, such as metal needles and paramagnetic markers, do not generate contrast at the exact location of the devices. Instead, the presence of these passive devices causes artifacts in MR images due to magnetic susceptibility differences. The shape of these artifacts is non-trivial and can interfere with accurate localization of the devices [65]. For example, the signal void caused by a device is not necessarily representative for the actual location of the device, because the shape of the void can change depending on the acquisition parameters and the device orientation [28, 65], and it can be confounded with nearby anatomical signal voids.

Therefore, accurate localization of passive interventional devices is more difficult in MRI than in other modalities, which has been one of the main reasons for the lack of widespread clinical adoption of MR-guided interventions using devices. Instead, a lot of research has been performed in the last decade to improve real-time device visualization and overcome many of the drawbacks of conventional passive tracking. Current techniques for tracking devices in MRI can be broadly classified into passive, semi-active, and active tracking [108].

In passive tracking, the device is located based on its passive effect on the MR signal. The artifacts caused by magnetic field changes induced by the presence of a metal device can be detectable, either in anatomical images from standard pulse sequences [28, 65, 106] or in dedicated pulse sequences [103, 105, 109]. Alternatively, markers filled with contrast fluid can be added to devices to make them detectable in MR images [102, 110]. However, this requires specialized devices and will increase the minimal size of the devices.

Passive tracking methods can either generate positive contrast which can be visualized on an anatomical reference [103, 111], or the passive signal effects can be used to determine the exact location and orientation of the device [102, 105, 109, 110]. Acquiring anatomical images simultaneously with passive device tracking may not always be possible, especially in pulse sequences that include spectrally selective RF pulses.

Passive tracking has shown promise in a variety of applications, in particular in vascular interventions [29, 104]. The low hardware requirements of passive tracking make it flexible to the type of devices and markers that can be tracked. The accuracy and framerate achieved by passive tracking are mostly limited by the strength of the passive effect of the device. Larger devices and devices with strong magnetic susceptibilities will be easier to track. Dedicated pulse sequences that generate more specific contrast around the device can also enable faster, more accurate tracking [105, 109].

To overcome the limitations of passive tracking, (semi-)active tracking methods have been developed to provide fast and accurate tracking by using specialized hardware. In both

active and semi-active tracking, small RF coils are attached to interventional devices [108]. In the case of active tracking, these coils are attached to a receive channel on the scanner. The coil captures signal from a small region around the coil, which can be used to determine the location of the coil [112]. In semi-active tracking, the coils are tuned to the Larmor frequency and filled with a solution with a short  $T_1$ . In a fast pulse sequence with low flip angles these coils generate a high signal at the exact location of the coil [113].

In both active and semi-active tracking one-dimensional projections of the signal are acquired, in which a maximum can be detected that corresponds to the position of the object [114]. The 3D position of the coil can then be determined by triangulation. Because the signal from (semi-)active tracking sequences is very specific, very few projections are needed to accurately determine the position of the device. This process is very fast, and can in principle be interleaved with regular real-time scanning protocols to provide an anatomical reference for the localized device [112, 115]. The biggest disadvantage of (semi-)active tracking is that specialized hardware is required, which is costly and adds to the size of the devices. Furthermore, in active tracking there needs to be a wire connected to the device, which causes additional RF safety concerns due to potential heating [116].

We believe that in an ideal situation an MR-based device tracking method should share the advantages of both passive and active tracking, while minimizing the disadvantages. First, this means that the method must be accurate, robust, and should have real-time updates for device tracking (i.e. multiple updates per second). Second, the system should allow exact visualization of the device on an anatomical reference image, of which the slice position should automatically update. Ideally, this image would be acquired simultaneously to ensure that patient motion and deformation of the anatomies does not influence the accuracy of the visualization. Finally, the hardware used in the method should be safe, cheap to implement, and flexible with regard to clinical applications. For example, no outside connection to the scanner should be necessary, and any modification of the devices should not add to the size of the device to allow interventions in small vessels and with thin needles.

In this study, we aimed to develop a passive tracking method which satisfies these criteria. We propose a method that builds on previous research on dephased MRI [117] and the white marker phenomenon [118] to provide positive contrast near metal devices, and fast simulation and Phase Correlation template matching [95, 102] to exactly localize devices. An undersampled 2D radial multi-echo pulse sequence was used to achieve high update rates and to acquire anatomical contrast simultaneously with the device tracking. The proposed method requires no specialized hardware and can be applied to any metal device that induces sufficient magnetic field changes. We tested the method using on 0.5 mm steel markers in an agarose phantom and an MRI-compatible 20 Gauge titanium needle in ex vivo porcine tissue.

## 5.2 Theory

In this section we describe several advances we made to existing methodologies to make them applicable to the tracking method we propose in this study. First, we describe how the white marker phenomenon can be applied to a multi-echo sequence with an arbitrary number of echoes. Second, we extended a previously proposed fast simulation framework to provide simulations of the white marker phenomenon in pulse sequences that use non-Cartesian k-space trajectories. Finally, we describe how the Phase Correlation template

matching method can be applied to raw data acquired with non-Cartesian k-space trajectories.

### 5.2.1 White marker phenomenon

Seppenwoolde et al. described the white marker phenomenon for passive tracking in 2D gradient echo MRI scans [118]. The white marker phenomenon is a positive contrast mechanism that counteracts intravoxel dephasing caused by the presence of metal objects. This is achieved by applying an additional gradient in the slice direction that will conserve signal in regions where an opposite local field gradient is present, and that will attenuate the background signal [118]. The strength of the dephasing gradient can be varied to control the background attenuation and to obtain positive contrast at different locations near a metal object. Note that this dephasing gradient is similar to the phase encoding gradients applied in the slice direction in 3D scans.

In this study, we extend the white marker phenomenon to multi-echo gradient echo scans, where the strength of the dephasing effect can be varied per echo. This is achieved by adding gradients in the slice direction in between the readout windows for each echo, similar to EPI gradients. With this extension it is possible to scan both anatomical and white marker images simultaneously. In this study, we only used a gradient between the 1st and 2nd echo of a 4 echo acquisition. This yields a  $T_1$  weighted anatomical image with minimized off-resonance artifacts in the 1st echo. In the 2nd to 4th echoes, this yields images with the white marker contrast. The pulse sequence for this acquisition is shown in Figure 5.1.

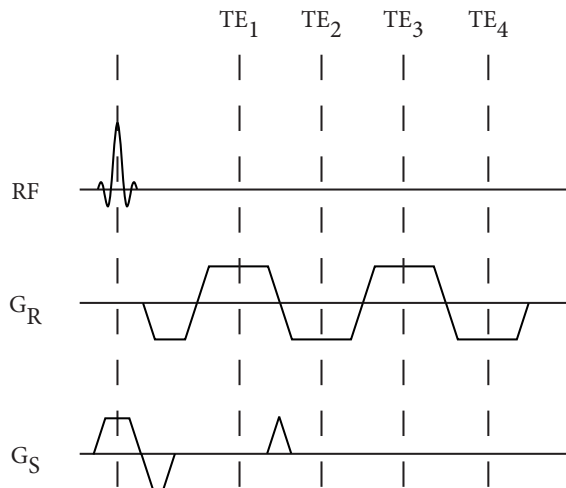


**FIGURE 5.1:** White marker pulse sequence for a gradient echo acquisition with 4 echoes. An additional dephasing gradient in the slice direction ( $G_S$ ) was added between the first ( $TE_1$ ) and second echo ( $TE_2$ ) to induce the white marker phenomenon in the 2nd to 4th echoes.

### 5.2.2 Non-uniform fast simulation

For the generation of a template library for the purpose of object localization, we aimed to simulate the white marker phenomenon around metal objects in radial MRI scans. To accomplish this we extended our previously proposed fast simulation framework (FORECAST) [95] to allow simulation of the white marker phenomenon, and to allow non-Cartesian sampling trajectories.

The FORECAST method uses the discrete Fourier transform to simulate time-varying effects along the readout direction and the fast Fourier transform to simulate phase encoding, which in a perfect steady-state is time-invariant. These Fourier transforms are applied to a complex spin density function, which includes proton density, off-resonance, and  $T_2$ , which allows fast evaluation of the following signal equation:

$$s(k_x, k_y) = \sum_z \sum_y \sum_x \rho'(x, y, z, t') e^{i2\pi\gamma\Delta B_0(x,y,z)t'} e^{-t'/T_2(x,y,z)} e^{-i2\pi(k_x x + k_y y)} \quad (5.1)$$

Here,  $\rho$  is the proton density at location  $(x, y, z)$ ,  $\Delta B_0$  is the off-resonance, the time point  $t'$  is the time after RF excitation, and  $k_x$  and  $k_y$  are the k-space locations at which the signal is evaluated.

Because the white marker phenomenon is similar to a phase encoding gradient, it is trivial to include the effect of this gradient in the signal equation used in FORECAST as a single encoding step in the  $z$  direction:

$$s(k_x, k_y) = \sum_z \sum_y \sum_x \rho'(x, y, z, t') e^{i2\pi\Delta B_0(x,y,z)t' + k_z z} e^{-t'/T_2(x,y,z)} e^{-i2\pi(k_x x + k_y y)} \quad (5.2)$$

To allow non-uniform sampling the method can be adapted by using a non-uniform fast Fourier transform (NUFFT) [73] for each unique time point  $t'$  to evaluate the Fourier encoding for all frequencies  $(k_x, k_y)$  sampled at time point  $t'$ . This approach is slightly less efficient than the original approach for Cartesian trajectories, because the readout and phase encoding cannot in general be separated in a non-Cartesian acquisition. Nevertheless, the speedup relative to Bloch simulation is still expected to be in the order of the number of repetitions of the pulse sequence.

### 5.2.3 Phase Correlation in non-Cartesian k-space

The Phase Correlation (PC) method was originally proposed for image registration [72], but has been shown to be usable as a template matching method to locate small structures in images [95, 102]. The PC operation is identical to cross-correlation followed by a normalization of frequency components to unit magnitude. In the frequency domain the PC operation is expressed as an element-wise operation:

$$C(\mathbf{k}) = \frac{I(\mathbf{k})\overline{T(\mathbf{k})}}{|I(\mathbf{k})\overline{T(\mathbf{k})| + \epsilon}} \quad (5.3)$$

Here,  $I$  is the frequency domain of the MR image,  $\overline{T}$  is the complex conjugate of the frequency domain of the template image,  $C$  is the frequency domain of the phase correlation image,  $\mathbf{k}$  is the location of the frequency domain element to which the operation is applied,

and  $\epsilon$  is a constant that prevents division by zero, which was set to  $10^{-15}$ . Because the PC method operates in the frequency domain, it can be applied to raw k-space data before image reconstruction. And because the operation is element-wise, it can also be applied to non-Cartesian raw k-space data before gridding reconstruction, as long as the template data is also represented in the same non-Cartesian space. Furthermore, there are no requirements on the non-Cartesian sampling pattern, which therefore may be undersampled.

## 5.3 Methods

The proposed device tracking method is a combination of dedicated acquisition, reconstruction, and tracking algorithms, which will be described separately in the following sections. Finally we describe the experiments we performed on phantoms with two different types of metal objects: small stainless steel spherical markers and an MRI-compatible needle.

### 5.3.1 Acquisition

The basic pulse sequence used in this study was an undersampled radial 2D gradient echo scan with 4 echoes (resolution =  $1.2 \times 1.2 \times 15$  mm; field of view =  $230 \times 230 \times 15$  mm;  $TE_1/TE_2/TE_3/TE_4/TR = 1.73/3.18/4.62/6.07/8.46$  ms; flip angle =  $10^\circ$ ; nr. of radial profiles = 192; dynamic scan time = 1.6 s), acquired at a field strength of 1.5T (Philips Achieva, Best, The Netherlands) using a 2-channel surface coil. We used a bit-reversed profile order [119] with an acceleration factor of 16, giving a scan time of 0.1 seconds per undersampled frame. This profile ordering allows approximately uniformly undersampled reconstructions up to an acceleration factor of 16.

The pulse sequence was modified with an additional gradient in the slice direction to induce the white marker phenomenon as described in the Theory section (Fig. 5.1). The strength of the gradient was chosen such that one complete cycle of dephasing (i.e.  $2\pi$  radians) was induced over the slice thickness.

### 5.3.2 Reconstruction

All reconstructions were performed retrospectively on raw acquired data, without further processing such as phase corrections. Sampling density correction was applied to the radial profiles, followed by gridding using the NUFFT library [73]. Images from the two receive coils were combined using the sum of squares method.

The first echo with anatomical contrast was reconstructed using a sliding window approach with a window of 16 frames, which yields a fully sampled k-space with a temporal resolution of 1.6 seconds.

Additionally, Phase Correlation (PC) images were reconstructed from single undersampled frames for all echoes. Before reconstruction, the PC method was applied to the raw undersampled k-space as described in the Theory section. These reconstructed PC images were corrupted by aliasing due to the undersampling. However, the aliasing was expected to be incoherent because of the radial sampling [120]. And because the PC images were expected to be sparse (i.e. there was a limited number of strong correlation peaks), the correlation peaks could still be expected to be detectable local maxima. Finally, the reconstructed PC images were multiplied pixel-wise to yield one combined PC image. Implicitly,

this means that in order to detect an object, the PC image for each echo must have a strong correlation peak.

The templates used in the PC matching were simulations of the metal object in a uniform background, using the scan parameters, undersampling scheme, and echo times specific for each echo and each frame. These simulations were performed with the non-Cartesian FORECAST method, as described in the Theory section. For the 2nd to 4th echoes the white marker dephasing gradient was also simulated.

The objects were simulated at an isotropic resolution of 0.15 mm in a  $25 \times 25 \times 15$  mm field of view (i.e. 6400 spins per pixel). The simulation models were based on physical models of the objects: The stainless steel spheres had a diameter of 0.5 mm and had an estimated magnetic susceptibility ( $\chi$ ) of 5000 ppm. The needle was of type MRI Chiba (SOMATEX<sup>®</sup>, Berlin, Germany), which consists of a titanium needle ( $\chi$  190 ppm) and a nitinol mandrin (est.  $\chi$  600). Only the artifacts around the needle tip were simulated, and the orientation of the needle was assumed to be known a priori.

### 5.3.3 Tracking

Although it is possible to extract positions from the PC image for each undersampled frame individually, we opted to use a tracking algorithm to estimate the position of the object(s) over time to increase robustness.

We implemented a basic Kalman filter [121] with a linear motion model that includes the position and velocity of the object:

$$x_{i+1} = x_i + dtv_i + N_x \quad (5.4)$$

$$v_{i+1} = v_i + N_v \quad (5.5)$$

Here,  $x$  is the 2D position of the object,  $v$  is the velocity vector,  $dt$  is the discrete time step of the model, and  $N_x$  and  $N_v$  describe normally distributed process noise (i.e. how fast the values are allowed to change). The measurement with which the model was updated was a single measured position  $z$  per frame:  $z_i = x_i + N_z$ , where  $N_z$  describes normally distributed measurement noise.

The measured positions were extracted from the PC image by finding a location that optimizes both the PC intensity and the distance to the previously predicted location of the object. Candidates for these locations were required to be a local maximum in a  $7 \times 7$  region in the PC image. In the case of tracking multiple identical objects, we used the Hungarian Method [122] to optimally assign a candidate position to each object.

The tracking was initialized by performing a fully sampled reconstruction of the first fully sampled frame. The initial locations were found by locating maxima in the PC image.

The process and measurement noise covariance were experimentally determined. Process noise was set to a standard deviation of 1 voxel per second for the position, and 10 voxels per second per second for the velocity. Measurement noise was to a standard deviation of 0.5 voxel.

### 5.3.4 Experimental setup

We performed experiments with two different types of metal objects: small spherical steel markers and an MRI-compatible biopsy needle. The primary goal of the experiments with

the steel markers was to show feasibility and to establish the accuracy of the proposed method. The steel markers can be seen as a surrogate for other small markers that create dipolar field distortions, such as markers on a guidewire. The experiments with the needle serve as a proof of concept for clinical applications. The larger, orientation-dependent artifacts created by a needle are similar to other types of interventional devices, such as DBS-applicators and HDR brachytherapy sources.

For the first series of experiments we created a cylindrical phantom containing 5 steel markers (0.5 mm diameter) in a cross pattern in a 2% agarose gel. The phantom was scanned with our proposed tracking sequence in four different conditions: 1) stationary, 2) moving linearly along  $B_0$  with varying speeds, 3) rotating in the coronal plane with varying speeds, and 4) rapidly moving and rotating at the same time. Tracking was applied to the 5 markers independently.

For the second series of experiments we inserted an MRI Chiba (SOMATEX<sup>®</sup>, Berlin, Germany) needle into ex vivo porcine tissue. The inserted needle was scanned with our proposed tracking sequence in three different conditions: 1) stationary, 2) needle inserted and retracted linearly along  $B_0$  with varying speeds, and 3) needle inserted and retracted linearly at an approximately 45 degree angle with  $B_0$  with varying speeds.

For the stationary experiments we also scanned the phantoms with anatomical contrast in all echoes and white marker contrast in all echoes. This allowed a comparison between anatomical and white marker contrast in both fully sampled and undersampled scans.

To validate the steel marker positions we acquired a CT scan of the marker phantom (resolution  $0.21 \times 0.21 \times 0.67$  mm). The marker positions in the CT scan were located by finding the center of mass of connected components with voxel values larger than 2000 HU. We performed a rigid registration of the CT scan to a 3D gradient echo scan of the marker phantom (resolution  $1 \times 1 \times 2$  mm), which was acquired in the same session as the stationary experiment. The CT marker positions were registered to the MRI coordinate space using the resulting transformation. Because the markers were stationary with respect to the phantom, they could be directly compared to the registered CT marker positions.

In the dynamic tracking experiment with the steel marker phantom, no direct comparison could be made to the CT marker positions, since the position of the phantom over time was unknown. Instead, for each frame we performed a rigid registration of the CT marker positions to the tracked positions in MRI using the Coherent Point Drift method [96]. After registration the error in position was calculated for each marker. Any errors in the positions indicate deformation of the tracked configuration of the 5 markers with respect to the configuration found on CT.

Finally, we performed an experiment using dual plane tracking of a needle insertion. For this approach, 16-fold undersampled 2D acquisitions for coronal and sagittal slices were interleaved. The basic acquisition and reconstruction strategy remained unchanged. The tracking model was extended to 3D positions, where coronal slices updated the left-right and feet-head positions, and sagittal slices updated the anterior-posterior and feet-head positions. This means the left-right and anterior-posterior positions were updated at a rate of 5 Hz, while the feet-head position was updated at a rate of 10 Hz. Both the coronal and sagittal anatomical images fully updated once every 3.2 seconds.

## 5.4 Results

### 5.4.1 Stationary objects

Figure 5.2 shows the MRI scan and corresponding MRI simulation for a single steel marker and the tip of the titanium needle in our multi-echo pulse sequence with simultaneous anatomical and white marker contrast. Overall the shape and intensity of the simulated artifacts around the objects had a good correspondence with the actual MRI scan. Some small differences in the artifacts can be observed, which could be attributed to noise, partial volume effects due to sub-voxel shifts, and factors that were not included in the simulations, such as accurate simulation of the RF excitation pulse.

Figure 5.3 shows the difference between performing PC template matching on anatomical contrast and white marker contrast for the 4 echoes. First, as may be expected, the signal void related to intravoxel dephasing increases with increasing echo number (and echo time). The same holds for the white marker phenomenon, the size of which increases with increasing echo time. For the white marker contrast we observed a reduction in high intensity correlations in other structures, especially around sharp edges in the anatomical images. In general we observed that the background dephasing in the white marker images was incomplete in many areas. This can be explained by structural variation over the slice, as well as presence of fatty tissue and bone. Additionally, variation in the background field and in the coil sensitivity over the slice direction may cause dephasing to be incomplete. Some increased correlations in the PC images can be observed at locations that have not dephased completely, which is particularly visible in the porcine tissue.

Figures 5.4 and 5.5 show the effect of 16-fold undersampling on PC template matching using the proposed pulse sequence for the steel markers (Fig. 5.4) and the needle (Fig. 5.5). In the echoes with white marker contrast we observed a reduction of streaking artifacts in the PC images, which suggests that the white marker contrast around objects is more specific than anatomical contrast. Most of the aliasing artifacts due to undersampling were effectively removed by taking the product of the PC images. Even at 16-fold undersampling the objects were still well-defined in the product of the PC matching on all echoes, with only minor blurring of the correlation peak.

Figure 5.6 shows the localized markers (blue) in the stationary steel marker phantom overlaid on the anatomical contrast for the last undersampled frame in our proposed tracking sequence, alongside the registered CT scan and the markers as localized on CT (red). The mean pairwise distance between the CT locations and the MRI locations over the entire scan sequence is shown in the bottom panel of Figure 5.6. The average distance over the entire sequence was 0.30 mm. This shows that the MR-based tracking was accurate and stable over time with respect to the configuration found on CT.

### 5.4.2 Moving objects

Figure 5.7 shows the results of the proposed tracking method applied to a dynamic scan sequence where the steel marker phantom was manually moved in a linear fashion along the bore of the scanner (feet-head [FH] direction) at varying speeds. A movie of this sequence is available as Supplementary Movie 1. The FH-positions of the 5 markers all follow the motion pattern of the phantom very consistently, even at the highest speed of over 4 cm/second. However, at these speeds it does become apparent that the sliding window re-

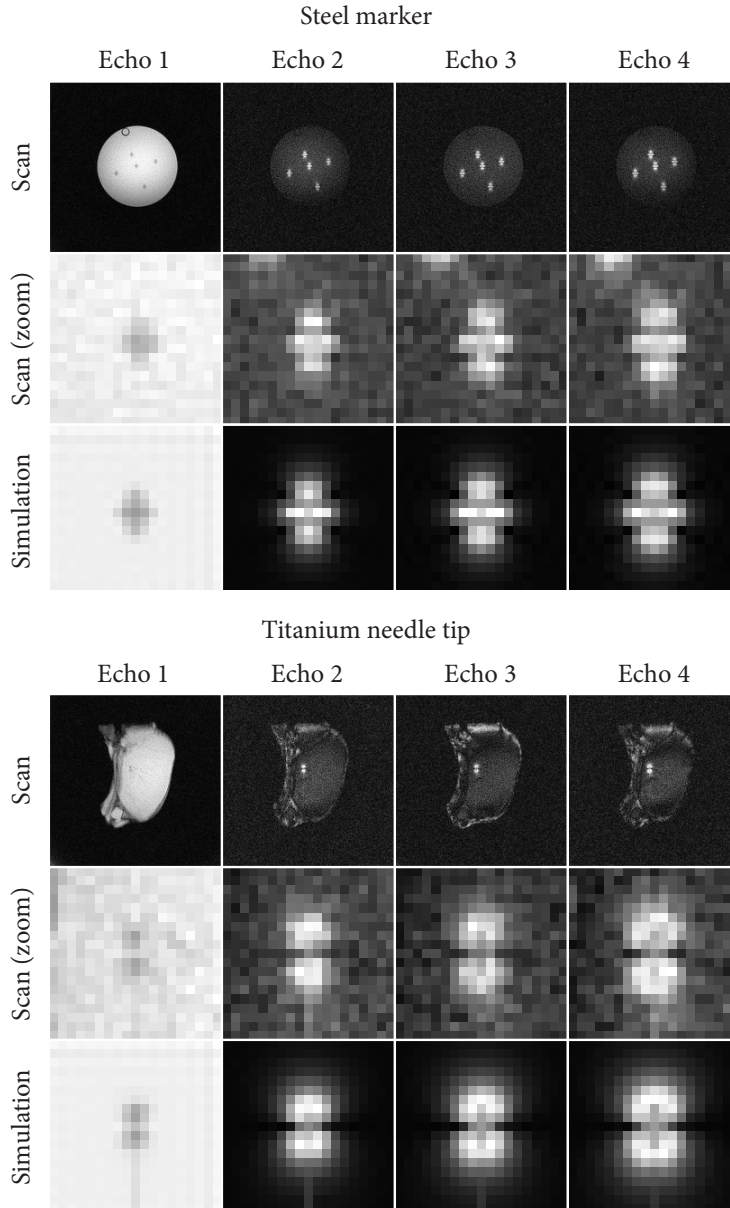


**FIGURE 5.2:** MRI scan and MRI simulation using the proposed multi-echo pulse sequence for a single steel marker (top) and tip of a titanium needle (bottom). The first echo shows anatomical contrast, whereas the 2nd to 4th echoes show white marker contrast.

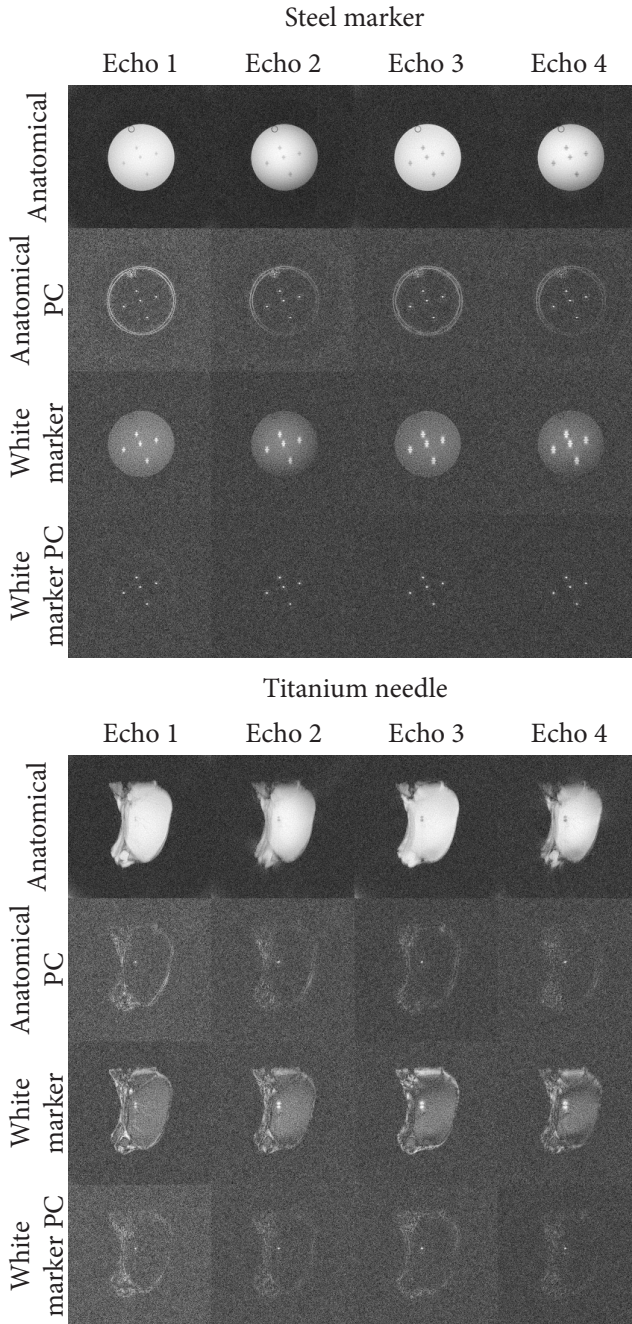


**FIGURE 5.3:** MRI scans and Phase Correlation (PC) maps on anatomical (rows 1 and 2) and white marker (rows 3 and 4) contrasts for the steel markers (top) and a titanium needle (bottom). Images are shown for all 4 echoes of the pulse sequences.

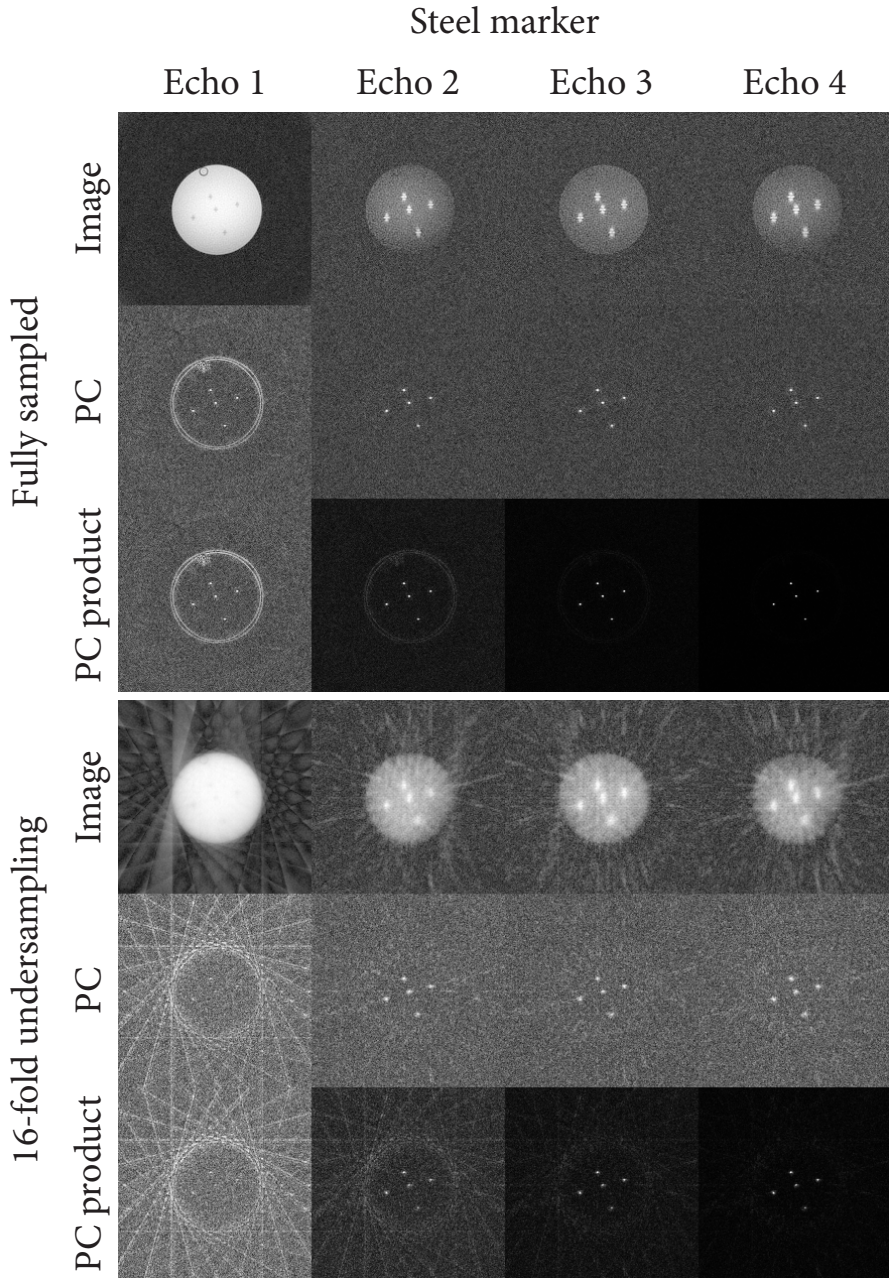


**FIGURE 5.4:** MRI scans and Phase Correlation (PC) maps for fully sampled (top) and 16-fold radially undersampled (bottom) acquisitions with the proposed pulse sequence for the steel markers. The last row of the top and bottom sections shows the product of all PC images up to the current echo.

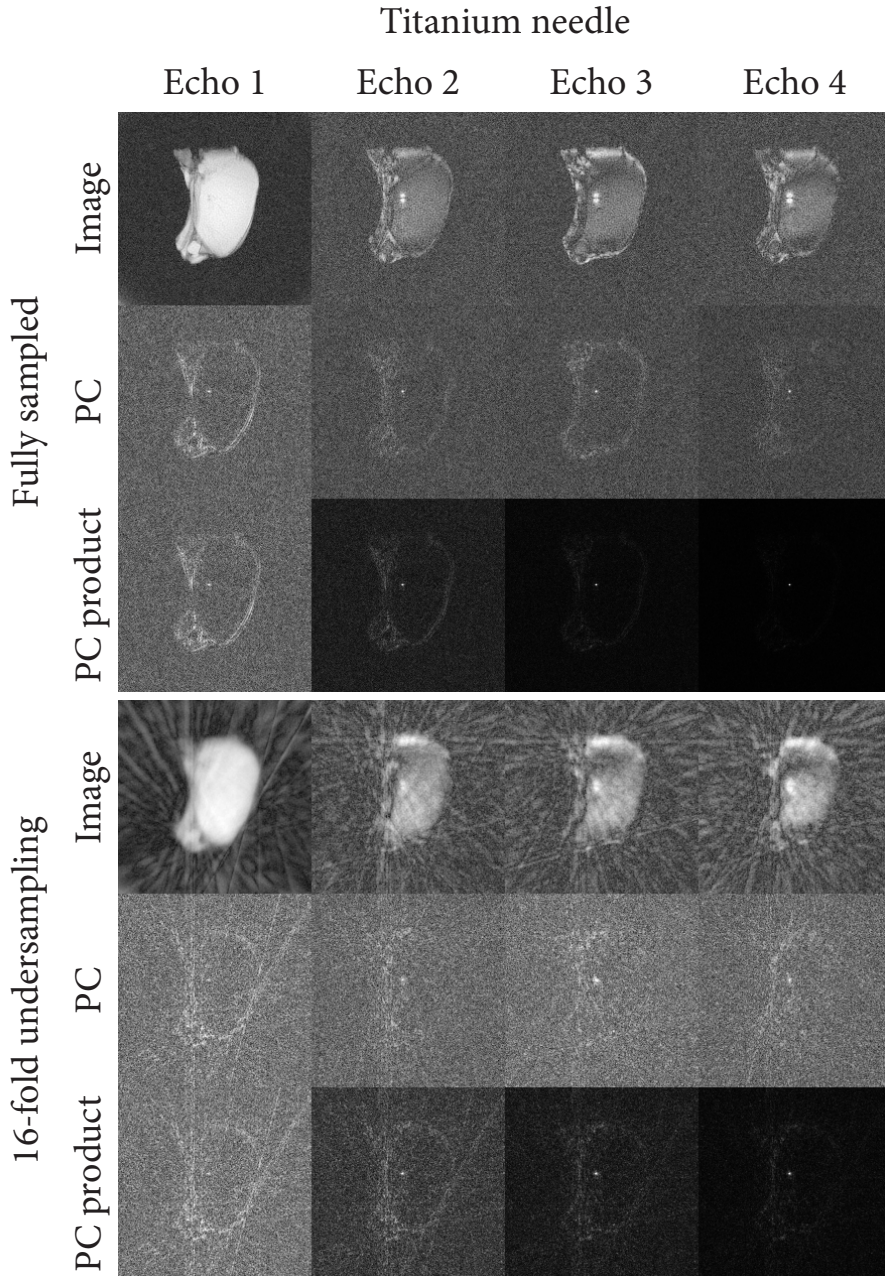


**FIGURE 5.5:** MRI scans and Phase Correlation (PC) maps for fully sampled (top) and 16-fold radially undersampled (bottom) acquisitions with the proposed pulse sequence for the titanium needle. The last row of the top and bottom sections shows the product of all PC images up to the current echo.

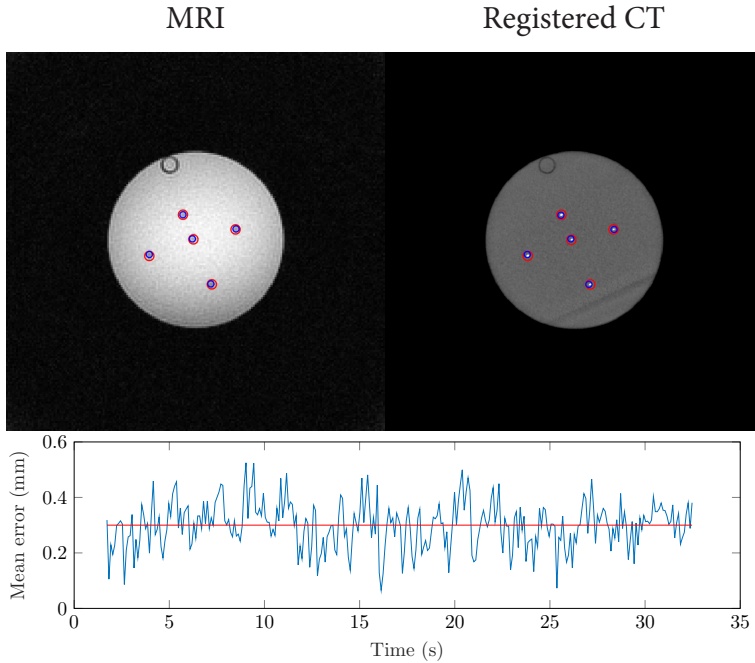


**FIGURE 5.6:** Steel markers localized on both MRI (left) and CT (right) scans. The tracked positions of the markers at the end of the MRI tracking sequence are shown as blue circles. The marker positions detected on CT are shown as red circles. The bottom graph shows the mean error of the MRI positions with respect to the CT positions over the entire tracked sequence. The mean error over all time points is shown in red and was 0.30 mm.

construction of the anatomical image has a lower temporal resolution, which results in a smeared image that lags behind the tracked marker positions.

The mean error of the marker locations compared with the registered CT locations was 0.29 mm on average. The motion of the phantom did not appear to influence this error. This indicates that the configuration of the tracked markers was consistent with the configuration of the markers as found on CT, even during motion.

In the supplementary material the results of two additional motion sequences for the steel marker phantom are available. Supplementary movie 2 shows mostly rotational motion. Supplementary movie 3 shows both translational as well as rotational movement in both directions and with fast and abrupt changes in velocity. In this sequence, the tracking algorithm lost the positions of the markers at one point in time, but restored automatically after just a few frames.

Figure 5.8 shows the results of the tracking method applied to locating the tip of a needle in a ex vivo porcine tissue as it was being inserted and retracted along the bore of the scanner with varying speeds. The full tracked sequence is shown in Supplementary movie 4. The tracked position of the needle tip was stable and smoothly moving throughout the tracking sequence, consistent with linear insertions and retractions of the needle. Note that in the anatomical image the off-resonance artifacts caused by the needle are minimized because

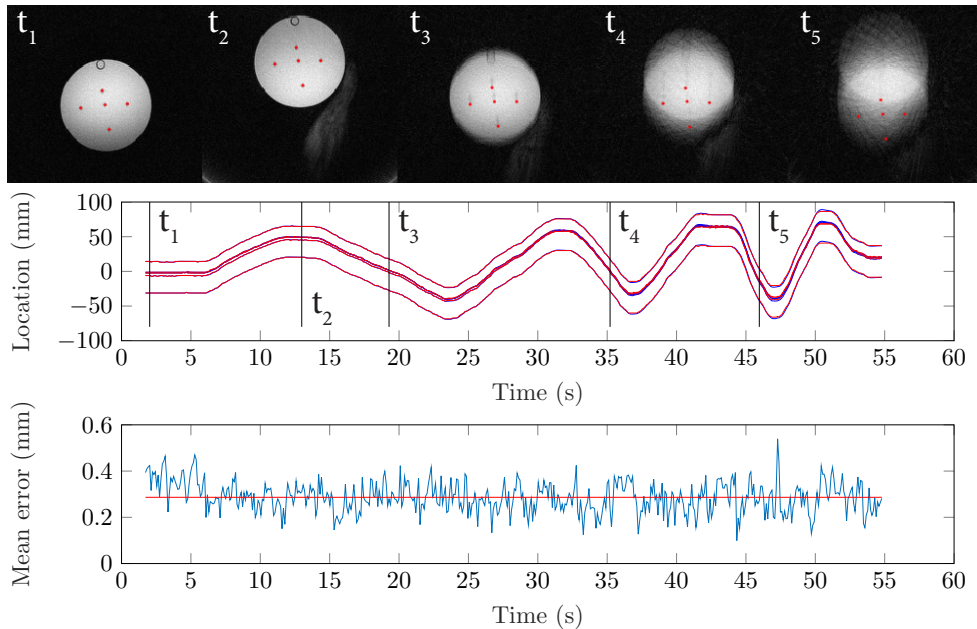


**FIGURE 5.7:** Tracking results for a dynamic sequence where the steel marker phantom was moving in a linear fashion along the bore of the scanner (feet-head direction). Anatomical images with the marker locations superimposed (red) are shown for five frames (top). The middle graph shows the measured (red) and tracked (blue) feet-head locations of all 5 markers over time. The bottom graph shows the mean error of the marker locations with respect to registered CT locations. The mean error over all time points is shown in red and was 0.29 mm. The full sequence is available as Supplementary Movie 1.

of the short echo time. Almost no signal void is visible around the needle tip, which allows accurately visualization of the anatomy around the needle tip during tracking. An insertion of the needle at an angle of 45 degrees relative to  $B_0$  is shown in Supplementary movie 5. Although the artifacts in this sequence were larger due to the angulation, the anatomy around the needle tip is still visible.

Figure 5.9 shows one frame of the dual plane tracking approach with a 3D visualization of the needle during insertion and retraction. The full movie is available as Supplementary movie 6. A dark band is visible in the anatomical images where the two planes overlap, which is caused by increased saturation of the signal, because this tissue is excited twice as often as the rest of the tissue. Despite this dark band and the lower refresh rate of the anatomical images, deformation of the tissue can still be observed during insertion of the needle.

## 5.5 Discussion

In this study, we have demonstrated a passive tracking framework that allows real-time tracking of metal objects in 2D MRI at a rate of 10 updates per second, while also providing an anatomical image with a temporal resolution of 1.6 seconds. The anatomical image

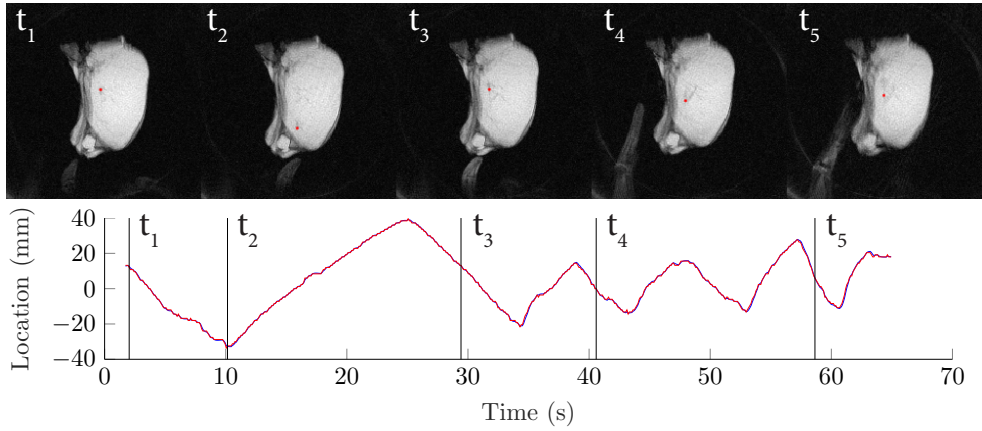


**FIGURE 5.8:** Tracking results for a dynamic sequence where a titanium needle was inserted into ex vivo porcine tissue along the bore of the scanner (feet-head direction). Anatomical images with the needle tip location superimposed (red) are shown for five frames (top). The bottom graph shows the measured (red) and tracked (blue) feet-head locations of the needle tip over time. The full sequence is available as Supplementary Movie 4.

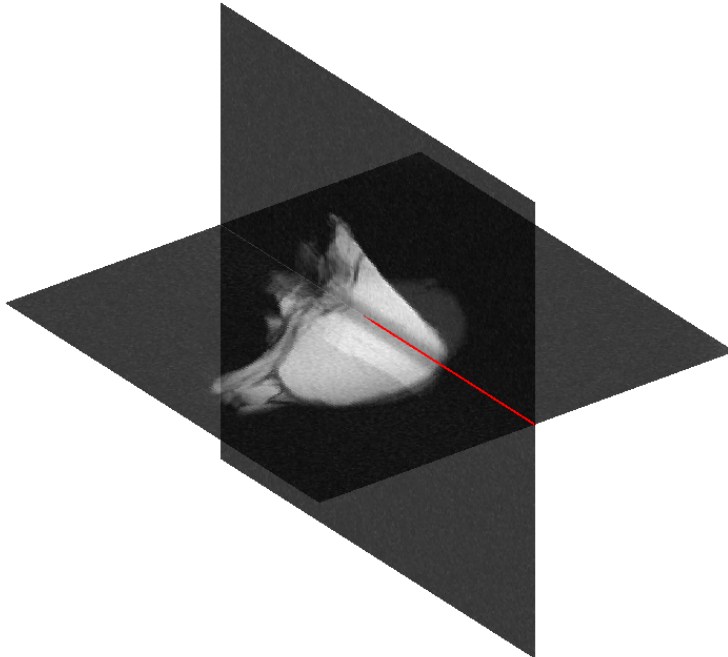


**FIGURE 5.9:** 3D Visualization of a needle (red) in ex vivo porcine tissue that is being tracked using the proposed dual plane approach. The anatomical images are slightly transparent to allow a volumetric view of the entire field of view. The full sequence is available as Supplementary Movie 6.

was acquired in the echo with the shortest echo time, which minimized off-resonance artifacts around the objects. Because both the object localization and the anatomical image were simultaneously acquired with the same pulse sequence, the tracked positions of the objects were intrinsically registered to the anatomical image. Any distortion to the anatomical image (e.g. due to gradient non-linearity) would have also been present in the Phase Correlation images used for localization.

The accuracy of our method was validated against a high resolution CT scan of a phantom containing 5 steel markers. The mean localization error for the stationary phantom was 0.3 mm, which was near the theoretical limit of a system that localizes on the MRI resolution of 1.2 mm. This limit may be overcome by performing PC template matching at sub-voxel resolutions [100], which may further improve the accuracy of our method. The mean localization error for the moving phantom was 0.29 mm, which was comparable to the stationary results. It should be noted that the analysis on the moving phantom was limited to measuring the accuracy of the internal configuration of the markers, because the pointset registration was able to correct for any systematic errors.

The tracked positions appeared to be robust at velocities much higher than those that would be expected in interventional applications. In only one of the 6 tracked sequences the method failed to track the positions correctly over the entire sequence, and even in this case the tracking failed very briefly and automatically recovered afterwards. Further experiments are needed to test the robustness of the method *in vivo*, with moving anatomies and more heterogeneous tissues.

In clinical situations there may be unfavorable circumstances which may compromise passive tracking of devices, for example when there is low signal in the vicinity of the device. These situations may occur when the object is located in a region with low proton density or low  $T_2^*$ , for example in the vicinity of air, in bone, or in turbulent flow. In our method these situations would lead to a reduced PC intensity, which could be detectable and communicated to the operator. Once the object is well-detectable again, tracking can be reinitialized using a fully sampled reconstruction while the object is stationary, identical to the first initialization. These processes can be automated and would not require manual interaction of the operator. Alternatively, hardware changes may allow tracking of devices that are partially undetectable. For example, additional markers could be placed on a needle to allow localization even when the tip of the needle is not detectable.

It is important to note that the framework we proposed is very flexible with regards to the pulse sequence. First, the number of echoes, the echo times, and the contrast used in each echo (anatomical or white marker) can be freely chosen. Varying the amount of dephasing per echo could add additional information for the localization, especially for larger objects. This may allow imaging with fewer echoes, which would lead to higher frame rates. Second, the proposed framework is independent of the sampling scheme and undersampling rate. Instead of radial sampling, the methods described in this study could be applied to conventional Cartesian acquisitions or other non-Cartesian acquisitions, such as spiral sampling. Finally, the slice thickness may be increased beyond the 15 mm thickness we used in this study, as the white marker contrast can be maintained even for thicker slices [118].

The method is also flexible with regard to the device being tracked. The main requirement is that the artifacts around the device can be accurately simulated in a single template. In turn, this requires that the device has a rigid shape, and that the artifacts are either independent of orientation, or that the orientation of the object is known a priori and constant while it is being tracked. For example, the approximate angle of a needle insertion would

be planned before the intervention and would therefore be known. Alternatively, a library of templates for multiple orientations of the object could be simulated [28, 95, 105]. PC maps for multiple templates could be reconstructed during the tracking in order to detect changes in the orientation of the object, at the cost of an increased computational load.

This flexibility with regard to the device allows novel design of interventional hardware to optimize it for passive tracking. Using materials with strong magnetic susceptibilities can aid localization, because larger artifacts carry more information about the position of the object, which leads to a more specific correlation peak. A stronger correlation peak could allow larger undersampling factors. In the extreme case, the correlation peak could be detectable in a single projection, which would allow a position update after every repetition of the pulse sequence, similar to how (semi-)active tracking operates. Conversely, objects that cause smaller artifacts may require lower undersampling factors to be accurately tracked with the proposed method. Interestingly, using scanners with higher field strengths would allow smaller objects to be tracked, because magnetic susceptibility artifacts scale with the main magnetic field strength [59].

Finally we have shown that the proposed method is directly applicable to dual plane tracking, where the slice orientation of every undersampled frame is alternated between the two planes. This lowered the anatomical framerate by a factor 2, but enabled the method to track the position of the device in all 3 dimensions. In every frame, the position of the device was updated in the 2 dimensions of the plane that was imaged in that frame. This means that in the dimension that was shared between the two planes the tracking was performed at 10 updates per second, identical to the single plane approach, while the other 2 dimensions were updated 5 times per second.

In a system integrated with the scanner software, this dual plane approach would allow automatic slice positioning to keep the scanning planes centered on the device. In this sense, the proposed passive tracking method possesses properties generally thought to be exclusive for active tracking.

The passive tracking method we proposed in this study shares some of the advantages that are traditionally only available with active tracking methods: accurate tracking of devices at high framerates, the ability to include real-time anatomical scanning, and the capability of automatic slice positioning. At the same time the proposed method does not require specialized hardware. Instead, any rigid metal device that is safe for MRI and that causes sufficient magnetic field distortions can be tracked using this method. While more experiments are required to definitively prove the robustness of the method in clinical applications, the results in this study are promising for a flexible, low-cost approach to MR-guided interventions.

## 5.6 Supplementary material

The following supplementary movies show the full reconstructions for the tracking experiments performed in this study. In the movies, the tracked position of an object is shown as a red point and the raw position measurements are shown as a green point.

The movies are available online at: [http://www.isi.uu.nl/People/Frank/Thesis/Steel markers](http://www.isi.uu.nl/People/Frank/Thesis/Steel%20markers):

- Supplementary Movie 1: The phantom was manually moved in a linear fashion along the bore (feet-head direction) with varying speeds.

- Supplementary Movie 2: The phantom was rotated with varying speeds.
- Supplementary Movie 3: The phantom was both moved and rotated with high speeds.

Titanium needle:

- Supplementary Movie 4: The needle was inserted and retracted linearly along  $B_0$  with varying speeds.
- Supplementary Movie 5: The needle was inserted and retracted linearly at an approximately 45 degree angle with  $B_0$  with varying speeds.
- Supplementary Movie 6: Dual plane tracking where the needle was inserted and retracted linearly along  $B_0$  with varying speeds.





CHAPTER



## SUMMARY AND DISCUSSION

## 6.1 Summary

In this thesis we aimed to incorporate prior knowledge in the MRI acquisition, reconstruction, and image analysis pipeline to accelerate MRI and to localize metal devices in MRI. We have shown two different approaches for using prior knowledge. First, we demonstrated that undersampling patterns for Compressed Sensing can be optimized for a specific anatomy using a dataset of previous scans of that anatomy. Second, we have shown that models of metal devices can be used to predict the artifacts that the device will cause in an MRI scan. Using these predicted artifacts, the device can be accurately localized in an MRI scan using template matching. Finally, we demonstrated that the specificity of these artifacts allows localization of devices in real-time using highly undersampled acquisitions. Together, these studies show the value of using prior knowledge in MRI and how it can help accelerate MRI and localize metal devices in MRI.

In **Chapter 2** we investigated the influence of different undersampling patterns on reconstruction quality for Compressed Sensing (CS) in datasets of knee and brain MR scans. First, we investigated the influence of randomness and sampling density in random variable density and variable density Poisson disk undersampling. Second, we investigated whether data-driven undersampling methods could improve reconstruction quality when one or more fully sampled scans were available as prior knowledge. We implemented three different data-driven undersampling methods: (1) Monte Carlo optimization of variable density and variable density Poisson disk undersampling, (2) calculating sampling probabilities directly from the k-space power spectra of the training data, and (3) iterative design of undersampling patterns based on CS reconstruction errors in k-space. Using cross-validation and retrospective undersampling we evaluated the three methods and the influence of the number of scans that were available as prior knowledge. Finally, we applied two of the data-driven methods prospectively to show their practical applicability.

We found that optimal sampling densities were different for each of the datasets, which shows that the optimal sampling density is data-dependent. This suggests that choosing a sampling density without any prior knowledge is likely suboptimal. For the data-driven methods, we found that the iterative design method yielded significantly higher reconstruction quality in both retrospective and prospective experiments. The two other data-driven methods yielded similar reconstruction qualities which were close to the optimal quality that could be achieved with variable density random undersampling. The number of scans available as prior knowledge had only a minor influence on reconstruction quality. This shows that with at least one fully sampled scan as prior knowledge, suboptimal reconstruction quality can be avoided using data-driven undersampling methods.

In **Chapter 3**, we proposed a fast method for the simulation of off-resonance artifacts in steady-state MRI. By exploiting the repetitive nature of steady-state pulse sequences we demonstrated the possibility of using fast Fourier transforms to simulate phase encoding, and therefore calculate the MR signal with a lower computational complexity than Bloch simulation. We validated simulations of artifacts around metal objects from our proposed method against Bloch simulations and actual MRI scans. The differences in the simulated images resulting from the proposed method were minor with respect to Bloch simulations, while the computational complexity of our fast simulation method was lower by a factor linear with the number of repetitions of the pulse sequence, resulting in a reduction in simulation time with a factor 400 for a 2D simulation with a  $256 \times 256$  matrix size. For 3D simulations, the proposed method is expected to be several orders of magnitude faster,

enabling 3D simulation of off-resonance artifacts at high resolution.

We demonstrated the practical applicability of the fast simulation method by using it to localize metal objects in MRI. With susceptibility models of the metal objects available as prior knowledge, the proposed method can efficiently simulate artifacts around these objects in 3D for many orientations of the objects. By applying phase correlation template matching on an MRI scan with each of these simulations, both the location and orientation of the object can be found. We applied this localization method to scans of a titanium cylinder, an oxidized zirconium knee implant, and gold fiducials, each of which was localized accurately.

In **Chapter 4** we extended the metal object localization methodology from **Chapter 3** and applied it to localization of low dose rate (LDR) brachytherapy seeds in vivo in the prostate. Localization of brachytherapy seeds using only MRI would support an MR-only workflow for postimplant dosimetry, which would remove the need for CT scanning and image registration. However, because in LDR brachytherapy many radioactive seeds are implanted in the prostate in close vicinity to each other, MR-only localization of these seeds is particularly challenging. To address this challenge, we implemented a local matching strategy based on linear regression, in order to ensure that detections found with the template matching methodology from **Chapter 3** were indeed valid detections.

We applied this localization method to MRI scans of 25 prostate cancer patients who underwent LDR brachytherapy and for whom postimplant dosimetry was performed after four weeks. Out of a total of 1557 seeds, 1490 were correctly detected, while 67 false positive errors were made. The correctly detected seed locations had a high spatial accuracy with an average error of 0.8 mm compared with locations found on CT. By classifying the detection errors we found that a majority of the false positive detections occurred near other seeds. Most of the false negative detections were found in either stranded configurations without spacers or near other seeds. These results show that a low detection error rate and high accuracy can be achieved using an MR-only brachytherapy seed localization approach based on template matching of complex-valued artifacts. For MR-only postimplant dosimetry, the most important remaining challenge is to achieve robustness with regard to configuration of multiple seeds in close vicinity.

In **Chapter 5** we combined the metal object localization methodology from **Chapter 3** with radial undersampling and the white marker phenomenon to achieve real-time tracking of passive metal devices in MRI. Using a multi-echo pulse sequence we were able to simultaneously acquire images with anatomical contrast. We tested this approach on tracking of five 0.5 mm steel markers in an agarose phantom and on an insertion of an MRI-compatible 20 Gauge titanium needle in ex vivo porcine tissue.

We performed tracking experiments with both stationary and moving objects. The tracked locations of the stationary steel spheres were compared with locations found using CT. The average pairwise distance between the MRI and CT locations was 0.30 mm, which was close to the theoretical limit of a system that localizes objects on the MRI resolution of 1.2 mm. To evaluate the accuracy of our method on the moving steel spheres, we assumed that the spheres maintained a rigid configuration during movement and measured the error compared with this configuration. On average, we found an error of 0.29 mm which remained relatively constant during motion.

Qualitative evaluation of the tracking of the needle insertions showed that tracked positions were stable throughout needle insertion and retraction. The anatomical contrast around the needle tip was almost undisturbed by off-resonance artifacts caused by the pres-

ence of the needle because of the low echo time and fast acquisition of the anatomical image. Finally, we showed that the tracking algorithm can be applied to dual plane acquisitions, which could be used to support automatic slice positioning to keep the scanning planes centered on the device.

The passive tracking method we proposed shares some advantages that are traditionally only available with active tracking methods: accurate tracking of devices at high framerates, the ability to include real-time anatomical scanning, and the capability of automatic slice positioning. Furthermore, the method does not require specialized hardware and could therefore be applied to track any rigid metal device that is safe for use in MRI and that causes sufficient magnetic field distortions.

## 6.2 Discussion

Current imaging methods rely mostly on the underlying physical principles of the imaging device, generally leaving valuable prior knowledge unused. The major advantage of this approach is the wide applicability: In theory, a scanner would not even need to know what type of anatomy is being imaged. The downside is that with the amount of prior knowledge available today, evidence is increasing that imaging can be enhanced when this knowledge is incorporated in the image formation process. And with the still growing digitization of patient files and databases of scans, a wealth of prior knowledge will continue to become available in the future.

In this thesis we have demonstrated that different types of prior knowledge can be exploited to improve the MR imaging workflow, for example by reducing scan time, by localizing metal objects that are otherwise difficult to discern, and by enabling real-time guidance of interventional procedures using MRI. In **Chapter 2** we have shown that prior knowledge of medical images in general can be used for optimization of undersampling patterns for Compressed Sensing (CS) MRI. In **Chapters 3 to 5** we have shown that prior knowledge of the shape and composition of metal devices can be used for (accelerated) localization of metal objects in MRI. It is important to note that within these applications we have not exhausted the potential of the prior knowledge that was available. In CS, prior knowledge could be used to optimize almost every aspect of the implementation. In particular the sparsifying transform and the reconstruction algorithm could be chosen using prior knowledge. Ideally, these aspects should be optimized simultaneously, because it would be reasonable to expect that, for example, changing the sparsifying transform and its parameters would influence the optimal undersampling pattern and reconstruction parameters, and vice versa. In our studies on localization of metal objects we expect that using additional prior knowledge about the expected configurations of multiple metal objects can be helpful. For example, this can include knowledge about configurations of brachytherapy seeds (**Chapter 4**), the locations of multiple markers on a single rigid device (**Chapter 5**), or constraints on the relative orientations of implants that consist of multiple rigid components, such as a total knee replacement implant. This type of prior knowledge could restrict the solution space of plausible solutions, which could make localization of the objects easier and less computationally intensive.

An important requirement for the further development of an MR acquisition, reconstruction, and analysis workflow that incorporates prior knowledge is that information that can be relevant as prior knowledge should be collected and stored. Currently, mostly clini-

cally relevant information is stored, unless there are specific research questions that require additional information to be stored. For example, for the majority of MRI scans only magnitude images are stored, while the complex-valued images are discarded since they are often not clinically relevant. However, in all studies presented in this thesis the complex-valued images were necessary for the methods to function. For wider application of prior knowledge in MRI it will be necessary to collect and store all information that could be relevant for future MRI exams, even if it is not strictly clinically necessary. There are challenges associated with such large scale data collection that need to be adequately solved, for example concerning infrastructure, security, and privacy of patients.

The way prior knowledge could or should be incorporated in the imaging process is very application-specific. The image-based approach we took in **Chapter 2** is fundamentally different from the model-based and physics-based approaches in **Chapters 3 to 5**. Generalization and application of our methods to fundamentally different problems with different types of prior knowledge will therefore be difficult. However, our research does show that there is merit in using prior knowledge, and can serve as an example of how incorporation of prior knowledge can be approached in a systematic, mathematical fashion. Our results in **Chapter 5** in particular show value in taking an approach where acquisition, reconstruction, and image processing are not seen as separate entities. The knowledge of having a specific clinical objective, in this case tracking of a metal interventional device, inspired modifications in the entire acquisition, reconstruction, and image processing pipeline. In general, we believe that such a holistic approach is necessary to achieve optimal, accelerated MRI exams that are suitable to answer very specific clinical questions. The availability of prior knowledge on different levels of the imaging process could stimulate this type of approach.

The use of prior knowledge should be approached with care, as there are risks involved. For example, an imaging workflow that is taught what to expect in terms of normal and healthy anatomy may become biased towards trying to image normal anatomy, while losing quality or even missing pathology in diseased anatomies. There are approaches that can be taken to minimize this risk. The most rigorous approach is to make sure that a representative sample of diseased anatomies is included in the datasets that are used as prior knowledge. Importantly, the methods that learn from the prior knowledge must ensure that overfitting on healthy anatomies is avoided. Our results in **Chapter 2** show that the optimized undersampling patterns for CS do not overfit even when they are optimized using just data from a single patient. However, this must be confirmed in clinically relevant conditions by imaging patients with diseased anatomies, preferably using unaccelerated scans as a gold standard.

Another risk is that the use of prior knowledge can lead to errors or imaging artifacts that are hard to understand intuitively. While it is possible to educate doctors to recognize such situations, ideally we would want to avoid such artifacts as much as possible. To avoid artifacts, it is important to not push acceleration of MRI to its extreme limits, but rather to take a safer, more reliable approach.

As most medical images exhibit some form of sparsity, Compressed Sensing has the promise of being generally applicable to virtually any MRI scan. A major challenge for CS in clinical practice is to prove that the acceleration it provides does not reduce the diagnostic quality of the reconstructed images. Optimizations based on prior knowledge, such as the methods we evaluated in **Chapter 2**, can improve the overall quality of the reconstructed images. However, diagnostic quality of an image does not necessarily correlate with voxel-

wise quality metrics (e.g., MSE) or metrics for overall image quality (e.g., SSIM), inasmuch as it can depend on very specific features. A variety of datasets of MRI scans of different anatomies should be collected to perform clinical evaluation of the diagnostic quality of the images reconstructed using CS.

In **Chapters 4 and 5** we have shown practical applications of localization of metal devices in MRI. Because the localization methodology is generic, other application areas involving metal devices could easily benefit from our approach, as long as accurate models of the devices are available. For example, localization of gold fiducial markers in MRI could advance methods for MR-only radiotherapy planning [123]. And in orthopedics, localization of larger metal implants could aid diagnosis of symptoms related to the implant procedure or to loosening of the implant during follow up. In addition, the position and orientation of an object obtained by our localization method could serve as prior knowledge for other MRI scans. This could lead to better and faster metal artifact correction methods, as current methods do not use this type of prior knowledge [124].

For future application of prior knowledge in MRI, the recent successes of deep learning in medical image processing [125, 126] could be translatable to the entire MR image reconstruction and analysis pipeline. While deep learning requires a large amount of training data, it shows great potential in picking up automatically complex patterns in very diverse types of data. Recently, deep learning has been applied to attempt to solve MR image reconstruction problems such as Compressed Sensing [127], water-fat separation [128], and even to perform reconstruction without using the fast Fourier transform [129]. An interesting and promising aspect of deep learning is that it incorporates prior knowledge automatically. For example, when deep learning is only trained with data from a single type of anatomy, it is also capable of learning priors about that specific anatomy, e.g. the shape and contrasts that appear in that anatomy, which could aid reconstruction from undersampled acquisitions of that anatomy. Therefore, a complete reconstruction and analysis pipeline based on deep learning could help incorporate prior knowledge into the entire pipeline.

With the studies in this thesis we have shown that using prior knowledge to optimize MRI acquisition, reconstruction, and analysis can accelerate MRI acquisitions and obtain clinically relevant information about the location of metal devices in MRI scans. By doing these optimizations we directly increased the value of the MRI scans. Reductions in scan time can be expected from an optimized implementation of Compressed Sensing (**Chapter 2**). And accurate localization of metal devices in MRI improves the efficiency of an MR-only workflow (**Chapters 4 and 5**) that removes the need for imaging using other modalities. As a result, image registration and image fusion will not be necessary in such procedures, making the workflow less labor-intensive. These advances directly translate into a reduction of cost and patient burden.

## BIBLIOGRAPHY

- [1] OECD, “Magnetic resonance imaging (MRI) exams (indicator).” <http://dx.doi.org/10.1787/1d89353f-en>, 2017.
- [2] D. A. Feinberg, C. M. Mills, J. P. Posin, D. A. Ortendahl, N. M. Hylton, L. E. Crooks, J. C. Watts, L. Kaufman, M. Arakawa, and J. C. Hoenninger, “Multiple spin-echo magnetic resonance imaging,” *Radiology*, vol. 155, pp. 437–442, May 1985.
- [3] J. Hennig, A. Nauerth, and H. Friedburg, “RARE imaging: A fast imaging method for clinical MR,” *Magnetic Resonance in Medicine*, vol. 3, pp. 823–833, Dec. 1986.
- [4] M. K. Stehling, R. Turner, and P. Mansfield, “Echo-planar imaging: magnetic resonance imaging in a fraction of a second,” *Science*, vol. 254, pp. 43–50, Oct. 1991.
- [5] D. J. Larkman, J. V. Hajnal, A. H. Herlihy, G. A. Coutts, I. R. Young, and G. Ehnholm, “Use of multicoil arrays for separation of signal from multiple slices simultaneously excited,” *Journal of Magnetic Resonance Imaging*, vol. 13, pp. 313–317, Feb. 2001.
- [6] G. McGibney, M. R. Smith, S. T. Nichols, and A. Crawley, “Quantitative evaluation of several partial fourier reconstruction algorithms used in mri,” *Magnetic Resonance in Medicine*, vol. 30, pp. 51–59, July 1993.
- [7] K. P. Pruessmann, M. Weiger, M. B. Scheidegger, and P. Boesiger, “SENSE: Sensitivity encoding for fast MRI,” *Magnetic Resonance in Medicine*, vol. 42, pp. 952–962, Nov. 1999.
- [8] M. A. Griswold, P. M. Jakob, R. M. Heidemann, M. Nittka, V. Jellus, J. Wang, B. Kiefer, and A. Haase, “Generalized autocalibrating partially parallel acquisitions (GRAPPA),” *Magnetic Resonance in Medicine*, vol. 47, pp. 1202–1210, June 2002.
- [9] M. Blaimer, F. Breuer, M. Mueller, R. M. Heidemann, M. A. Griswold, and P. M. Jakob, “SMASH, SENSE, PILS, GRAPPA: how to choose the optimal method,” *Topics in magnetic resonance imaging: TMRI*, vol. 15, pp. 223–236, Aug. 2004.
- [10] M. Lustig, D. Donoho, and J. M. Pauly, “Sparse MRI: The application of compressed sensing for rapid MR imaging,” *Magnetic Resonance in Medicine*, vol. 58, pp. 1182–1195, Dec. 2007.
- [11] D. S. Taubman and M. W. Marcellin, *JPEG 2000: Image Compression Fundamentals, Standards and Practice*. Norwell, MA, USA: Kluwer Academic Publishers, 2001.
- [12] M. Lustig and J. M. Pauly, “SPIRiT: Iterative self-consistent parallel imaging reconstruction from arbitrary k-space,” *Magnetic Resonance in Medicine*, vol. 64, pp. 457–471, Aug. 2010.
- [13] S. Vasanawala, M. Murphy, M. Alley, P. Lai, K. Keutzer, J. Pauly, and M. Lustig, “Practical parallel imaging compressed sensing MRI: Summary of two years of experience in accelerating body MRI of pediatric patients,” in *2011 IEEE International Symposium on Biomedical Imaging: From Nano to Macro*, pp. 1039–1043, Mar. 2011.
- [14] S. C. L. Deoni, T. M. Peters, and B. K. Rutt, “High-resolution T1 and T2 mapping of the brain in a clinically acceptable time with DESPOT1 and DESPOT2,” *Magnetic Resonance in Medicine*, vol. 53, pp. 237–241, Jan. 2005.

- [15] L. de Rochefort, R. Brown, M. R. Prince, and Y. Wang, "Quantitative MR susceptibility mapping using piece-wise constant regularized inversion of the magnetic field," *Magnetic Resonance in Medicine*, vol. 60, pp. 1003–1009, Oct. 2008.
- [16] U. Gamper, P. Boesiger, and S. Kozerke, "Compressed sensing in dynamic MRI," *Magnetic Resonance in Medicine*, vol. 59, pp. 365–373, Feb. 2008.
- [17] B. Bilgic, V. K. Goyal, and E. Adalsteinsson, "Multi-contrast reconstruction with Bayesian compressed sensing," *Magnetic Resonance in Medicine*, vol. 66, pp. 1601–1615, Dec. 2011.
- [18] M. Doneva, P. Börnert, H. Eggers, C. Stehning, J. S en egas, and A. Mertins, "Compressed sensing reconstruction for magnetic resonance parameter mapping," *Magnetic Resonance in Medicine*, vol. 64, pp. 1114–1120, Oct. 2010.
- [19] M. Cabezas, A. Oliver, X. Llad o, J. Freixenet, and M. Bach Cuadra, "A review of atlas-based segmentation for magnetic resonance brain images," *Computer Methods and Programs in Biomedicine*, vol. 104, pp. e158–e177, Dec. 2011.
- [20] T. Heimann and H.-P. Meinzer, "Statistical shape models for 3d medical image segmentation: A review," *Medical Image Analysis*, vol. 13, pp. 543–563, Aug. 2009.
- [21] D. L. Pham, C. Xu, and J. L. Prince, "Current Methods in Medical Image Segmentation," *Annual Review of Biomedical Engineering*, vol. 2, no. 1, pp. 315–337, 2000.
- [22] J. G. Bouwman and C. J. G. Bakker, "Alias subtraction more efficient than conventional zero-padding in the Fourier-based calculation of the susceptibility induced perturbation of the magnetic field in MR," *Magnetic Resonance in Medicine*, vol. 68, pp. 621–630, Aug. 2012.
- [23] J. D. Port and M. G. Pomper, "Quantification and minimization of magnetic susceptibility artifacts on GRE images," *Journal of Computer Assisted Tomography*, vol. 24, pp. 958–964, Dec. 2000.
- [24] Z. H. Cho, D. J. Kim, and Y. K. Kim, "Total inhomogeneity correction including chemical shifts and susceptibility by view angle tilting," *Medical Physics*, vol. 15, pp. 7–11, Jan. 1988.
- [25] K. M. Koch, J. E. Lorbiecki, R. S. Hinks, and K. F. King, "A multispectral three-dimensional acquisition technique for imaging near metal implants," *Magnetic Resonance in Medicine*, vol. 61, pp. 381–390, Feb. 2009.
- [26] W. Lu, K. B. Pauly, G. E. Gold, J. M. Pauly, and B. A. Hargreaves, "SEMAC: Slice Encoding for Metal Artifact Correction in MRI," *Magnetic Resonance in Medicine*, vol. 62, pp. 66–76, July 2009.
- [27] S. Ghose, J. Mitra, D. Rivest-H enault, A. Fazlollahi, P. Stanwell, P. Pichler, J. Sun, J. Fripp, P. B. Greer, and J. A. Dowling, "MRI-alone radiation therapy planning for prostate cancer: Automatic fiducial marker detection," *Medical Physics*, vol. 43, pp. 2218–2228, May 2016.
- [28] K. Wachowicz, S. D. Thomas, and B. G. Fallone, "Characterization of the susceptibility artifact around a prostate brachytherapy seed in MRI," *Medical Physics*, vol. 33, pp. 4459–4467, Dec. 2006.
- [29] C. J. Bakker, R. M. Hoogeveen, W. F. Hurtak, J. J. van Vaals, M. A. Viergever, and W. P. Mali, "MR-guided endovascular interventions: susceptibility-based catheter and near-real-time imaging technique.," *Radiology*, vol. 202, pp. 273–276, Jan. 1997.
- [30] S. S. Vasanawala, M. T. Alley, B. A. Hargreaves, R. A. Barth, J. M. Pauly, and M. Lustig, "Improved Pediatric MR Imaging with Compressed Sensing," *Radiology*, vol. 256, pp. 607–616, Aug. 2010.
- [31] J. Paulsen, V. S. Bajaj, and A. Pines, "Compressed sensing of remotely detected MRI velocimetry in microfluidics," *Journal of Magnetic Resonance*, vol. 205, pp. 196–201, Aug. 2010.
- [32] E. J. Cand es, Y. C. Eldar, D. Needell, and P. Randall, "Compressed sensing with coherent and redundant dictionaries," *Applied and Computational Harmonic Analysis*, vol. 31, pp. 59–73, July 2011.
- [33] E. Cand es, L. Demanet, D. Donoho, and L. Ying, "Fast Discrete Curvelet Transforms," *Multiscale Modeling & Simulation*, vol. 5, pp. 861–899, Jan. 2006.

- [34] A. Beck and M. Teboulle, "A Fast Iterative Shrinkage-Thresholding Algorithm for Linear Inverse Problems," *SIAM Journal on Imaging Sciences*, vol. 2, pp. 183–202, Jan. 2009.
- [35] E. J. Candès and T. Tao, "Near-optimal signal recovery from random projections: Universal encoding strategies?," *Information Theory, IEEE Transactions on*, vol. 52, no. 12, pp. 5406–5425, 2006.
- [36] S. Ajraoui, K. J. Lee, M. H. Deppe, S. R. Parnell, J. Parra-Robles, and J. M. Wild, "Compressed sensing in hyperpolarized  $^3\text{He}$  Lung MRI," *Magnetic Resonance in Medicine*, vol. 63, pp. 1059–1069, Apr. 2010.
- [37] X. Qu, W. Zhang, D. Guo, C. Cai, S. Cai, and Z. Chen, "Iterative thresholding compressed sensing MRI based on contourlet transform," *Inverse Problems in Science and Engineering*, vol. 18, pp. 737–758, Sept. 2010.
- [38] S. D. Sharma, C. L. Fong, B. S. Tzung, M. Law, and K. S. Nayak, "Clinical Image Quality Assessment of Accelerated Magnetic Resonance Neuroimaging Using Compressed Sensing:," *Investigative Radiology*, vol. 48, pp. 638–645, Sept. 2013.
- [39] S. Hu, M. Lustig, A. Balakrishnan, P. E. Z. Larson, R. Bok, J. Kurhanewicz, S. J. Nelson, A. Goga, J. M. Pauly, and D. B. Vigneron, "3d compressed sensing for highly accelerated hyperpolarized  $^{13}\text{C}$  MRSI with in vivo applications to transgenic mouse models of cancer," *Magnetic Resonance in Medicine*, vol. 63, pp. 312–321, Feb. 2010.
- [40] F. Knoll, C. Clason, C. Diwokoy, and R. Stollberger, "Adapted random sampling patterns for accelerated MRI," *Magnetic Resonance Materials in Physics, Biology and Medicine*, vol. 24, pp. 43–50, Jan. 2011.
- [41] D.-d. Liu, D. Liang, X. Liu, and Y.-t. Zhang, "Under-sampling trajectory design for compressed sensing MRI," in *Engineering in Medicine and Biology Society (EMBC), 2012 Annual International Conference of the IEEE*, pp. 73–76, IEEE, 2012.
- [42] S. Ravishanker and Y. Bresler, "Adaptive sampling design for compressed sensing MRI," in *Engineering in Medicine and Biology Society, EMBC, 2011 Annual International Conference of the IEEE*, pp. 3751–3755, IEEE, 2011.
- [43] M. Seeger, H. Nickisch, R. Pohmann, and B. Schölkopf, "Optimization of k-space trajectories for compressed sensing by Bayesian experimental design," *Magnetic Resonance in Medicine*, vol. 63, pp. 116–126, Jan. 2010.
- [44] K. Epperson, A. M. Sawyer, M. Lustig, M. Alley, M. Uecker, P. Virtue, P. Lai, and S. Vasanawala, "Creation of an MRI Data Repository for Validating Compressed Sensing and Other Acceleration Techniques," in *SMRT Conference, Salt Lake City, UT*, 2013.
- [45] K. Epperson, "MR Datasets for Compressed Sensing." <http://mridata.org/>, 2013.
- [46] C. A. McKenzie, E. N. Yeh, M. A. Ohliger, M. D. Price, and D. K. Sodickson, "Self-calibrating parallel imaging with automatic coil sensitivity extraction," *Magnetic Resonance in Medicine*, vol. 47, no. 3, pp. 529–538, 2002.
- [47] M. Uecker, P. Virtue, F. Ong, M. J. Murphy, M. T. Alley, S. S. Vasanawala, and M. Lustig, "Software toolbox and programming library for compressed sensing and parallel imaging," in *Proceedings of the ISMRM Workshop on Data Sampling and Reconstruction, Sedona, Arizona, USA*, 2013.
- [48] J. J. M. Zwanenburg, M. J. Versluis, P. R. Luijten, and N. Petridou, "Fast high resolution whole brain  $T_2^*$  weighted imaging using echo planar imaging at 7 T," *NeuroImage*, vol. 56, pp. 1902–1907, June 2011.
- [49] I. Daubechies, "The wavelet transform, time-frequency localization and signal analysis," *Information Theory, IEEE Transactions on*, vol. 36, no. 5, pp. 961–1005, 1990.
- [50] T. Goldstein and S. Osher, "The Split Bregman Method for L1-Regularized Problems," *SIAM Journal on Imaging Sciences*, vol. 2, pp. 323–343, Jan. 2009.

- [51] M. Uecker, P. Lai, M. J. Murphy, P. Virtue, M. Elad, J. M. Pauly, S. S. Vasanawala, and M. Lustig, "ESPIRiT—an eigenvalue approach to autocalibrating parallel MRI: Where SENSE meets GRAPPA," *Magnetic Resonance in Medicine*, vol. 71, pp. 990–1001, Mar. 2014.
- [52] M. Uecker, F. Ong, J. I. Tamir, D. Bahri, P. Virtue, J. Y. Cheng, T. Zhang, and M. Lustig, "Berkeley Advanced Reconstruction Toolbox," in *Proc. Intl. Soc. Mag. Reson. Med.*, (Toronto), p. 23:2486, 2015.
- [53] M. Uecker, F. Ong, J. I. Tamir, D. Bahri, P. Virtue, J. Y. Cheng, T. Zhang, and M. Lustig, "Berkeley Advanced Reconstruction Toolbox." <http://mikgroup.github.io/bart/>, 2015.
- [54] D. J. Best and D. E. Roberts, "Algorithm AS 89: The Upper Tail Probabilities of Spearman's Rho," *Journal of the Royal Statistical Society. Series C (Applied Statistics)*, vol. 24, pp. 377–379, Jan. 1975.
- [55] Z. Wang, A. Bovik, H. Sheikh, and E. Simoncelli, "Image quality assessment: from error visibility to structural similarity," *IEEE Transactions on Image Processing*, vol. 13, pp. 600–612, Apr. 2004.
- [56] S. Klein, M. Staring, K. Murphy, M. Viergever, and J. Pluim, "elastix: A Toolbox for Intensity-Based Medical Image Registration," *IEEE Transactions on Medical Imaging*, vol. 29, pp. 196–205, Jan. 2010.
- [57] S. Rapacchi, Y. Natsuaki, A. Plotnik, S. Gabriel, G. Laub, J. P. Finn, and P. Hu, "Reducing view-sharing using compressed sensing in time-resolved contrast-enhanced magnetic resonance angiography," *Magnetic Resonance in Medicine*, vol. 74, pp. 474–481, Aug. 2015.
- [58] N. Gdaniec, H. Eggers, P. Börner, M. Doneva, and A. Mertins, "Robust abdominal imaging with incomplete breath-holds," *Magnetic Resonance in Medicine*, vol. 71, pp. 1733–1742, May 2014.
- [59] K. M. Lüdeke, P. Röschmann, and R. Tischler, "Susceptibility artefacts in NMR imaging," *Magnetic Resonance Imaging*, vol. 3, no. 4, pp. 329–343, 1985.
- [60] C. J. G. Bakker, R. Bhagwandien, M. A. Moerland, and L. M. P. Ramos, "Simulation of susceptibility artifacts in 2d and 3d fourier transform spin-echo and gradient-echo magnetic resonance imaging," *Magnetic Resonance Imaging*, vol. 12, no. 5, pp. 767–774, 1994.
- [61] H. Liu, A. J. Martin, and C. L. Truwit, "Interventional MRI at high-field (1.5 T): Needle artifacts," *Journal of Magnetic Resonance Imaging*, vol. 8, pp. 214–219, Jan. 1998.
- [62] K. Koch, B. Hargreaves, K. B. Pauly, W. Chen, G. Gold, and K. King, "Magnetic resonance imaging near metal implants," *Journal of Magnetic Resonance Imaging*, vol. 32, pp. 773–787, Oct. 2010.
- [63] B. A. Hargreaves, P. W. Worters, K. B. Pauly, J. M. Pauly, K. M. Koch, and G. E. Gold, "Metal-Induced Artifacts in MRI," *American Journal of Roentgenology*, vol. 197, pp. 547–555, Sept. 2011.
- [64] M. R. Smith, N. S. Artz, C. Wiens, D. Hernando, and S. B. Reeder, "Characterizing the limits of MRI near metallic prostheses," *Magnetic Resonance in Medicine*, vol. 74, pp. 1564–1573, Dec. 2015.
- [65] V. Lagerburg, M. A. Moerland, J. H. Seppenwoolde, and J. J. W. Lagendijk, "Simulation of the artefact of an iodine seed placed at the needle tip in MRI-guided prostate brachytherapy," *Physics in Medicine and Biology*, vol. 53, no. 5, p. N59, 2008.
- [66] Y. Dong, Z. Chang, G. Xie, G. Whitehead, and J. X. Ji, "Susceptibility-based positive contrast MRI of brachytherapy seeds," *Magnetic Resonance in Medicine*, vol. 74, pp. 716–726, Sept. 2015.
- [67] P. Shkarin and R. G. S. Spencer, "Direct simulation of spin echoes by summation of isochromats," *Concepts in Magnetic Resonance*, vol. 8, pp. 253–268, Jan. 1996.
- [68] H. Benoit-Cattin, G. Collewet, B. Belaroussi, H. Saint-Jalmes, and C. Odet, "The SIMRI project: a versatile and interactive MRI simulator," *Journal of Magnetic Resonance*, vol. 173, pp. 97–115, Mar. 2005.
- [69] T. Stöcker, K. Vahedipour, D. Pflugfelder, and N. J. Shah, "High-performance computing MRI simulations," *Magnetic Resonance in Medicine*, vol. 64, pp. 186–193, July 2010.

- [70] C. G. Xanthis, I. E. Venetis, A. V. Chalkias, and A. H. Aletras, "MRISIMUL: A GPU-Based Parallel Approach to MRI Simulations," *IEEE Transactions on Medical Imaging*, vol. 33, pp. 607–617, Mar. 2014.
- [71] F. Zijlstra, J. G. Bouwman, I. Braškute, and P. R. Seevinck, "Fast simulation of off-resonance artifacts in MRI using FORECAST (Fourier-based Off-REsonanCe Artifact Simulation in the Steady-State)," in *Proceedings of the 24th Annual Meeting of the ISMRM*, (Singapore), 2016.
- [72] C. Kuglin and D. Hines, "The Phase Correlation Image Alignment Method," in *Proc. of the IEEE Int. Conf. on Cybernetics and Society*, pp. 163–165, 1975.
- [73] J. A. Fessler and B. P. Sutton, "Nonuniform fast Fourier transforms using min-max interpolation," *IEEE Transactions on Signal Processing*, vol. 51, pp. 560–574, Feb. 2003.
- [74] S. D. Sharma, N. S. Artz, D. Hernando, D. E. Horng, and S. B. Reeder, "Improving chemical shift encoded water-fat separation using object-based information of the magnetic field inhomogeneity," *Magnetic Resonance in Medicine*, vol. 73, pp. 597–604, Feb. 2015.
- [75] K. M. Koch, M. F. Koff, P. Shah, and H. G. Potter, "A Mechanism for Quantifiable MRI-Based Detection of Cobalt-Chromium Particulate Deposits Near Total Hip Replacements," in *Proceedings of the 23rd Annual Meeting of the ISMRM*, (Toronto), 2015.
- [76] F. Zijlstra, J. G. Bouwman, M. A. Moerland, and P. R. Seevinck, "Fully automatic in-vivo localization of LDR brachytherapy seeds for post-implant dosimetry using MR simulations and template matching," in *Proceedings of the 24th Annual Meeting of the ISMRM*, (Singapore), 2016.
- [77] E. Beld, M. Moerland, F. Zijlstra, J. Lagendijk, M. Viergever, and P. Seevinck, "Automatic High Temporal and Spatial Resolution Position Verification of an HDR Brachytherapy Source Using Subpixel Localization and SENSE," in *Proceedings of the 24th Annual Meeting of the ISMRM*, (Singapore), 2016.
- [78] S. Nag, J. P. Ciezki, R. Cormack, S. Doggett, K. DeWyngaert, G. K. Edmundson, R. G. Stock, N. N. Stone, Y. Yu, and M. J. Zelefsky, "Intraoperative planning and evaluation of permanent prostate brachytherapy: Report of the American Brachytherapy Society," *International Journal of Radiation Oncology\*Biophysics*, vol. 51, pp. 1422–1430, Dec. 2001.
- [79] M. J. Rivard, D.-A. R. Evans, and I. Kay, "A technical evaluation of the Nucletron FIRST system: Conformance of a remote afterloading brachytherapy seed implantation system to manufacturer specifications and AAPM Task Group report recommendations," *Journal of Applied Clinical Medical Physics*, vol. 6, pp. 22–50, Dec. 2005.
- [80] D.-A. Radford Evans, T. Meyer, S. Angyalfi, S. Husain, I. Kay, and P. Dunscombe, "Enhanced efficiency and ergonomics of an intraoperative automated prostate brachytherapy delivery technique," *Brachytherapy*, vol. 6, pp. 254–257, Oct. 2007.
- [81] R. Taschereau, J. Pouliot, J. Roy, and D. Tremblay, "Seed misplacement and stabilizing needles in transperineal permanent prostate implants," *Radiotherapy and Oncology*, vol. 55, pp. 59–63, Apr. 2000.
- [82] D. R. Reed, K. E. Wallner, G. S. Merrick, S. Arthurs, A. Mueller, W. Cavanagh, W. B. Butler, E. Ford, and S. G. Sutlief, "A prospective randomized comparison of stranded vs. loose 125i seeds for prostate brachytherapy," *Brachytherapy*, vol. 6, pp. 129–134, Apr. 2007.
- [83] D. Ash, A. Flynn, J. Battermann, T. de Reijke, P. Lavagnini, and L. Blank, "ESTRO/EAU/EORTC recommendations on permanent seed implantation for localized prostate cancer," *Radiotherapy and Oncology*, vol. 57, pp. 315–321, Dec. 2000.
- [84] C. Salembier, P. Lavagnini, P. Nickers, P. Mangili, A. Rijnders, A. Polo, J. Venselaar, and P. Hoskin, "Tumour and target volumes in permanent prostate brachytherapy: A supplement to the ESTRO/EAU/EORTC recommendations on prostate brachytherapy," *Radiotherapy and Oncology*, vol. 83, pp. 3–10, Apr. 2007.

- [85] J. O. Barentsz, J. Richenberg, R. Clements, P. Choyke, S. Verma, G. Villeirs, O. Rouviere, V. Loggager, and J. J. Fütterer, "ESUR prostate MR guidelines 2012," *European Radiology*, vol. 22, pp. 746–757, Apr. 2012.
- [86] C. Lim, S. C. Malone, L. Avruch, R. H. Breau, T. A. Flood, M. Lim, C. Morash, J. S. Quon, C. Walsh, and N. Schieda, "Pictorial review. Magnetic resonance for radiotherapy management and treatment planning in prostatic carcinoma," *The British Journal of Radiology*, vol. 88, p. 20150507, Oct. 2015.
- [87] A. P. Brown, T. J. Pugh, D. A. Swanson, R. J. Kudchadker, T. L. Bruno, E. N. Christensen, M. van Vulpen, and S. J. Frank, "Improving prostate brachytherapy quality assurance with MRI-CT fusion-based sector analysis in a phase II prospective trial of men with intermediate-risk prostate cancer," *Brachytherapy*, vol. 12, pp. 401–407, Sept. 2013.
- [88] M. De Brabandere, B. Al-Qaisieh, L. De Wever, K. Haustermans, C. Kirisits, M. A. Moerland, R. Oyen, A. Rijnders, F. Van den Heuvel, and F.-A. Siebert, "CT- and MRI-based seed localization in postimplant evaluation after prostate brachytherapy," *Brachytherapy*, vol. 12, pp. 580–588, Nov. 2013.
- [89] K. Tanderup, A. Viswanathan, C. Kirisits, and S. J. Frank, "MRI-guided brachytherapy," *Seminars in radiation oncology*, vol. 24, pp. 181–191, July 2014.
- [90] M. De Brabandere, C. Kirisits, R. Peeters, K. Haustermans, and F. Van den Heuvel, "Accuracy of seed reconstruction in prostate postplanning studied with a CT- and MRI-compatible phantom," *Radiotherapy and Oncology*, vol. 79, pp. 190–197, May 2006.
- [91] S. D. Thomas, K. Wachowicz, and B. G. Fallone, "MRI of prostate brachytherapy seeds at high field: A study in phantom," *Medical Physics*, vol. 36, pp. 5228–5234, Nov. 2009.
- [92] A. K. H. Robertson, P. S. Basran, S. D. Thomas, and D. Wells, "CT, MR, and ultrasound image artifacts from prostate brachytherapy seed implants: The impact of seed size," *Medical Physics*, vol. 39, pp. 2061–2068, Apr. 2012.
- [93] N. Kuo, J. Lee, C. Tempny, M. Stuber, and J. Prince, "MRI-based prostate brachytherapy seed localization," *Proceedings / IEEE International Symposium on Biomedical Imaging: from nano to macro. IEEE International Symposium on Biomedical Imaging*, vol. 2010, pp. 1397–1400, Apr. 2010.
- [94] P. R. Seevinck, H. de Leeuw, C. Bos, and C. J. G. Bakker, "Highly localized positive contrast of small paramagnetic objects using 3d center-out radial sampling with off-resonance reception," *Magnetic Resonance in Medicine*, vol. 65, pp. 146–156, Jan. 2011.
- [95] F. Zijlstra, J. G. Bouwman, I. Braškute, M. A. Viergever, and P. R. Seevinck, "Fast Fourier-based simulation of off-resonance artifacts in steady-state gradient echo MRI applied to metal object localization," *Magnetic Resonance in Medicine*, Dec. 2016.
- [96] A. Myronenko and X. Song, "Point Set Registration: Coherent Point Drift," *IEEE Transactions on Pattern Analysis and Machine Intelligence*, vol. 32, pp. 2262–2275, Dec. 2010.
- [97] L. R. Dice, "Measures of the Amount of Ecologic Association Between Species," *Ecology*, vol. 26, pp. 297–302, July 1945.
- [98] N. Chng, I. Spadinger, W. J. Morris, N. Usmani, and S. Salcudean, "Prostate brachytherapy postimplant dosimetry: Automatic plan reconstruction of stranded implants," *Medical Physics*, vol. 38, pp. 327–342, Jan. 2011.
- [99] S. J. Frank, R. J. Stafford, J. A. Bankson, C. Li, D. A. Swanson, R. J. Kudchadker, and K. S. Martirosyan, "A Novel MRI Marker for Prostate Brachytherapy," *International Journal of Radiation Oncology\* Biology\* Physics*, vol. 71, pp. 5–8, May 2008.
- [100] A. Alba, J. F. Viguera-Gomez, E. R. Arce-Santana, and R. M. Aguilar-Ponce, "Phase correlation with sub-pixel accuracy: A comparative study in 1d and 2d," *Computer Vision and Image Understanding*, vol. 137, pp. 76–87, Aug. 2015.

- [101] C.-A. Collins Fekete, M. Plamondon, A.-G. Martin, E. Vigneault, F. Verhaegen, and L. Beaulieu, "Quantifying the effect of seed orientation in postplanning dosimetry of low-dose-rate prostate brachytherapy," *Medical Physics*, vol. 41, p. 101704, Oct. 2014.
- [102] A. J. Krafft, P. Zamecnik, F. Maier, A. de Oliveira, P. Hallscheidt, H.-P. Schlemmer, and M. Bock, "Passive marker tracking via phase-only cross correlation (POCC) for MR-guided needle interventions: Initial in vivo experience," *Physica Medica*, vol. 29, pp. 607–614, Nov. 2013.
- [103] J. N. Draper, M. L. Lauzon, and R. Frayne, "Passive catheter visualization in magnetic resonance-guided endovascular therapy using multicycle projection dephasers," *Journal of Magnetic Resonance Imaging*, vol. 24, pp. 160–167, July 2006.
- [104] J.-H. Seppenwoolde, L. W. Bartels, R. van der Weide, J. F. Nijsen, A. D. van het Schip, and C. J. Bakker, "Fully MR-guided hepatic artery catheterization for selective drug delivery: A feasibility study in pigs," *Journal of Magnetic Resonance Imaging*, vol. 23, pp. 123–129, Feb. 2006.
- [105] H. Karimi, W. Dominguez-Viqueira, and C. H. Cunningham, "Position and orientation measurement of susceptibility markers using spectrally selective spin-echo projections," *Magnetic Resonance in Medicine*, vol. 76, pp. 1563–1573, Nov. 2016.
- [106] T. Kapur, J. Egger, A. Damato, E. J. Schmidt, and A. N. Viswanathan, "3-T MR-guided brachytherapy for gynecologic malignancies," *Magnetic Resonance Imaging*, vol. 30, pp. 1279–1290, Nov. 2012.
- [107] W. Wang, C. L. Dumoulin, A. N. Viswanathan, Z. T. H. Tse, A. Mehrtash, W. Loew, I. Norton, J. Tokuda, R. T. Seethamraju, T. Kapur, A. L. Damato, R. A. Cormack, and E. J. Schmidt, "Real-time active MR-tracking of metallic stylets in MR-guided radiation therapy," *Magnetic resonance in medicine : official journal of the Society of Magnetic Resonance in Medicine / Society of Magnetic Resonance in Medicine*, vol. 73, pp. 1803–1811, May 2015.
- [108] J. L. Duerk, E. Y. Wong, and J. S. Lewin, "A brief review of hardware for catheter tracking in magnetic resonance imaging," *Magnetic Resonance Materials in Physics, Biology and Medicine*, vol. 13, p. 199, Oct. 2001.
- [109] K. Zhang, F. Maier, A. J. Krafft, R. Umathum, W. Semmler, and M. Bock, "Tracking of an interventional catheter with a ferromagnetic tip using dual-echo projections," *Journal of Magnetic Resonance*, vol. 234, pp. 176–183, Sept. 2013.
- [110] P. S. Larson, P. A. Starr, G. Bates, L. Tansey, R. M. Richardson, and A. J. Martin, "An Optimized System for Interventional MRI Guided Stereotactic Surgery: Preliminary Evaluation of Targeting Accuracy," *Neurosurgery*, vol. 70, pp. 95–103, Mar. 2012.
- [111] S. Patil, O. Bieri, P. Jhooti, and K. Scheffler, "Automatic slice positioning (ASP) for passive real-time tracking of interventional devices using projection-reconstruction imaging with echo-dephasing (PRIDE)," *Magnetic Resonance in Medicine*, vol. 62, pp. 935–942, Oct. 2009.
- [112] A. Buecker, G. B. Adam, J. M. Neuerburg, S. Kinzel, A. Glowinski, T. Schaeffter, V. Rasche, J. J. van Vaals, and R. W. Guenther, "Simultaneous real-time visualization of the catheter tip and vascular anatomy for MR-guided PTA of iliac arteries in an animal model," *Journal of Magnetic Resonance Imaging*, vol. 16, pp. 201–208, Aug. 2002.
- [113] T. Kuehne, S. Weiss, F. Brinkert, J. Weil, S. Yilmaz, B. Schmitt, P. Ewert, P. Lange, and M. Gutberlet, "Catheter Visualization with Resonant Markers at MR Imaging?guided Deployment of Endovascular Stents in Swine," *Radiology*, vol. 233, pp. 774–780, Dec. 2004.
- [114] T. Wech, S. M. Shea, J. Barbot, K. Vij, L. Pan, C. H. Lorenz, and S. Patil, "Measurement accuracy of different active tracking sequences for interventional MRI," *Journal of Magnetic Resonance Imaging*, vol. 40, pp. 490–495, Aug. 2014.
- [115] C. E. Saikus, K. Ratnayaka, I. M. Barbash, J. H. Colyer, O. Kocaturk, A. Z. Faranesh, and R. J. Lederman, "MRI-guided vascular access with an active visualization needle," *Journal of Magnetic Resonance Imaging*, vol. 34, pp. 1159–1166, Nov. 2011.

- [116] M. K. Konings, L. W. Bartels, H. F. Smits, and C. J. Bakker, "Heating Around Intravascular Guidewires by Resonating RF Waves," *Journal of Magnetic Resonance Imaging*, vol. 12, pp. 79–85, July 2000.
- [117] C. J. Bakker, J.-H. Seppenwoolde, and K. L. Vincken, "Dephased MRI," *Magnetic Resonance in Medicine*, vol. 55, pp. 92–97, Jan. 2006.
- [118] J.-H. Seppenwoolde, M. A. Viergever, and C. J. Bakker, "Passive tracking exploiting local signal conservation: The white marker phenomenon," *Magnetic Resonance in Medicine*, vol. 50, pp. 784–790, Oct. 2003.
- [119] R. W. Chan, E. A. Ramsay, E. Y. Cheung, and D. B. Plewes, "The influence of radial undersampling schemes on compressed sensing reconstruction in breast MRI," *Magnetic Resonance in Medicine*, vol. 67, pp. 363–377, Feb. 2012.
- [120] M. Lustig, D. L. Donoho, J. M. Santos, and J. M. Pauly, "Compressed Sensing MRI," *IEEE Signal Processing Magazine*, vol. 25, pp. 72–82, Mar. 2008.
- [121] R. E. Kalman, "A New Approach to Linear Filtering and Prediction Problems," *Journal of Basic Engineering*, vol. 82, pp. 35–45, Mar. 1960.
- [122] H. W. Kuhn, "The Hungarian method for the assignment problem," *Naval Research Logistics Quarterly*, vol. 2, pp. 83–97, Mar. 1955.
- [123] M. Maspero, C. A. van den Berg, F. Zijlstra, G. G. Sikkes, H. C. de Boer, G. J. Meijer, L. G. Kerkmeijer, M. A. Viergever, J. J. Lagendijk, and P. R. Seevinck, "Evaluation of an automatic MR-based gold fiducial marker localisation method for MR-only prostate radiotherapy," *Physics in Medicine and Biology*, 2017, under review.
- [124] X. Shi, D. Yoon, K. M. Koch, and B. A. Hargreaves, "Metallic implant geometry and susceptibility estimation using multispectral B0 field maps," *Magnetic Resonance in Medicine*, vol. 77, pp. 2402–2413, June 2017.
- [125] G. Litjens, T. Kooi, B. E. Bejnordi, A. A. A. Setio, F. Ciompi, M. Ghafoorian, J. A. W. M. van der Laak, B. van Ginneken, and C. I. Sánchez, "A Survey on Deep Learning in Medical Image Analysis," *arXiv:1702.05747 [cs]*, Feb. 2017. arXiv: 1702.05747.
- [126] P. Moeskops, J. M. Wolterink, B. H. M. v. d. Velden, K. G. A. Gilhuijs, T. Leiner, M. A. Viergever, and I. Išgum, "Deep Learning for Multi-task Medical Image Segmentation in Multiple Modalities," in *Medical Image Computing and Computer-Assisted Intervention - MICCAI 2016*, Lecture Notes in Computer Science, pp. 478–486, Springer, Cham, Oct. 2016.
- [127] D. Lee, J. Yoo, and J. C. Ye, "Deep residual learning for compressed sensing MRI," in *2017 IEEE 14th International Symposium on Biomedical Imaging (ISBI 2017)*, pp. 15–18, Apr. 2017.
- [128] E. Gong, G. Zaharchuk, and J. Pauly, "Improved multi-echo water-fat separation using deep learning," in *Proceedings of the 25th Annual Meeting of the ISMRM*, no. 5657, (Hawaii), 2017.
- [129] B. Zhu, J. Z. Liu, B. R. Rosen, and M. S. Rosen, "Neural network MR image reconstruction with AUTOMAP: Automated transform by manifold approximation," in *Proceedings of the 25th Annual Meeting of the ISMRM*, no. 0640, (Hawaii), 2017.

# LIST OF PUBLICATIONS

## Publications in international journals

- **F. Zijlstra**, M. A. Viergever, and P. R. Seevinck, “Simultaneous real-time anatomical imaging and passive device tracking using multi-echo undersampled radial acquisitions for MR-guided interventions,” 2017, in preparation.
- M. Maspero, C. A. van den Berg, **F. Zijlstra**, G. G. Sikkes, H. C. de Boer, G. J. Meijer, L. G. Kerkmeijer, M. A. Viergever, J. J. Lagendijk, and P. R. Seevinck, “Evaluation of an automatic MR-based gold fiducial marker localisation method for MR-only prostate radiotherapy,” *Physics in Medicine and Biology*, 2017, in press.
- **F. Zijlstra**, M. A. Moerland, J. R. van der Voort van Zyp, J. L. Noteboom, M. A. Viergever, and P. R. Seevinck, “Challenges in MR-only seed localization for postimplant dosimetry in permanent prostate brachytherapy,” *Medical Physics*, 2017, in press.
- **F. Zijlstra**, J. G. Bouwman, I. Braškute, M. A. Viergever, and P. R. Seevinck, “Fast Fourier-based simulation of off-resonance artifacts in steady-state gradient echo MRI applied to metal object localization,” *Magnetic Resonance in Medicine*, Dec. 2016, early view online.
- **F. Zijlstra**, M. A. Viergever, and P. R. Seevinck, “Evaluation of Variable Density and Data-Driven K-Space Undersampling for Compressed Sensing Magnetic Resonance Imaging,” *Investigative Radiology*, vol. 51, pp. 410–419, June 2016.
- J. S. van Gorp, C. J. G. Bakker, J. G. Bouwman, J. Smink, **F. Zijlstra**, and P. R. Seevinck, “Geometrically undistorted MRI in the presence of field inhomogeneities using compressed sensing accelerated broadband 3d phase encoded turbo spin-echo imaging,” *Physics in Medicine & Biology*, vol. 60, no. 2, p. 615, 2015.
- C. J. G. Bakker, J. S. van Gorp, J. L. Verwoerd, A. H. Westra, J. G. Bouwman, **F. Zijlstra**, and P. R. Seevinck, “Multiple single-point imaging (mSPI) as a tool for capturing and characterizing MR signals and repetitive signal disturbances with high temporal resolution: The MRI scanner as a high-speed camera,” *Magnetic Resonance Imaging*, vol. 31, pp. 1037–1043, Sept. 2013.

## Abstracts at international conferences

- M. Maspero, C. A. van den Berg, **F. Zijlstra**, H. C. de Boer, G. J. Meijer, M. A. Viergever, J. J. Lagendijk, L. G. Kerkmeijer, and P. R. Seevinck, “Clinical evaluation of automatic localization of prostate gold fiducial markers for MR-only radiotherapy,” in *Proceedings of the 25th Annual Meeting of the ISMRM*, no. 5555, (Hawaii), 2017.
- E. Beld, M. A. Moerland, J. Schuurman, **F. Zijlstra**, M. A. Viergever, J. J. Lagendijk, and P. R. Seevinck, “Simultaneous MR imaging and control of an MR compatible afterloader: feasibility

- of real-time HDR brachytherapy source tracking,” in *Proceedings of the 25th Annual Meeting of the ISMRM*, no. 5547, (Hawaii), 2017.
- M. J. van Rijssel, **F. Zijlstra**, P. R. Seevinck, P. R. Luijten, D. W. Klomp, and J. P. Pluim, “Susceptibility-induced local  $\delta b_0$  variations are essential for predicting EPI distortions in the breast,” in *Proceedings of the 25th Annual Meeting of the ISMRM*, no. 1389, (Hawaii), 2017.
  - E. Beld, P. Seevinck, J. Schuurman, **F. Zijlstra**, M. Viergever, J. Lagendijk, and M. M.A., “Testing an mr-compatible afterloader for MR-based source tracking in MRI guided HDR brachytherapy,” in *Proceedings of the ESTRO 36*, (Vienna), pp. S141–S142, 2017.
  - **F. Zijlstra** and P. R. Seevinck, “The influence of sampling density and randomness in variable density poisson disk undersampling on parallel imaging compressed sensing,” in *Proceedings of the 24th Annual Meeting of the ISMRM*, no. 3220, (Singapore), 2016.
  - **F. Zijlstra**, J. G. Bouwman, M. A. Moerland, and P. R. Seevinck, “Fully automatic in-vivo localization of LDR brachytherapy seeds for post-implant dosimetry using MR simulations and template matching,” in *Proceedings of the 24th Annual Meeting of the ISMRM*, no. 3615, (Singapore), 2016.
  - **F. Zijlstra**, J. G. Bouwman, I. Braškute, and P. R. Seevinck, “Fast simulation of off-resonance artifacts in MRI using FORECAST (Fourier-based Off-REsonance Artifact Simulation in the STeady-state),” in *Proceedings of the 24th Annual Meeting of the ISMRM*, no. 1936, (Singapore), 2016.
  - P. R. Seevinck, **F. Zijlstra**, J. Smink, S. Krueger, F. J. van Slochteren, S. A. Chamuleau, M. A. Viergever, and M. A. Moerland, “Robust and flexible real-time MRI-guided interventions using coRASOR-mediated passive device tracking,” in *Proceedings of the 24th Annual Meeting of the ISMRM*, no. 2125, (Singapore), 2016.
  - E. Beld, M. A. Moerland, **F. Zijlstra**, J. J. Lagendijk, M. A. Viergever, and P. R. Seevinck, “Automatic high temporal and spatial resolution position verification of an HDR brachytherapy source using subpixel localization and SENSE,” in *Proceedings of the 24th Annual Meeting of the ISMRM*, no. 3585, (Singapore), 2016.
  - P. R. Seevinck, C. A. van den Berg, **F. Zijlstra**, M. E. Philippens, S. J. Hoogcarspel, J. J. Lagendijk, M. A. Viergever, and M. A. Moerland, “Pushing X-ray CT out of the equation: In vivo RASOR MRI-based seed detection for post-implant dosimetry in LDR prostate,” in *Proceedings of the 23rd Annual Meeting of the ISMRM*, no. 0864, (Toronto), 2015.
  - J. S. van Gorp, C. J. Bakker, J. G. Bouwman, J. Smink, **F. Zijlstra**, and P. R. Seevinck, “Compressed sensing accelerated broadband 3d phase encoded turbo spin-echo imaging for geometrically undistorted imaging in the presence of field inhomogeneities,” in *Proceedings of the 23rd Annual Meeting of the ISMRM*, no. 2506, (Toronto), 2015.
  - E. Beld, M. A. Moerland, J. Bouwman, **F. Zijlstra**, J. J. Lagendijk, M. A. Viergever, and P. R. Seevinck, “Localization of an HDR brachytherapy source using MR artifact simulation and phase-only cross correlation,” in *Proceedings of the 23rd Annual Meeting of the ISMRM*, no. 4151, (Toronto), 2015.
  - **F. Zijlstra**, J. Zwanenburg, M. A. Viergever, and P. R. Seevinck, “Data-driven cartesian sampling design for compressed sensing MRI,” in *Proceedings of the 22nd Annual Meeting of the ISMRM*, no. 1550, (Milan), 2014.
  - **F. Zijlstra**, B. S. van Leeuwen, and P. R. Seevinck, “High framerate positive contrast needle tracking: Compressed sensing and view-sharing accelerated co-RASOR reconstruction,” in *Proceedings of the 22nd Annual Meeting of the ISMRM*, no. 3708, (Milan), 2014.

- J. S. van Gorp, C. J. Bakker, **F. Zijlstra**, J. Smink, J. G. Bouwman, and P. R. Seevinck, “Geometrically undistorted imaging of orthopedic implants using compressed sensing accelerated phase encoded imaging,” in *Proceedings of the 22nd Annual Meeting of the ISMRM*, no. 1680, (Milan), 2014.
- B. S. van Leeuwen, S. A. van Nimwegen, **F. Zijlstra**, C. Oerlemans, J. Kirpensteijn, J. F. Nijsen, and P. R. Seevinck, “Feasibility of MR-guided needle-directed intratumoral HoMS delivery for localized radiation therapy in a large tumor-model,” in *Proceedings of the 22nd Annual Meeting of the ISMRM*, no. 1134, (Milan), 2014.
- P. R. Seevinck, C. A. van den Berg, **F. Zijlstra**, M. E. Philippens, S. J. Hoogcarspel, J. J. Lagendijk, M. A. Viergever, and M. A. Moerland, “Pushing X-ray CT out of the equation: In vivo RASOR MRI-based seed detection for post-implant dosimetry in LDR prostate brachytherapy,” in *Proceedings of the 10th interventional MRI Symposium*, (Leipzig), 2014.



# NEDERLANDSE SAMENVATTING

## Introductie

In de afgelopen twee decennia heeft Magnetic Resonance Imaging (MRI) een belangrijke plek verworven binnen de radiologie, met name door de uitstekende beeldkwaliteit en het onderscheidende vermogen van MRI in zachte weefsels. Ook biedt MRI de mogelijkheid om verschillende soorten beelden te verkrijgen, bijvoorbeeld om verschillende soorten weefsels te kunnen onderscheiden of om fysiologische eigenschappen in kaart te brengen, zoals doorbloeding van weefsel en diffusie van water in weefsel. Mede door deze gunstige eigenschappen is er een gestage toename in de vraag naar MRI onderzoeken. Om deze reden is er de laatste jaren veel aandacht voor het verhogen van de efficiëntie van MRI als beeldvormende modaliteit, met als doel om aan deze verhoogde vraag te kunnen voldoen en om de kosten van MRI onderzoeken te verminderen.

Naast het gebruik van MRI voor diagnostische doeleinden wordt MRI ook steeds vaker gebruikt voor het plannen, monitoren en sturen van behandelingen en interventies. Deze toepassingen brengen nieuwe eisen met zich mee, zoals het nauwkeurig, veilig en snel afbeelden van medische instrumenten en implantaten. Door ontwikkeling van methoden die dit mogelijk maken kunnen scans van andere modaliteiten vervangen worden door één MRI protocol, waardoor er bijvoorbeeld geen problemen meer zijn met het registreren en fuseren van scans van meerdere modaliteiten.

In dit proefschrift presenteren we vier studies waarin twee aspecten centraal staan: 1) het versnellen van het MRI proces, en 2) het lokaliseren van metalen objecten in MRI-gestuurde interventies en andere toepassingen waar de aanwezigheid van metalen objecten problematisch kan zijn. In elk van deze studies verwerken we specifieke voorkennis in de MRI acquisitie, reconstructie en beeldanalyse, volgens hetzelfde principe: hoe meer voorkennis er vooraf over een probleem beschikbaar is, des te makkelijker en sneller het probleem op te lossen is.

## Samenvatting

In **Hoofdstuk 2** hebben we de invloed van verschillende onderbemonsterings (undersampling) strategieën op reconstructiekwaliteit in Compressed Sensing (CS) onderzocht. Ten eerste hebben we de invloed van willekeurigheid en bemonsteringsdichtheid onderzocht in willekeurige undersampling patronen met variabele bemonsteringsdichtheid. Ten tweede hebben we onderzocht of op voorkennis gebaseerde undersampling patronen de reconstructiekwaliteit kunnen verbeteren wanneer één of meer MRI scans als voorkennis beschikbaar zijn. Hiervoor hebben we drie verschillende methoden geïmplementeerd om deze voor-

kennis te gebruiken: (1) Monte Carlo optimalisatie van de bemonsteringsdichtheid, (2) bemonsteringswaarschijnlijkheden bepalen uit de signaalsterkte in het frequentiedomein, en (3) iteratief ontwerp van undersampling patronen op basis van minimalisatie van reconstructiefouten. Met behulp van kruisvalidatie en retrospectieve reconstructies hebben we deze methoden geëvalueerd en onderzocht wat de invloed was van de hoeveelheid scans die als voorkennis beschikbaar waren. Tenslotte hebben we twee van deze methoden prospectief toegepast om de praktische toepasbaarheid van deze methoden aan te tonen.

Onze resultaten laten zien dat de optimale bemonsteringsdichtheid afhankelijk is van de soort anatomie die gescand wordt. Hieruit volgt dat het kiezen van een bemonsteringsdichtheid zonder enige voorkennis waarschijnlijk suboptimaal is. Van de op voorkennis gebaseerde methoden leverde de iteratieve ontwerpmethodede significant hogere reconstructiekwaliteit in de retrospectieve en prospectieve experimenten. De twee andere methoden leverden reconstructiekwaliteit die vergelijkbaar was met undersampling op basis van de optimale bemonsteringsdichtheid. Het aantal scans dat gebruikt was als voorkennis had maar een kleine invloed op de reconstructiekwaliteit. Deze resultaten laten zien dat met tenminste één volledige geacquireerde scan als voorkennis suboptimale reconstructiekwaliteit voorkomen kan worden middels op voorkennis gebaseerde undersampling methoden.

In **Hoofdstuk 3** beschrijven we een snelle methode om artefacten ten gevolge van susceptibiliteitsverschillen in MRI te voorspellen. Door gebruik te maken van de herhaling in de pulse sequentie hebben we aangetoond dat fase encoding versneld kan worden middels fast Fourier transformaties. Op deze manier wordt de computationele complexiteit van deze simulaties lager dan die van Bloch simulaties. Snelle simulaties van artefacten rondom metalen objecten zijn gevalideerd door de uitkomst te vergelijken met Bloch simulaties en MRI scans. De verschillen in de gesimuleerde beelden was klein, terwijl de computationele complexiteit van onze methode lager was met een factor gelijk aan het aantal herhalingen van de pulse sequentie. Dit resulteerde in een versnelling van de simulatie met een factor 400 voor een 2D simulatie met matrixgrootte  $256 \times 256$ . Voor 3D simulaties verwachten we dat de methode meerdere orde van grootte sneller is dan Bloch simulaties, wat ons in staat stelt om 3D simulaties van susceptibiliteitsartefacten met hoge resolutie uit te voeren.

We hebben de praktische toepasbaarheid van deze snelle simulaties aangetoond door de methode te gebruiken om metalen objecten in MRI scans te lokaliseren. Met susceptibiliteitsmodellen als voorkennis zijn we met de snelle simulaties in staat om de artefacten rondom het object te simuleren voor een groot aantal oriëntaties van het object. Elk van deze simulaties kan met behulp van fase correlatie in een MRI scan herkend worden, waardoor de locatie en oriëntatie van het object gevonden kan worden. We hebben deze lokalisatiemethode toegepast op MRI scans van een titanium cilinder, een geoxideerd zirkonium knie implantaat, en kleine gouden markers. Elk van deze objecten werd nauwkeurig gelokaliseerd.

In **Hoofdstuk 4** hebben we de metaal lokalisatie methodologie uit Hoofdstuk 3 uitgebreid en toegepast op het lokaliseren van brachytherapiezaadjes in de prostaat. Lokalisatie van brachytherapiezaadjes met alleen MRI scans zou het uitvoeren van dosimetrie na implantatie met alleen MRI ondersteunen, wat het overbodig maakt om hiervoor CT scans en beeldregistratie te verrichten. Echter, in brachytherapie worden een groot aantal van deze zaadjes in een relatief klein gebied ingebracht, waardoor het lokaliseren ervan met alleen MRI uitdagend is. Om ook onder deze omstandigheden de zaadjes individueel te kunnen lokaliseren hebben we een lokale herkenningstechniek op basis van lineaire regressie geïmplementeerd. Hiermee kunnen we detecties die gevonden worden met de methode uit

### **Hoofdstuk 3** controleren en bepalen of het inderdaad geldige detecties waren.

We hebben deze methode toegepast op MRI scans van 25 prostaatkankerpatiënten die met brachytherapie behandeld zijn en voor wie dosimetrie vier weken na behandeling uitgevoerd is. Onze methode heeft 1490 van de 1557 zaadjes correct gedetecteerd met 67 vals positieve detecties. De locaties van de correct gedetecteerde zaadjes waren zeer nauwkeurig met een fout van gemiddeld 0.8 mm in vergelijking met lokalisatie op CT scans. Door de foute detecties te classificeren hebben we gevonden dat de meeste vals positieve detecties optreden nabij andere zaadjes. De meeste vals negatieve detecties treden op in strengen van zaadjes zonder afstandsstukken of nabij andere zaadjes. Deze resultaten tonen aan dat brachytherapiezaadjes met een hoge nauwkeurigheid gelokaliseerd kunnen worden met alleen MRI met behulp van patroonherkenning van complexe artefacten rondom de zaadjes. Voor het na behandeling uitvoeren van dosimetrie is de belangrijkste overgebleven uitdaging om de methode robuust te maken in gevallen waar meerdere zaadjes dicht bij elkaar geplaatst zijn.

In **Hoofdstuk 5** combineren we de methode voor lokalisatie van metalen objecten uit **Hoofdstuk 3** met radiële undersampling en het witte marker fenomeen, om met hoge snelheid interventionele hulpmiddelen te lokaliseren in MRI. Door gebruik te maken van een pulse sequentie waarin meerdere echo's opgenomen worden kunnen we tegelijkertijd anatomische beelden verkrijgen waarin de versturende effecten van het metaal minimaal zijn en waarop de metalen objecten te visualiseren zijn. We hebben deze aanpak getest in een agarose fantoom waarin vijf stalen markers worden gelokaliseerd en in een meer realistische situatie waarin een titanium naald wordt gelokaliseerd tijdens het inbrengen van de naald in een stuk weefsel van een varken.

We hebben lokalisatie experimenten uitgevoerd met stationaire en bewegende objecten. De locaties van de stationaire stalen markers hebben we vergeleken met een lokalisatie van deze markers met behulp van CT. De gemiddelde afstand tussen de locaties op MRI en CT was 0.30 mm, wat dichtbij de theoretische limiet ligt van een systeem dat op de MRI resolutie van 1.2 mm lokaliseert. Om de nauwkeurigheid van de lokalisatie tijdens beweging te evalueren hebben we aangenomen dat de configuratie van de markers rigide was. De afwijking van deze configuratie was gemiddeld 0.29 mm en bleef relatief constant tijdens beweging.

Kwalitatieve evaluatie van het inbrengen van de naald laat zien dat de lokalisatie van de naaldpunt stabiel was gedurende het inbrengen en terugtrekken van de naald. De anatomische informatie rondom de naaldpunt was vrijwel onverstoorde door de lage echotijd en snelle acquisitie van het anatomische beeld. Tenslotte hebben we laten zien dat het lokalisatie algoritme toegepast kan worden in acquisities van twee beeldvlakken tegelijkertijd. Dit kan automatisch positionering van de beeldvlakken ondersteunen, zodat de scan gecentreerd blijft op het object.

Deze lokalisatie methode op basis het passief volgen van objecten heeft voordelen die traditioneel alleen beschikbaar waren met het actief volgen van objecten: nauwkeurig lokaliseren van objecten met hoge snelheid, de mogelijkheid om tegelijkertijd anatomische informatie af te beelden, en de mogelijkheid om automatisch beeldvlakken te positioneren. Een belangrijk voordeel van de methode is het feit dat er geen specifieke hardware nodig is, met als gevolg dat elk rigide metalen object gelokaliseerd kan worden, zolang het veilig in MRI te gebruiken is en voorspelbare artefacten veroorzaakt.

## Discussie en Conclusie

In dit proefschrift hebben we aangetoond dat verschillende soorten voorkennis gebruikt kunnen worden om MRI te verbeteren, bijvoorbeeld door scantijd te verminderen, metalen objecten te lokaliseren die anders lastig te herkennen zijn, en door MRI-gestuurde interventionele procedures te ondersteunen. Hierbij is het belangrijk om op te merken dat ook in deze studies nog niet het volledige potentieel van de voorkennis gebruikt is. Om in de toekomst meer voorkennis toe te passen in MRI acquisitie, reconstructie, en beeldanalyse is het belangrijk dat alles wat relevante voorkennis kan opleveren verzameld en opgeslagen wordt. Op een dergelijke manier op grote schaal data verzamelen zal nieuwe vraagstukken oproepen over veilige opslag en het gebruik van deze data voor wetenschappelijke doeleinden.

Hoe voorkennis in het beeldvormende proces opgenomen moet worden hangt sterk af van de applicatie. De op data gebaseerde methode uit **Hoofdstuk 2** is fundamenteel anders dan de op fysica en modellen gebaseerde aanpak uit **Hoofdstukken 3 tot 5**. Het zal dus lastig zijn om onze methoden te generaliseren naar fundamenteel andere problemen met andere soorten voorkennis. Onze studies laten echter wel zien dat het gebruik van voorkennis meerwaarde creëert, en hoe dit op een systematische, wiskundige manier kan worden aangepakt om specifieke problemen op te lossen. In het bijzonder in **Hoofdstuk 5** laten we zien dat er waarde is in een aanpak waar acquisitie, reconstructie, en beeldanalyse niet als op zichzelf staande eenheden beschouwd worden. In het algemeen denken we dat een dergelijke holistische aanpak een grote rol kan spelen in het versnellen, verbeteren en efficiënter maken van MRI en het oplossen van specifieke klinische vraagstukken.

Met de studies in dit proefschrift hebben we aangetoond dat voorkennis gebruikt kan worden om MRI acquisitie, reconstructie, en beeldanalyse te optimaliseren en om klinisch relevante informatie over de locatie van metalen objecten in MRI te verkrijgen. Een vermindering van scantijd kan verwacht worden in een geoptimaliseerde implementatie van Compressed Sensing (**Hoofdstuk 2**). Nauwkeurige lokalisatie van metalen objecten kan de efficiëntie van werkwijzen op basis van alleen MRI verhogen (**Hoofdstukken 4 en 5**), waardoor scans van andere beeldvormende modaliteiten zoals CT niet meer nodig zullen zijn. Hierdoor zal beeldregistratie niet meer nodig zijn, wat de werkwijzen minder arbeidsintensief maken. Deze vooruitgangen vertalen zich rechtstreeks in een vermindering van kosten van MRI en een efficiëntere behandeling van de patiënt.

## ABOUT THE AUTHOR

Frank Zijlstra was born on the 31st of August 1985 in Drachten and grew up in Zeijen. In 2003, he finished his secondary education at the Dr. Nassau College Quintus in Assen. In 2007, he received his Bachelor of Science degree in Technical Computer Science at the University of Twente. In 2012, he received his Master of Science degree in Biomedical Image Sciences at Utrecht University. His Master's thesis on localizing microscopic infarctions in the brain was completed at the Image Sciences Institute at the University Medical Center Utrecht. After obtaining his MSc he continued as a PhD candidate at the Image Sciences Institute, researching acceleration of MRI and localization of metal objects for MRI-guided interventions. The results of that research are presented in this thesis.

